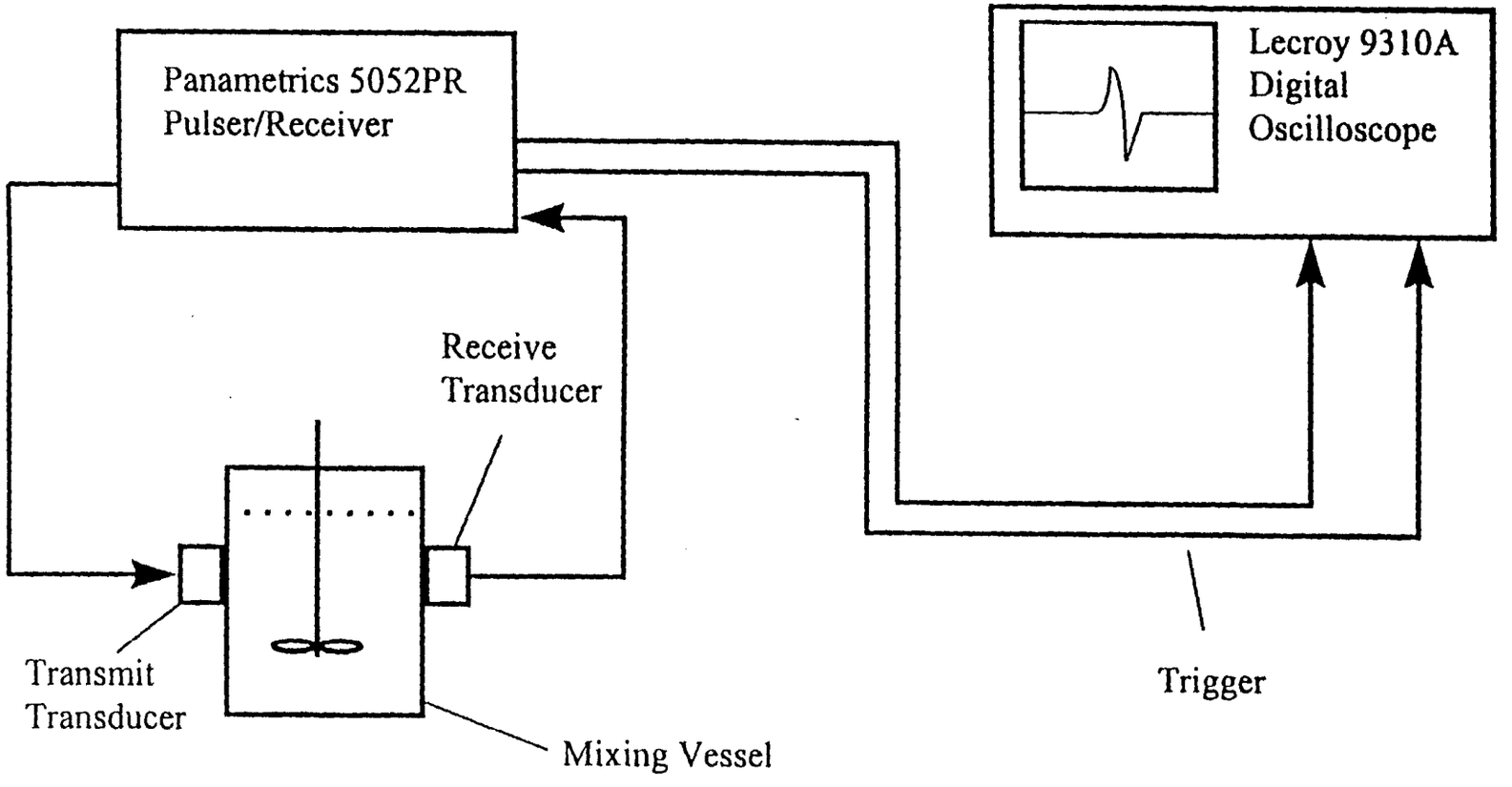

Figure 3.4: Schematic diagram of the experimental set-up used in the Pulse/FFT Technique.

capable of either 20 or 40 dB of gain and an attenuator capable of 0 to 58 dB of attenuation. The received pulse is then sent to the oscilloscope where the signal is averaged, and a Fast Fourier Transform (FFT) is performed on the averaged waveform. The average is usually calculated over 50 to 100 sweeps of the time domain duration of the signal of interest. The number of sweeps used in the averaging is dependent upon how quickly conditions in the sample are changing. If the particles or bubbles are large and tend to separate from the mixture quickly, fewer sweeps are used in the averaging of the waveform received. Through trial and error it has been determined that 50 sweeps allows for smoothing (averaging) of the received signal before the phases of a given slurry can separate. An example of a received pulse and its FFT magnitude spectrum (used by Panametrics a calibration for a 1.0 MHz transducer) is shown in Figure 3.5. The magnitude spectrum generated by the FFT is then saved on a floppy disk as an ASCII data file and loaded into a MATLAB™ code where the attenuation is calculated in a manner identical to that described previously in this section.

The advantage to the Pulse/FFT technique over that of the Toneburst technique is that the entire operating frequency range of a given pair of transducers can be covered in a single measurement rather than requiring measurements at incremental frequencies over the transducer operating range, as is the case of the toneburst measurements. A pulse is comprised of the sum of many sinusoidal waves of various frequencies (Ramirez 1985), and thus, the FFT of a received pulse of a given amplitude will exhibit magnitude values over the entire operational frequency range of a given pair of transducers. The Pulse/FFT

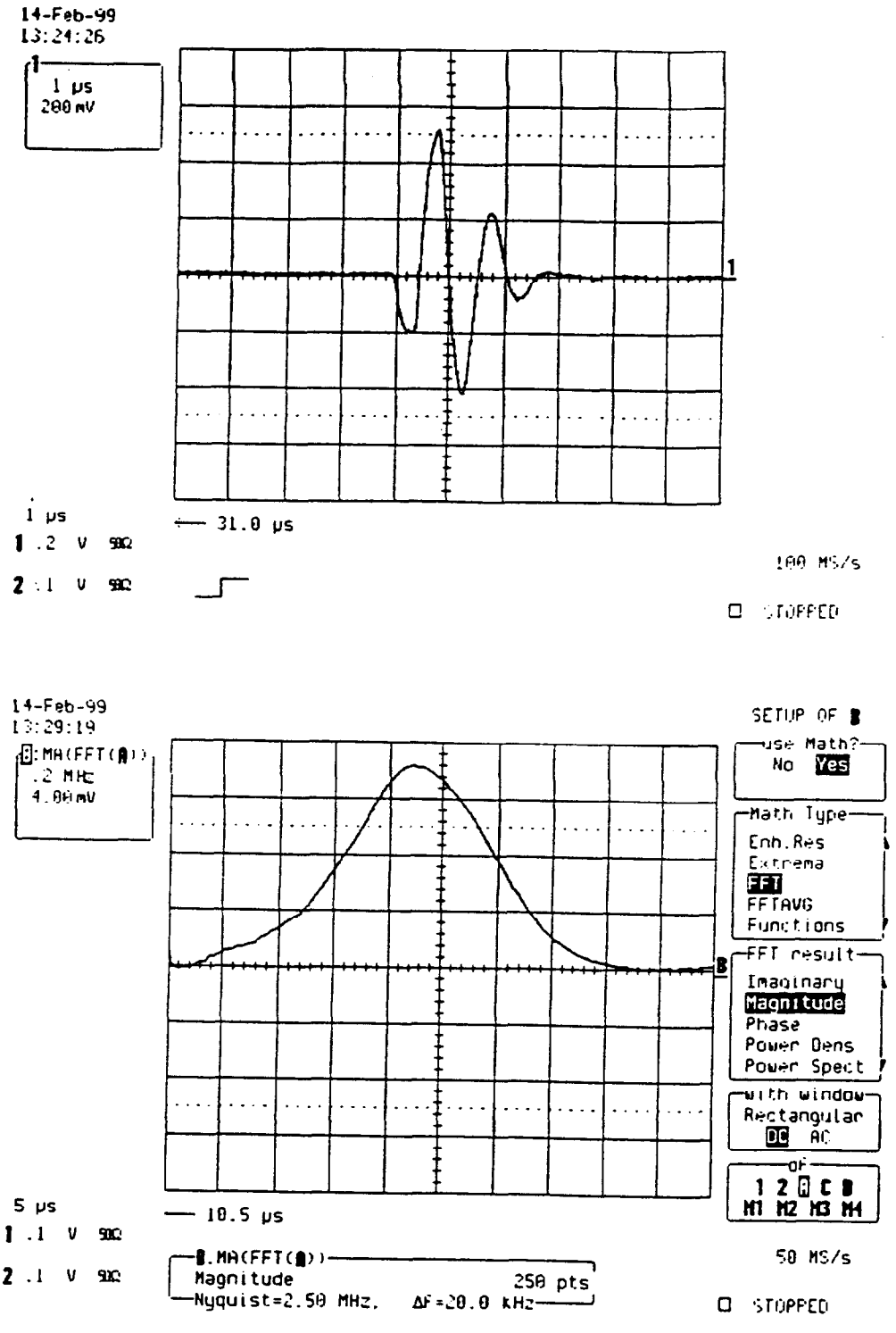

Figure 3.5: Oscilloscope trace and FFT Spectrum of received signal through water for a 1.0 MHz transducer with negative spike pulse input signal.

technique greatly increases the speed and efficiency of attenuation data acquisition. A comparison between results of the two data acquisition techniques is made in Section 3.5

3.1.3 Photomicrogrphic Video Imaging System:

In the present study bubble sizes in solid-gas-liquid slurries are estimated through the use of a digital photomicrographic video imaging system. This imaging system consists of a Company 7 "Questar" QM-100 long distance microscope (identical to that used by Burns *et al.* (1996) and Shin *et al.* (1997)) providing magnification of approximately 152 times at a working distance of 17.8 cm (7"). The microscope is coupled to a Cohu Model 4810 2/3" format monochrome CCD video camera. The CCD video camera is synchronized to a strobe light via a Global Specialty Corporation 4001 Pulse Generator and interfaced in parallel with an Apple Power Macintosh G3 desktop computer equipped with a Scion VG-5 PCI frame-grabber board and an Apple ColorSync 20 "high resolution" monitor. The strobe light provides backlighting so that the bubbles appear as dark images on a light background, and the strobe is synchronized with the camera so that the moving bubbles appear as though "frozen" in space. The imaging system setup is shown schematically in Figure 3.6.

Images obtained by the CCD video camera are sent to the computer where image analysis is performed. Initially, the image analysis was performed using the Scion *Image* software package provided with the frame-grabber board. However, that software package has been replaced by a more advanced, privately distributed, software package called *Image SXM*, version 1.61-7 (Barrett 1998).

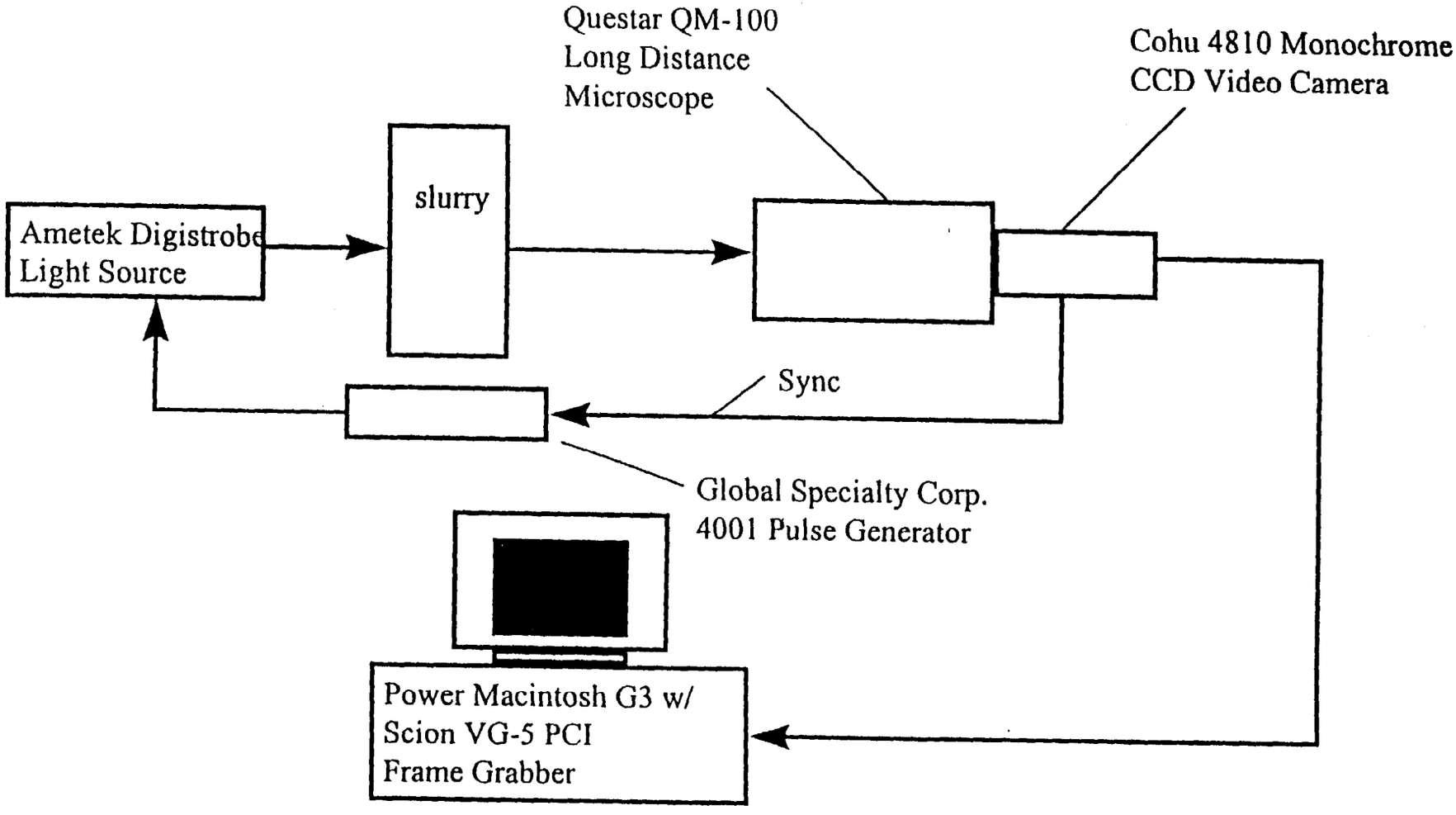

Figure 3.6: Schematic diagram of the experimental set-up for the photomicrographic video imaging system.

The most difficult consideration involved with the imaging system is that of the proper lighting to be used. As was discussed by Bongiovanni *et al.* (1997), the error in photographing spherical particles can be considerable depending upon the relative positions of the backlighting, the object, and the objective lens. However, bright field backlighting is the most desirable lighting technique (as opposed to, say, dark field lighting) in the consideration of possible three phase particle and bubble size measurements. In dark field illumination, it is difficult to distinguish between solid particles and bubbles. Also, an illumination configuration such as that employed by Kirou *et al.* (1988) is not feasible as the test cell size is too small to accommodate the fiber optic apparatus; and, according to Bongiovanni *et al.* (1997), the relative size and close proximity of the light source to the focal distance of the particles or bubbles will introduce large errors in the size measurements. Therefore, since the experimental measurements and the optical apparati involved are similar, bubble measurements are made by the method employed by Burns *et al.* (1997) and Shin *et al.* (1997), and a calibration is performed using particles of known sizes to determine how much, if any, error is present in the size measurements by this method. Back lighting is provided by a strobotach placed about 61 cm (24") behind the test cell. The microscope is placed at a working distance of approximately 17.8 cm (7") from the center of the test cell. As the strobotach has a lighting element that is only 4" in diameter, the error in the size measurements should be relatively small. The 17.8 cm working distance is chosen because it is a working distance which provides for reasonable magnification of the

smallest calibration particles while still allowing the largest particles to be photographed at the same working distance.

The calibration is begun by setting the scaling factor for the conversion from pixel count to size measurement. This task is performed by photographing a reticle marked with circles of various sizes. Diameter measurement is performed on the smallest circle on the reticle, which is 0.005" (127 ± 2 μm) in diameter. This information is then used to make the pixel to length conversion. This calibration is performed before each series of measurements or whenever the focus of the microscope is adjusted. Further calibration is performed to determine the overall measurement error by photographing NIST traceable polystyrene spheres (Duke Scientific Corp., Palo Alto, CA) of certified diameter at lighting conditions identical to those to be used in actual bubble measurements. Four different sphere diameters are used in the calibration. The sizes (diameters) are, respectively, 25.02 ± 0.12μm, 50.4 ± 1.0μm , 103 ± 1.8μm, and 158 ± 3.2 μm. A series of photographs is obtained for each particle diameter and an average of 50 diameter measurements are made from these photographs at each particle size. The diameter measurements for each particle size are averaged, and the average particle diameter is plotted versus the known (certified) particle diameter. A best fit least squares line is then fitted to these data using the "polyfit" routine in MATLAB™. The least squares fit yields the following relationship between the measured and true particle diameters:

$$d_{meas} = 1.25 d_{true} - 10.4, \qquad (3.2)$$

where d_{meas} and d_{true} are the measured and true (known) particle diameters, respectively. The calibration curve is shown in Figure B.3 in Appendix B.

3.2 Experimental Procedure—Solid-Liquid Slurries:

3.2.1 Dilute Soda-Lime Glass Slurries:

The initial solid-liquid attenuation experiments are performed in slurries of soda-lime glass beads in distilled water at various solids volume fraction. The soda-lime glass beads have been purchased from Cataphote, Inc. and have a density of 2.54 g/cm^3. The physical properties of these particles are shown in Table 3.2. Particle size distribution measurements have been performed on these beads at the Battelle Pacific Northwest National Laboratory (PNNL), and it has been determined that the batch of beads used in these experiments has a particle mean diameter of 32 μm and standard deviation of 7.6 μm (Greenwood, private communication 1998). Solids volume fractions of the various slurries is confirmed by making mass measurements of known volumes of suspended slurry upon completion of experimental runs. The solids volume fraction is determined from the following equation:

$$\phi_s = \frac{\rho_{slurry} - \rho_{H_2O}}{\rho_{solid} - \rho_{H_2O}} \quad , \tag{3.3}$$

where ϕ_s is the solids volume fraction in the slurry, and ρ_{slurry}, ρ_{solid}, and ρ_{H2O} are, respectively, the slurry, solid, and water densities.

Two pairs of transducers are put in place for each experimental series performed in the 1.6 L PVC mixing vessel. Before performing each experiment, the separation distance between each pair of transducers is measured and recorded, and the vessel is then filled with distilled water. The voltage amplitude of monochromatic tonebursts over incremental frequencies is measured over the operational range of each pair of tranducers

	Polystyrene	Soda-lime Glass	Water	Glycerin/ Water Mixture
Density (g/cm^3)	1.055	2.54	1.0	1.08
Thermal Conductivity ($J/K \cdot cm \cdot s$)	1.15×10^{-3}	9.6×10^{-3}	5.87×10^{-3}	4.5×10^{-3}
Specific Heat ($J/g \cdot K$)	1.19	0.836	4.19	4.19
Thermal Expansion Coefficient ($1/K$)	2.04×10^{-4}	3.2×10^{-6}	2.04×10^{-4}	3.22×10^{-4}
Attenuation Coefficient per f^2 (s^2/cm)	1.0×10^{-15}	1.0×10^{-15}	2.5×10^{-16}	–
Sound Speed (cm/s)	2.3×10^{5}	5.2×10^{5}	1.48×10^{5}	1.6×10^{5}
Shear Viscosity ($g/cm \cdot s^2$)	–	–	1.01×10^{-2}	3.2×10^{-2}
Shear Rigidity ($g/cm \cdot s^2$)	1.27×10^{10}	2.8×10^{11}	–	–

Table 3.2: Values of physical properties used in theoretical calculations. The values for polystyrene are from Epstein and Carhart (1953). The properties of soda-lime glass are from Kinsler *et al.* (1982) and Bolz (1973). The properties of glycerin are from *Perry's Chemical Engineer's Handbook* (1984) and the *CRC Handbook of Chemistry and Physics* (1984).

in the toneburst technique, or an FFT is performed on the received waveform of a negative spike pulse input signal for each pair of transducers in the Pulse/FFT technique. In each case it is important to record the pertinent operating parameters of each particular pulse generating apparatus. In the case of the toneburst technique, where the Matec TB-1000 digital synthesizer is used, the recorded parameters consist of the frequency, the amplifier gain, and attenuator box settings (if necessary). In the case of the Pulse/FFT technique the recorded parameters are the pulse repetition rate, the pulse energy, the receiver attenuation, the high pass filter setting, the damping, and the receiver gain. The digital oscilloscope is set to parameters which are appropriate for the given experimental run, and these parameters are either recorded manually or shown in printed "hardcopies" of oscilloscope waveform traces.

After voltages are measured by either technique for the distilled water, the water is drained from the vessel and replaced with the slurry to be interrogated. The slurry is suspended via agitation by a Lightnin' Labmaster II™ Model TS 2510 portable mixer fitted with a 5.08 cm diameter marine propeller type impeller. It is important to make certain that the impeller and shaft are positioned off center in the mixing vessel so that they are not in the travel path of the acoustic signal. The agitation speed is varied as the agitation speed employed in each case is the highest speed achievable such that the solids are suspended, but there is no vortex "tube" which extends into the acoustic travel path. These conditions are usually satisfied by agitation speeds ranging from 300 to 600 rpm. Voltage measurements are then made for the slurries in the same fashion as those made for the distilled water.

The voltage data for both the distilled water and the slurries are then entered into ASCII data files which are loaded into MATLAB™ codes to calculate the attenuation by using equation (3.1) after correcting for the receiver gain and receiver attenuation.

3.2.2 Dilute Polystyrene Slurries:

Attenuation measurements are also made in dilute suspensions of polystyrene beads in water. The polystyrene beads are manufactured by Duke Scientific Corp., Palo Alto, CA and are composed of polystyrene with 2 % divinylbenzene (considered pure polystyrene in this study). The physical properties of these particles are also given in Table 3.2. They are purchased as nominally "monodispersed" 158 μm diameter polystyrene spheres, but the calibration information provided by the manufacturer shows that spheres actually have a rather narrow size distribution with mean diameter of 158 ± 5 μm and standard deviation of 3.6 μm. Due to the very narrow size distribution, the spheres are somewhat expensive, and only a small quantity has been purchased which come from the manufacturer in a 10 % (by wt.) suspension in water. Since the particles have a density of 1.05 g/cm^3, weight percent is approximately equal to volume percent. The purchased quantity is diluted to a 5 % (by volume) suspension, and there is sufficient volume of slurry to perform attenuation measurements in the 5.08 cm test cell.

Attenuation measurements are performed in this slurry using both the toneburst and Pulse/FFT techniques described previously in Section 3.1.2.

3.2.3 Concentrated Soda-Lime Glass Slurries:

Attenuation measurements are also performed in relatively concentrated slurries of soda-lime glass beads. These beads are soda-lime glass beads manufactured by Potter's Industries, Inc. (Brownwood, TX) with a specified density of 2.54 g/cm^3. The physical properties of these particles are shown in Table 3.2. These particles have also been subjected to particle size measurements at the Battelle Pacific Northwest National Laboratory, and it has been determined that the particles have a mean diameter of 125 μm with standard deviation of 19 μm.

Because these particles are rather large, even concentrated slurries are difficult to suspend in a pure water continuous phase. Therefore, the suspending liquid which is employed is a mixture of approximately 29 % (by wt.) of glycerin (approximately 99 % reagent grade, Sigma Chemical Company) in distilled water. The addition of the glycerin increases the liquid phase density to approximately 1.08 g/cm^3, and the liquid phase viscosity by approximately a factor of three. The liquid phase viscosities of these solutions range from 0.0259 g/cm·s to 0.0308 g/cm·s. Thus, the solid particles settle much more slowly, and attenuation measurements can be made. It should be noted that even with the addition of glycerin, the particles still settle sufficiently quickly that the suspension of large volumes of slurry is difficult. Therefore, only small volumes of the concentrated slurries are prepared, and all measurements are performed in the various "box" geometry test cells.

Slurries are prepared at 5 %, 10 %, 15 %, 20 %, 30 %, 40 %, 45 %, and 50 % solids by volume. These slurries are then subjected to attenuation measurements in the

various test cells by both the toneburst and Pulse/FFT techniques described previously. It should also be noted here that the "pure liquid" reference voltages in these experiments are not made in pure distilled water, but rather in the individual glycerin/water mixtures in which the solids of each slurry are suspended. Each time a slurry is prepared, a portion of the suspending liquid mixture is put aside and saved to be used as the "reference liquid" for the attenuation measurements in that slurry. The average physical properties for the glycerin/water mixtures are given in Table 3.2.

3.3 Experimental Procedure—Bubble Generation:

Several different methods have been employed to generate bubbles for attenuation measurements in bubbly liquids and solid-gas-liquid systems. Each method has its particular advantages and disadvantages with respect to reproducible bubble generation rate, bubble size distribution, compatibility with the ultrasound measurement equipment and slurry solids, etc.

The first bubble generation method which has been employed is an electrolysis method based on that used by Kol'tsova *et al.* (1979). Electrolysis has the advantage of producing relatively small bubbles (< 100 μm diameter), but it can be difficult to control when operated in a continuous mode as the electrolysis causes the electrical properties of the water to change with time. These changes cause variations with time in the current provided to the electrolyzer which makes reproducible bubble production difficult. Also, continuous operation of the electrolyzer over an extended period of time causes significant increases in the temperature of the medium under interrogation. As the

density of most media changes with temperature, and the attenuation of acoustic energy in materials is strongly dependent upon the material density, these temperature changes are most undesirable. The possibility of using the electrolytic bubble generation method in a non-continuous fashion has also been explored and will be discussed in more detail later in this section. Another significant disadvantage to using the electrolytic generation technique is that the ultrasonic transducers are grounded. Because of this grounding, the safety controls in the DC power supply (Sigma-Aldrich Model PS 4010-1) cause it to shut off due to a "ground leak error" fault whenever the transducers are in direct contact with the sample under investigation.

The second bubble generation technique investigated is an electrostatic spraying technique based on that used by Tsouris *et al.* (1995). This technique produces bubbles which are approximately the same size as those produced by electrolysis, however, this technique has also proven to be difficult to employ reproducibly. Electrostatic spraying of air into water requires the use of de-ionized water. As the process is operated, ions begin to accumulate in the water, and the technique becomes less effective with time. This situation is further exacerbated by the addition of solids, such as soda-lime glass beads, which have a fairly high content of ions which will migrate from the solids into the liquid phase. The aforementioned factors, coupled with the solids also tending to clog the capillary spray nozzle make the electrostatic spraying technique difficult to control, and therefore, undesirable as a bubble generation technique.

The third bubble generation technique which has been explored is the use of air pumped through an aquarium aerator stone. The particular aerator used is manufactured

by Coralife (Energy Savers Unlimited, Inc., Harbor City, CA) and is made from limewood. Limewood has the unique property that it contains a number of small straight pores which allow for the production of relatively small bubbles. The aerator is operated by interfacing it with a Cole-Parmer Model 74900 syringe pump and pumping air at various metered flow rates. This method of bubble generation is quite successful in that bubbles are generated fairly consistently over long periods of time even with solids present. This technique is the one employed in the initial "proof of principle" solid-gas-liquid attenuation measurement experiments. A notable characteristic of this method is that the bubbles produced are of fairly large diameter and wide size distribution relative to those produced by the other methods, such as electrolysis. The bubbles produced from the limewood aerator, when operated in water at an air flow rate of 150 ml/hr, are photographed and measured using the photomicrographic imaging system described in Section 3.1.3, and the bubble population is determined to have a mean diameter of 141 μm with standard deviation of 67 μm. The bubble volume fraction is estimated to be approximately 0.02. These bubble size characteristics are somewhat undesirable as bubbles of these sizes have rather low resonance frequencies; it is, therefore, difficult to examine the effects of bubble resonance with bubbles of these sizes.

As was previously mentioned, the possibility of producing bubbles by electrolysis in a non-continuous manner has been explored. It has been determined, by trial and error, that if bubbles are generated electrolytically only for a time period which is long enough to establish bubble flow, mix the vessel contents, and make an acoustic measurement, fairly reproducible electrolyzer performance can be maintained. The other drawback to

the electrolytic technique is the recurrence of "ground leak error" faults when the transducers are in place which would cause the DC power supply to shut off. This problem is rectified by covering the wear plates of the transducers with Parafilm™, a paraffin laboratory covering wrap, and coupling the Parafilm™ to the transducers with ultrasound gel. Also, the transducers have to be disconnected from the pulse generator until bubble flow is established. Incorporation of these improvements allows for the use of electrolysis as a method of bubble generation in the attenuation experiments.

The electrolytic set up in the test cells is rather simple. The cathode (negatively charged electrode) consists of an approximately 30 cm length of 1.3 mm diameter copper electrical wire with the insulation stripped away from approximately ¼" of the wire end and the individual wire strands separated, run vertically through an 1/8" NPT to Swagelok fitting in the bottom of the cell so that it sticks upright perpendicular to the flat bottom of the cell. Care is taken to avoid the cathode wire protruding into the acoustic path between transducers. The anode (positively charged electrode) is an approximately 4 cm length of 1/8 " diameter stainless steel rod positioned against the test cell wall with approximately one centimeter of its length immersed below the liquid surface. When the DC power supply is turned on, bubbles are generated at the cathode and rise upward toward the anode. Bubbles are generated in all experiments at 40 V; 4 to 8 mA; and <1 W. The bubbles generated in water at these conditions are photographed and measured using the photomicrographic imaging system described in Section 3.1.3. These bubbles are found to have a mean diameter of 51 μm with standard deviation of 26 μm. The bubble volume fraction is estimated to be approximately 0.002.

3.4 Experimental Procedure—Solid-Gas-Liquid Slurries:

The attenuation measurement experiments in solid-gas-liquid slurries are very similar in nature and procedure to those performed in solid-liquid slurries. In fact, the experimental procedure for the solid-gas-liquid systems actually includes a step where the attenuation is measured in a solid-liquid slurry without the presence of gas bubbles. Solid-liquid slurries are prepared at 5 % and 10 % solids (by volume) using the same soda-lime glass beads which are described in Section 3.2.1. Attenuation measurements are performed in these slurries using the Pulse/FFT technique described previously in Section 3.1.2. Once attenuation measurements are made in the solid-liquid slurry of interest in the particular experiment, bubbles are generated using either electrolysis to generate relatively small, narrowly distributed bubbles (approximately 25 to 76 μm in diameter) or air pumped at 150 ml/hr through the limewood aerator stone to generate larger, more widely distributed bubbles (approximately 74 to 210 μm in diameter). In the case where the bubbles are generated electrolytically, the DC power supply is operated at 40 V; 4 to 8 mA; and < 1 W. When the LCD display on the power supply shows that it is operating at the specified conditions, the (now solid-gas-liquid) slurry is mixed thoroughly with a glass or plastic stirring rod and a measurement is made. The data are recorded as per the procedure described in Section 3.1.2, and "hardcopies" of the oscilloscope traces and FFT spectra are entered into the laboratory notebooks. All computer files are stored both on the hard drive of the data acquisition computer (Gateway 2000 P5-66) and on 3.5" floppy diskette. Also in these experiments, bubbles are generated by both methods in the water used to make the reference measurements

after the reference measurements are made. Pulse/FFT measurements are made in these bubbly liquids, and the data are recorded in order to calculate bubbly liquid attenuations for later comparison with solid-gas-liquid attenuations in an attempt to obtain information about any effects the solids may have on the bubble size.

3.5 Quality of Experimental Results:

3.5.1 Comparison of Attenuation Measurement Techniques:

Upon development of the Pulse/FFT technique for obtaining attenuation data in the various slurries, one of the most important issues to be addressed is how well the attenuation data obtained by this technique compare with those obtained by the Toneburst measurement technique. A comparison of attenuation data obtained by both techniques in a 5 % (by vol.) slurry of soda-lime glass beads in water is shown in Figure 3.7. From this figure is clear that the two methods of obtaining data are equivalent under most conditions. It is found, however, that in dilute slurries the Pulse/FFT technique yields better results at lower frequencies than the toneburst technique. The results are better for the Pulse/FFT technique because the toneburst measurements are made by manually moving the horizontal oscilloscope cursors to correspond with the wave peaks and troughs in the received toneburst signal. At lower frequencies, the attenuation is small, and the error in the measurements becomes large relative to the magnitude of the measurements, themselves (on the order of 20 % relative error). In the case of the Pulse/FFT technique, the amplitude as a function of frequency is calculated from the received pulse waveform by the oscilloscope as part of the FFT algorithm. Since

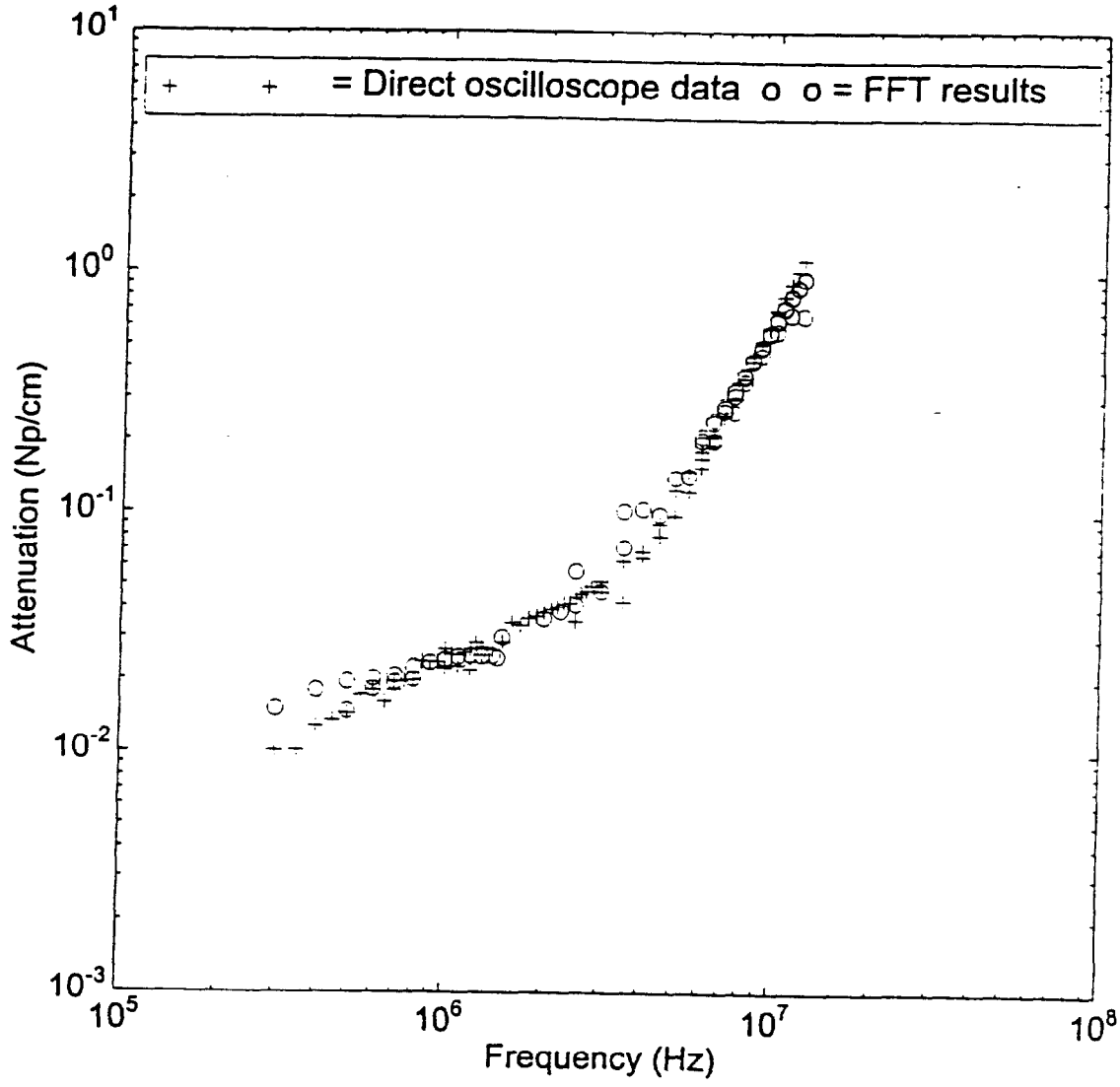

Figure 3.7: Comparison of attenuation spectra results obtained in a 5 % soda-lime glass slurry by both the Toneburst and the Pulse/FFT Techniques. - E1301.

Pulse/FFT method is an automated measurement technique, the measurement error at lower frequencies is smaller than that observed in the manually performed toneburst measurements.

3.5.2 Reproducibility of Experimental Results:

In order to examine the reproducibility of experimental results, complete repeat experiments have been performed at various times throughout the course of this study. These duplicate experiments are performed in addition to collecting data by more than one technique (as discussed in the previous section) in order to establish an overall sense of the reproducibility of the experimental results. As the acoustic attenuation behavior of these various slurries is quite complicated, and the data for these specific systems (e.g. particle type and size, and gas phase concentration) are unique, it is difficult to perform a rigorous error analysis to determine the absolute accuracy of the results. It is, however, possible to investigate the quality of the data with regard to the reproducibility of results and their agreement with theoretical predictions.

Experiments are repeated (total of three experiments) in the attenuation measurements made in the soda-lime glass slurries at 5 % solids by volume using the Toneburst technique. Also, repeated experiments are performed in the concentrated slurry experiments with the Potter's beads slurries in glycerin/water. Duplicate experiments are performed at 50 % (two duplicates), 30 %, and 10 % solids by volume.

Figure 3.8 shows the average (solid line) attenuation versus frequency curve, with error bars, for three experiments using slurries of 5 % (by volume) soda-lime glass beads

in water. The error in the measurements is taken to be the mean difference between the experimentally determined attenuation value and the mean attenuation value at each frequency. It can be seen from Figure 3.8 that the data, except at the lowest frequencies where the attenuations are rather small, fall within 5 % (relative error) of the average value. Even at the lowest frequencies, the measurement error still permits results which are within 20 % of the mean value of the attenuation. These results demonstrate that the experimental measurements in these slurries are rather reproducible.

Similarly, Figures 3.9, 3.10 and 3.11 show the average attenuation versus frequency curves, with error bars, for 10 %, 30 %, and 50 % (by volume) slurries, respectively, of Potter's Beads in a mixture of glycerin and water. In Figure 3.9, which shows the error in the 10 % Potter's beads slurry measurements, the error in the attenuation measurements is relatively small up to, and including, that at 3.0 MHz. At 3.0 MHz the relative error is 1.7 %, while at 3.5 MHz, the error jumps to 18 %. The error in the attenuation measurements at 3.5 MHz is more than 10 times that at 3.0 MHz. The error continues to increase with increasing frequency up to 32 % at 5.0 MHz. The error is considerably larger at frequencies above 3.0 MHz because these are the frequencies at which the operating ranges of the various transducers used in the measurements overlap. There often tend to be slight differences in measurements between the individual transducer pairs at overlapping frequencies, even though the results should ideally match. These differences are usually small enough so as not to present a problem from a reproducibility standpoint. However, because of the large particle size and density difference between the phases, the Potter's beads slurries are particularly difficult to

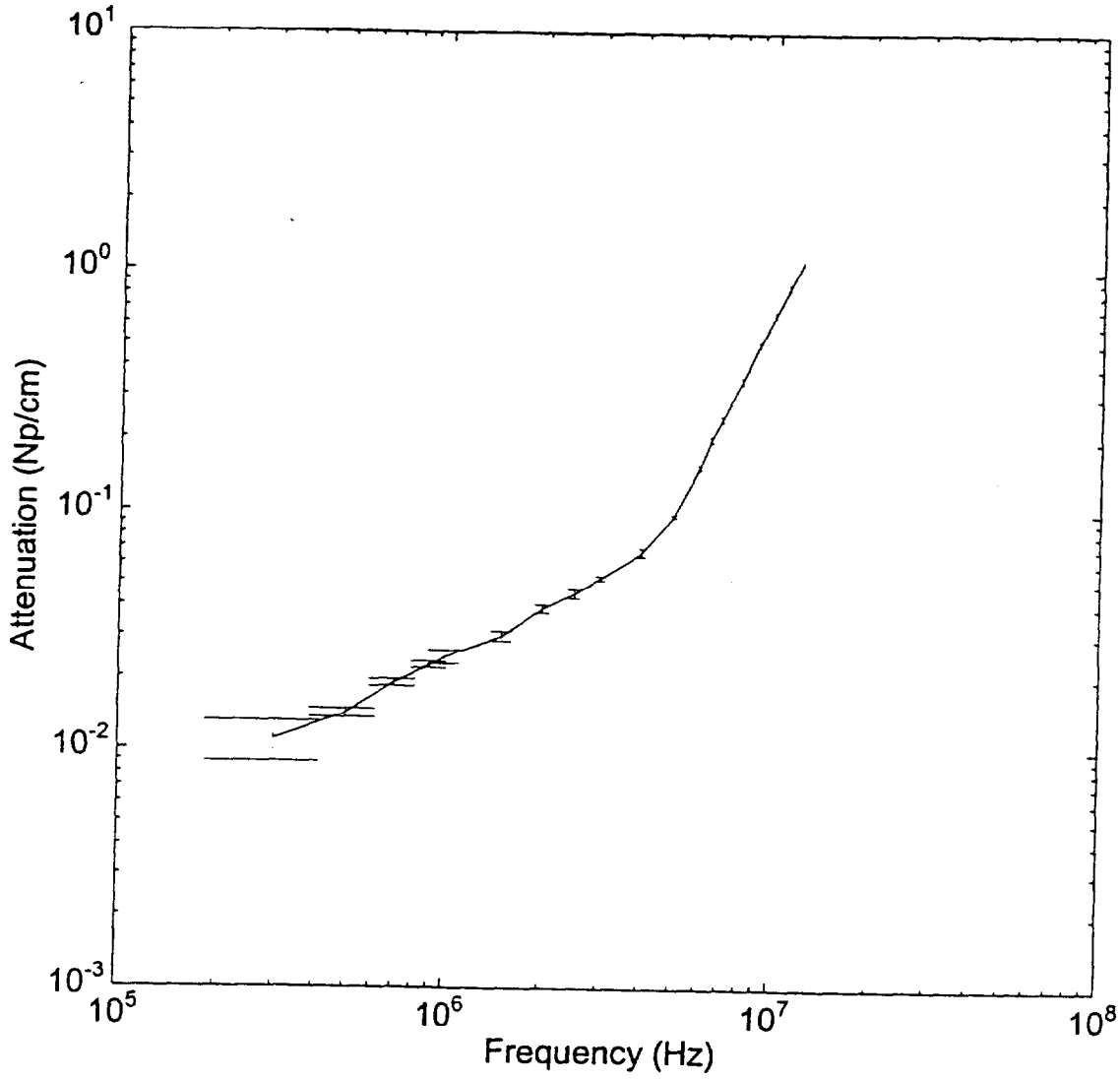

Figure 3.8: Mean attenuation versus frequency curve with error bars representing the average difference between individual attenuation values and the mean value. These data are for a 5 % (by volume) soda-lime glass slurry in water. - E1101.

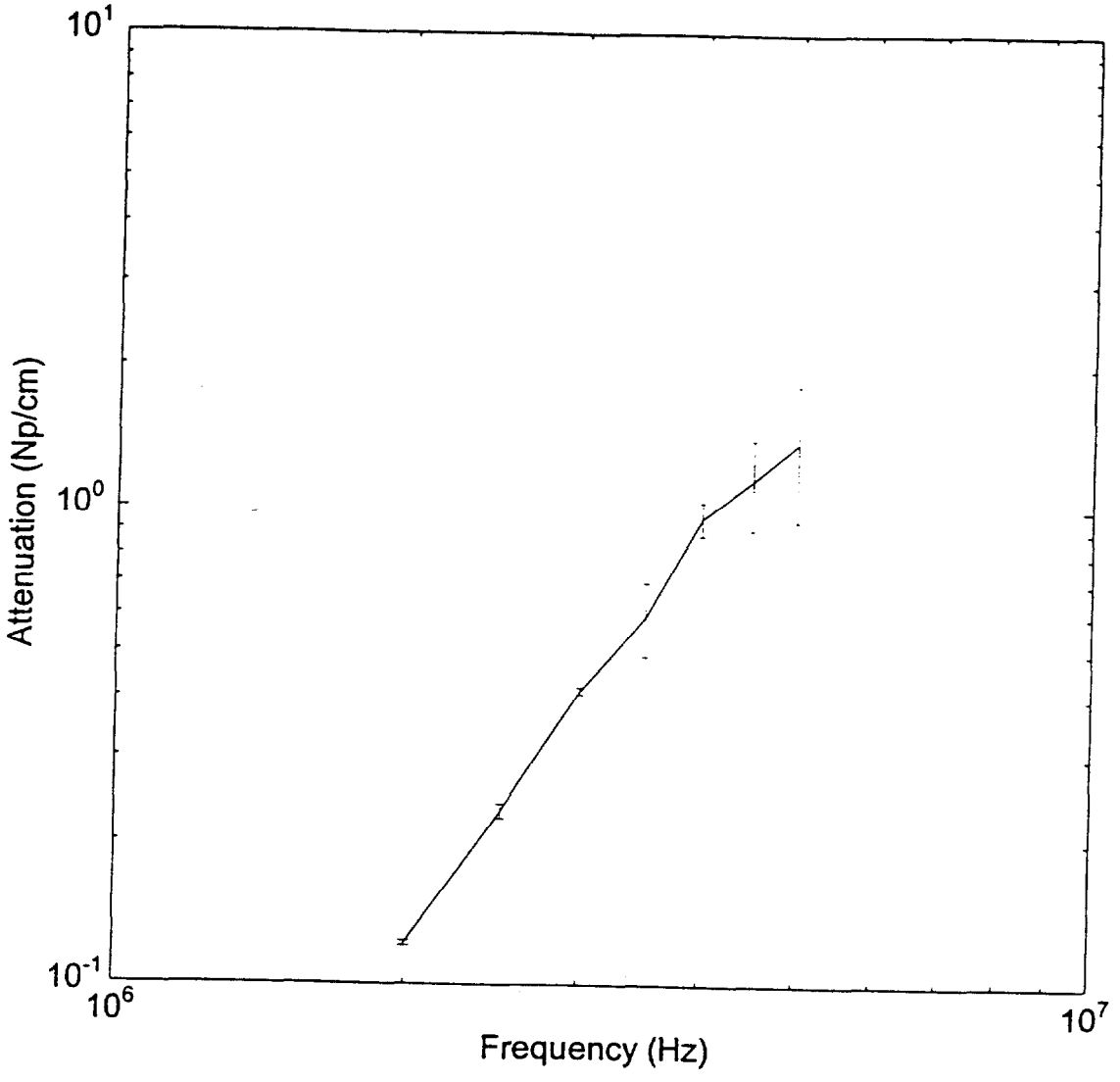

Figure 3.9: Mean attenuation versus frequency curve with error bars representing the average difference between individual attenuation values and the mean value. These data are for a 10 % (by volume) Potter's beads slurry in a mixture of glycerin/water. - E5182.

suspend uniformly. Therefore, any discrepancies between measurements will be amplified in the data for these slurries because of differences in the uniformity of the suspension.

A similar situation is seen for the 30 % Potter's beads slurry data shown in Figure 3.10. Here the error in the attenuation measurements becomes relatively large at 2.0 MHz, and at 3.0 MHz and 3.5 MHz. These frequencies also overlap in the operating ranges of the transducers used in these experiments. Therefore, as seen previously in Figure 3.9, there is an increased error at these frequencies because of differences in the results obtained by the different transducers.

Figure 3.11 shows the error in the attenuation measurements in a 50 % (by volume) Potter's beads slurry. The error in the measurements in the 50 % slurry appears to be more uniform relative to that in the 10 % and 30 % slurries in that there are no data points where the error band is exceptionally large. It is not clear why the error is more uniform for this slurry. One possible explanation could be that the data for the 50 % Potter's beads slurry are obtained in the test cell with the shortest acoustic path length (2.54 cm). It is possible that the slurry volume between the transducers in this test cell is small enough that there is more consistency in the slurry mixing conditions and solids concentration which are interrogated by the different transducer pairs.

In general it can be said that the experimental error is larger in the Potter's Beads slurries than in the soda-lime glass slurries. The largest relative error in the soda-lime glass beads slurries data is 19 % at 0.3 MHz where the attenuation is extremely small; while the 30 % Potter's Beads slurry measurements display an error as high as 32 % at

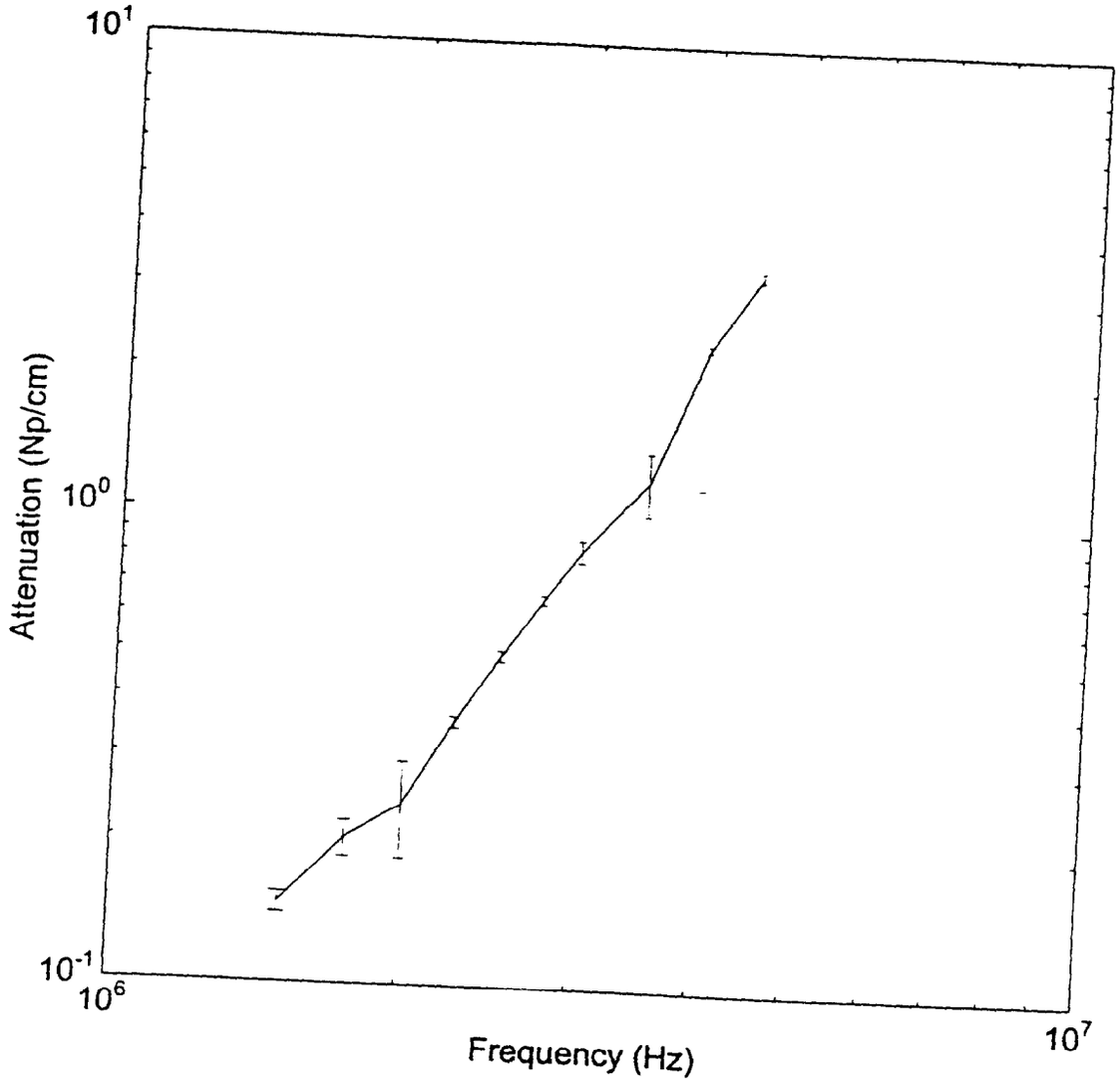

Figure 3.10: Mean attenuation versus frequency curve with error bars representing the average difference between individual attenuation values and the mean value. These data are for a 30 % (by volume) Potter's beads slurry in a mixture of glycerin/water. - E6192.

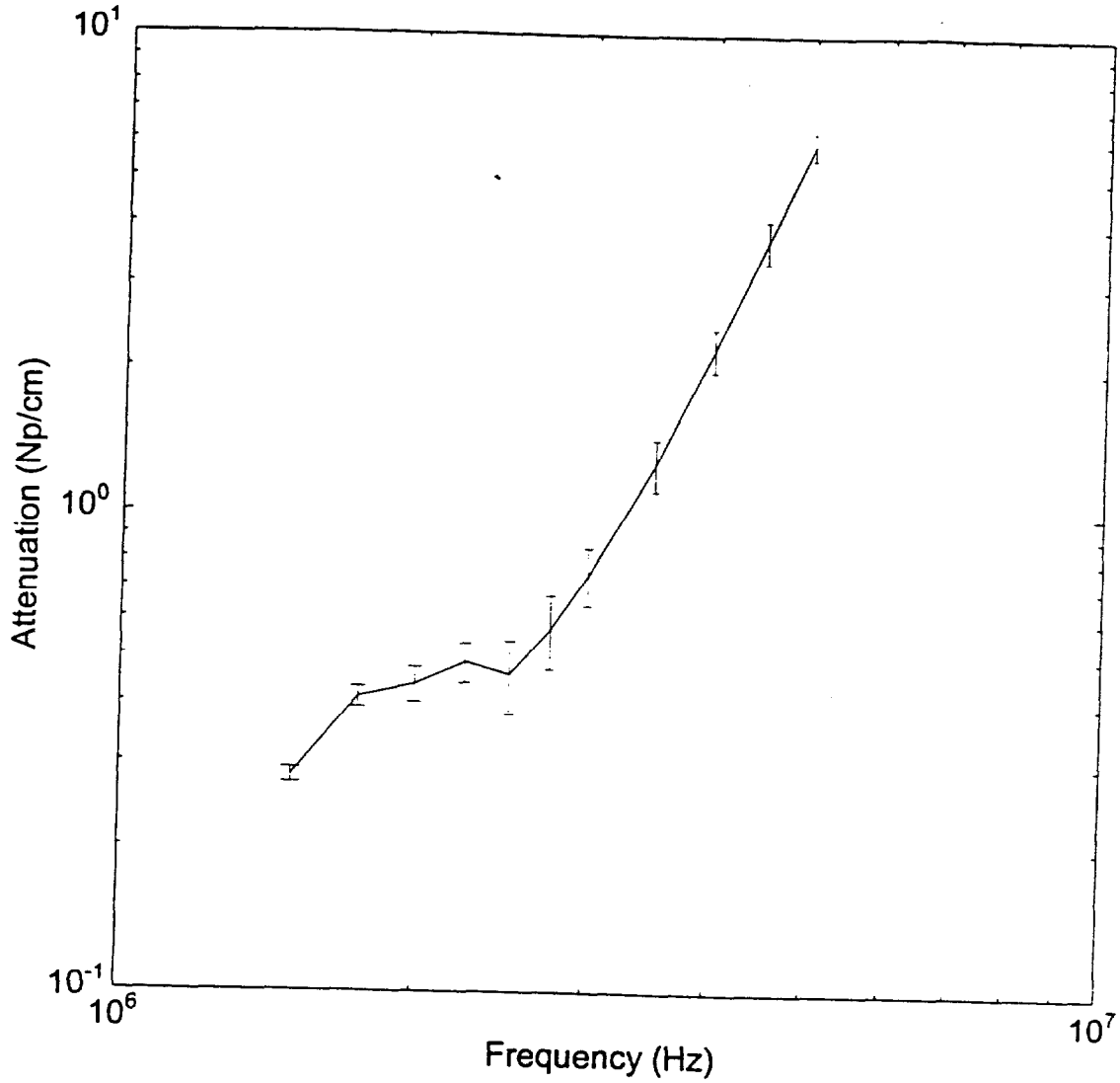

Figure 3.11: Mean attenuation versus frequency curve with error bars representing the average difference between individual attenuation values and the mean value. These data are for a 50 % (by volume) Potter's beads slurry in a mixture of glycerin/water. - E6112.

5.0 MHz. This larger error is, again, most likely due to variations in the mixing conditions in the Potter's Beads slurries caused by the combination of relatively large particle size and the density difference between the solid and liquid phases.

Chapter 4: Theory and Experiments for Dilute Solid-Liquid Suspensions

4.1 Theory for the Attenuation of Sound in Dilute Solid-Liquid Suspensions:

The determination of the acoustic response of a slurry given *a priori* details of its microstructure is referred to as the forward problem. When the total volume fraction of the solids is small, the problem is relatively simple since one only needs to understand the interactions between a single particle and an incident sound wave. This phenomenon has been studied by a number of investigators in the past with notable contributions from Epstein and Carhart (1953) and Allegra and Hawley (1972), who considered suspensions of particles as well as drops. Allegra and Hawley (1972) also reported experimental results verifying the theory for relatively small particles for which the acoustic wavelength is large compared with the particle radius. The theory developed by these investigators is quite general and accounts for attenuation by thermal, viscous, and scattering effects. This theory is briefly described in this chapter, and its predictions are compared with experimental data for dilute systems of polystyrene particles in water and soda-lime glass beads in water. A more complete description of the governing equations is given in Chapter 6, where a theory is developed for concentrated suspensions.

The wave equations for both the interior and exterior of the solid particles were initially derived by Epstein and Carhart (1953). These investigators first linearized the conservation equations for mass, momentum, and energy. The pressure and internal

energy are eliminated by introducing the linearized equations of state to yield equations in terms of density, velocity, and temperature. Next, the time dependence of all quantities is expressed by the factor $\exp(-i\omega t)$, which is henceforth suppressed. The velocity vector, **v**, can always be represented in terms of a scalar potential, Φ, and a vector potential, **A**, as

$$\mathbf{v} = -\nabla\Phi + \nabla\times\mathbf{A} \tag{4.1}$$

with $\nabla \bullet \mathbf{A} = 0$. With this form of **v** it is possible to eliminate the temperature and density from the governing equations to yield a fourth-order partial differential equation for Φ and a second-order equation in **A**. The former can be split in two second-order wave equations upon substitution of $\Phi = \phi_C + \phi_T$ (where ϕ_C and ϕ_T represent the scalar potentials of the compressional and thermal waves, respectively) to finally yield three wave equations:

$$\left(\nabla^2 + k_c^2\right)\phi_c = 0, \tag{4.2}$$

$$\left(\nabla^2 + k_T^2\right)\phi_T = 0, \tag{4.3}$$

$$\left(\nabla^2 + k_s^2\right)\mathbf{A} = \mathbf{0}, \tag{4.4}$$

The wavenumbers in the above equations are given by

$$1/k_c^2 = \frac{c^2}{2\omega^2}\left[1 - i(e+\gamma f) + \left((1-i(e+\gamma f))^2 + 4f(i+\gamma e)\right)^{1/2}\right], \tag{4.5}$$

$$1/k_T^2 = \frac{c^2}{2\omega^2}\left[1 - i(e+\gamma f) - \left((1-i(e+\gamma f))^2 + 4f(i+\gamma e)\right)^{1/2}\right], \tag{4.6}$$

$$k_s = (1+i)(\omega\rho/2\mu)^{1/2}, \qquad (4.7)$$

with

$$e \equiv (4\mu/3+\kappa)\omega/(\rho c^2); \quad f \equiv \sigma\omega/c^2 . \qquad (4.8)$$

Here, c is the phase speed in the pure liquid; ρ is the density; κ and μ are, respectively, the compressional and dynamic viscosities; $\gamma = C_p/C_v$ is the ratio of specific heats at constant pressure and volume; τ is the thermal conductivity; and $\sigma = \tau/\rho C_p$ is the thermal diffusivity.

Inside the particles similar equations hold with the dynamic viscosity replaced by $\tilde{\mu}/(-i\omega)$ and the wave speed by $\left(\left(\tilde{\lambda} + 2\tilde{\mu}/3\right)/\tilde{\rho}\right)^{1/2}$, where $\tilde{\mu}$ and $\tilde{\lambda}$ are the Lamè constants, and the compressional viscosity is left out. Henceforth, a tilde refers to the inside of the particles.

At small values of e and f (such as in water), the above expressions for k_C and k_T simplify to

$$k_c = \omega/c + \frac{i}{2}\left[\left(\frac{4}{3}\mu+\kappa\right)/\rho + (\gamma-1)\sigma\right]\omega^2/c^3 \qquad (4.9)$$

and

$$k_T = (1+i)(\omega/2\sigma)^{1/2} . \qquad (4.10)$$

Equation (4.2) and its counterpart inside the particles describe the sound wave propagation through the suspension. Note that the wavenumber has an imaginary part; sound waves in pure fluid are attenuated by viscous and thermal energy dissipation (Lighthill 1956); the term inside the square brackets in equation (4.9) is commonly

referred to as the 'diffusivity of sound'. The total attenuation coefficient in both the liquid and in the solid particle will henceforth be treated as additional physical properties. The other two wave equations describe waves that arise from thermal conduction and finite viscosity: we note that the modulus, k_T in equation (4.10), is inversely proportional to the thermal penetration depth, $\sqrt{\sigma/\omega}$, and that of k_S to the viscous penetration depth, $\sqrt{\mu/\rho\omega}$. The thermal (ϕ_T) and shear (**A**) waves have generally very high attenuation and are unimportant in acoustic applications.

Applying the boundary conditions of continuity of temperature, heat flux, velocity, and traction at the surface of the particles, and solving the resulting boundary problem numerically, it is possible to, in principle, determine the phase speed and attenuation at arbitrary volume fraction using the above formulation.

The potential, ϕ_C, outside a particle at $\mathbf{x}_1$ can be expressed as

$$\langle\phi_C\rangle(\mathbf{x}) = \exp(i\mathbf{k}_C \bullet \mathbf{x}) + \exp(i\mathbf{k}_C \bullet \mathbf{x}_1)\sum_{n=0}^{\infty} i^n (2n+1) A_n h_n(k_C r) P_n(\mu), \quad (4.11)$$

where $r = |\mathbf{x} - \mathbf{x}_1|$, $\mu = \cos\theta$, θ being the angle between $\mathbf{x} - \mathbf{x}_1$ and $\mathbf{k}_C$, h_n is the spherical Bessel function of the third kind (or Hankel function) corresponding to an outgoing scattered wave, and P_n is the Legendre polynomial of degree of n.

Inside the particle centered at $\mathbf{x}_1$ we have

$$\langle\tilde{\phi}_C\rangle(\mathbf{x}|\mathbf{x}_1) = \exp(i\mathbf{k}_C \bullet \mathbf{x}_1)\sum_{n=0}^{\infty} i^n (2n+1) \tilde{A}_n j_n(\tilde{k}_C r) P_n(\mu), \quad (4.12)$$

where j_n is the is the spherical Bessel function of the first kind. Similar expressions are written for ϕ_T and **A**. This results in expressions with a set of six unknowns for each mode n. Application of the boundary conditions of continuity of velocity, traction, temperature, and heat flux yield six equations in six unknowns for each n. There were some typographical errors in the equations given by Epstein and Carhart (1953) and Allegra and Hawley (1972); the correct equations are given in Appendix A. Although it is possible to solve for the unknowns analytically in certain limiting cases, it is best to solve them numerically since we are interested in covering a wide frequency range for later inverse calculations.

Once the coefficients are determined, the attenuation can be calculated using the result for the attenuation per unit length given by Allegra and Hawley (1972) as

$$\alpha = -\frac{3\phi}{2z^2 a}\sum_{n=0}^{\infty}(2n+1)\Re e A_n . \tag{4.13}$$

The above analysis can be extended in a straightforward manner to account for the particle size distribution when the total volume fraction of the particles is small. One may write the attenuation by the particles of radius between a and $a+da$ as an attenuation density $\hat{\alpha}(f,a)$ (where f is the frequency of the wave, $f = \omega/(2\pi)$) times the volume fraction of those particles, $\phi(a)da$. Here $\phi(a)$ is the particle volume fraction distribution. At low volume fractions these contributions can be "summed" over all particle sizes to give the total attenuation $\alpha_{tot}(f)$:

$$\alpha_{\text{tot}}(f) = \int_{a=0}^{\infty} \hat{\alpha}(f,a)\phi(a)da \qquad (4.14)$$

It should be noted that it is customary to express the particle size distribution in terms of its number density distribution $P(a)$. The volume fraction distribution is related to $P(a)$ by $\phi(a) = \left(4\pi a^3/3\right)P(a)$.

4.2 Attenuation Measurements in Dilute Solid-Liquid Systems:

4.2.1 Attenuation in Soda-Lime Glass Bead Slurries:

Attenuation data plotted as a function of frequency for soda-lime glass beads at 5 % and 10 % by volume are shown in Figure 4.1. These data are collected in the 1.6 L PVC vessel by the Toneburst measurement technique. These experimental results are plotted along with results of the forward problem calculation based on the theory of Allegra and Hawley (1972) for log-normal distribution of particle sizes. The forward problem calculation used a particle radius of 14 μm with a standard deviation of 7 μm. The actual solids radii range from 0.5 μm to 18 μm, with mean radius at 9 μm. It is clear from this figure that the agreement between theory and experiment is excellent.
It is interesting to note in this figure the pronounced change in the slope of the attenuation curve. This change in slope occurs where the dominant attenuation regime changes from the inertial regime (Kytomaa 1995) to the geometric scattering regime. The theory predicts that the slope of the attenuation curve should be ½ ,before the transition and four afterwards. That is, the attenuation should scale as $f^{1/2}$ before the

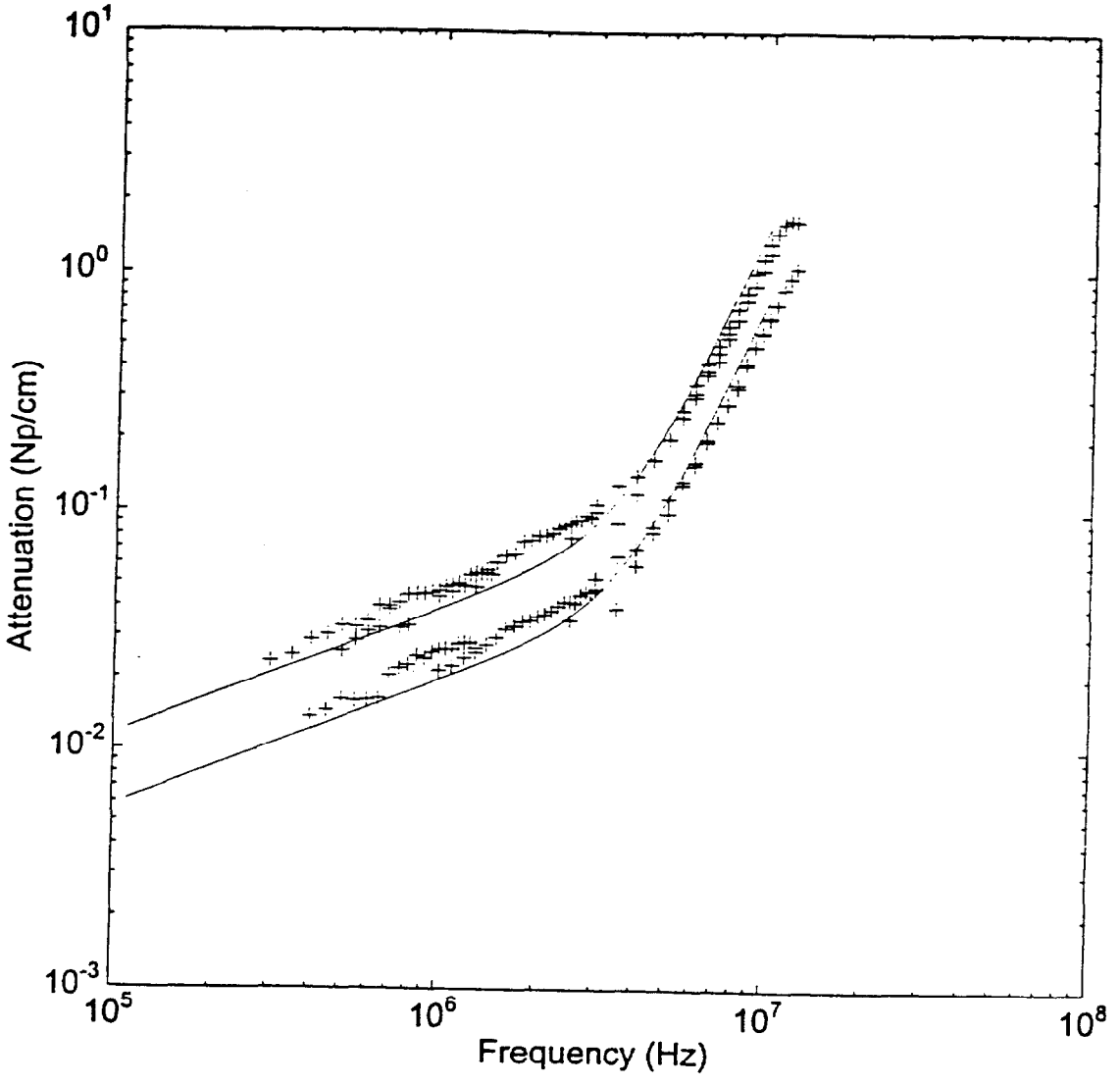

Figure 4.1: Comparison between experimental results and forward problem theory predictions for the attenuation versus frequency curves for soda-lime glass slurries at 5 % (lower curve) and 10 % solids by volume. The experimental solids size distribution has a mean radius of 14.9 μm with standard deviation of 3.56 μm. The forward theory predictions are based on a log-normal distribution with a mean radius of 14 μm and standard deviation of 7 μm. - E1101.

transition and f^4 afterwards. However, if one examines the experimental data it can be seen that the data in the inertial regime do scale as $f^{1/2}$, but the data in the scattering regime scale with frequency more like f^3. At first it was thought that this difference occurred because the soda-lime glass particles are polydispersed, but this behavior is seen in theoretical calculations even for monodispersed particles. This behavior is actually due to contributions from more than one mode of resonance, which shall be discussed in more detail in the next section.

4.2.2 Attenuation in Polystyrene Bead Slurries:

Figure 4.2 shows the attenuation as a function of frequency for 79 μm radius "monodispersed" polystyrene beads. These data are obtained in the 2.54 cm nominal path length Plexiglas test cell using both the Toneburst and the Pulse/FFT measurement techniques. These data are also compared with several different results of the forward problem theory using different input particle size distributions. Good agreement is seen between experiments and the theory except near the resonance frequencies where small differences appear. The differences were initially thought to possibly be due to finite volume fraction effects, but when the attenuation is calculated using an effective medium approach, shown by a dash-dot line in Figure 4.2, the attenuation actually shifts in a direction which increases the differences . Therefore, the differences probably occur because the particles are not exactly monodispersed. The theory for a monodispersed dispersion, shown by the solid line in Figure 4.2, also shows a difference from experimental data. However, when the theory calculations are performed using a particle

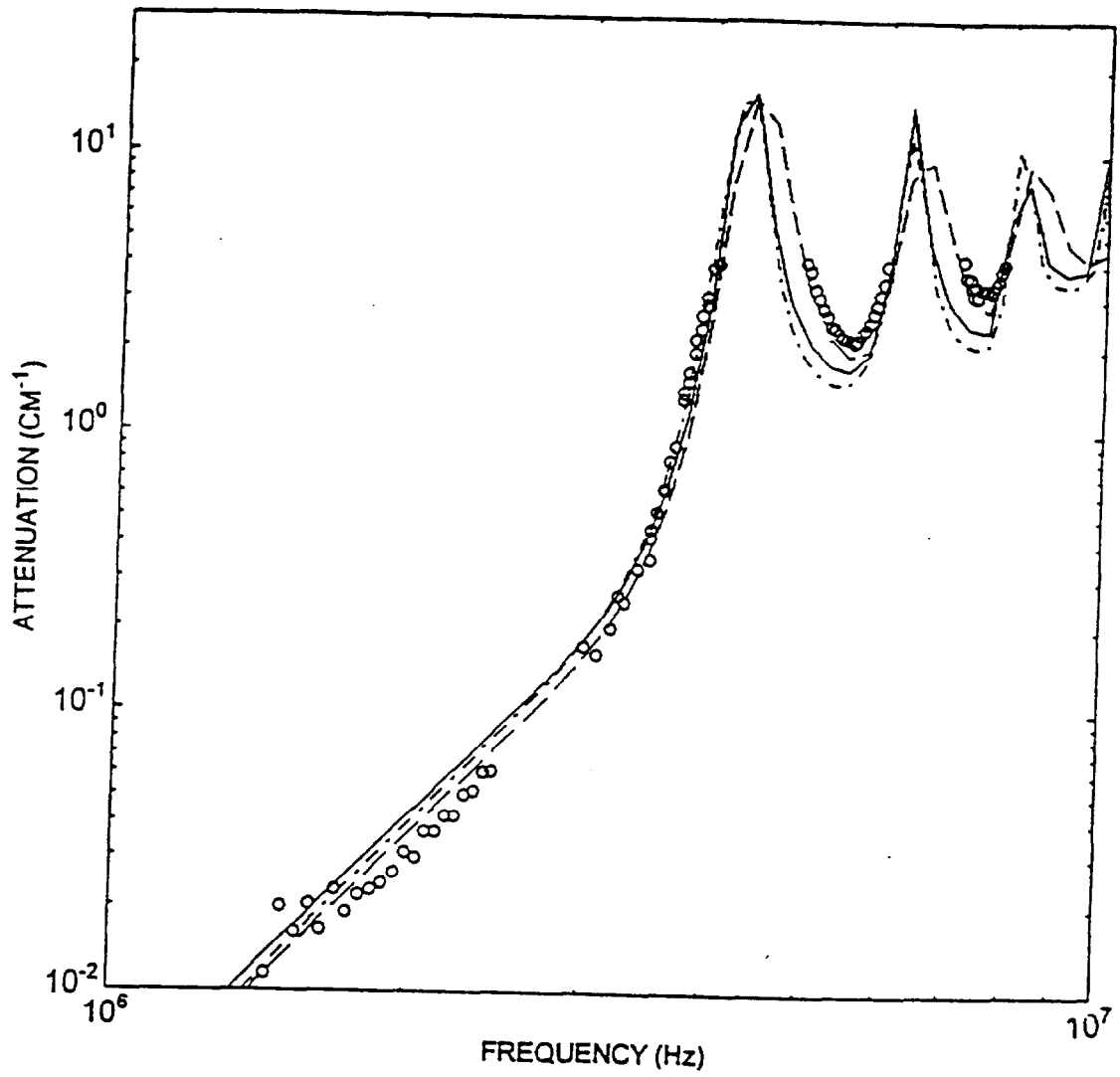

Figure 4.2: Comparison of forward theory with experimental data for the attenuation as a function of frequency. These data are for polystyrene particles of radius a = 79 μm, at 5 % by volume. O, experimental data; —, theory for monodispersed particles; -.-.-, theory for monodispersed particles with effective medium correction for finite volume fraction effects; - - -, theoretical result with a particle size distribution with a mean radius of 79 μm and standard deviation of 2.5 μm (this is the particle size range specified by the particle manufacturer). - E2363.

size distribution with a mean diameter of 154 μm with a standard deviation of 5 μm, (which lies within the manufacturer's specifications) the result for the attenuation, which is shown as a dashed line in Figure 4.2, shows excellent agreement with the experimental data. Thus, it can be concluded that the small observed differences are due to the polydispersity of the dispersion.

It is important to note the several peaks and troughs in the plot at frequencies above approximately 3 MHz. These peaks and troughs are caused by the various modes of resonance which the particles undergo. Each peak corresponds to dominance by a different mode of resonance.

These transitions to dominance by the different modes of resonance are also responsible for the slope in the scattering regime never truly achieving an f^4 dependence. The Lengendre polynomials in the equations for the potential describe the contributions to the attenuation from the various modes of oscillation which the particles can undergo. The $n = 0$ mode corresponds to radial (volume) oscillations. The $n = 1$ mode corresponds to translational oscillations. The $n = 2$ mode corresponds to ellipsoidal P_2-shape oscillations, and so on. Figure 4.3 shows the contributions to the total attenuation as calculated for the polystyrene particles used in the experiments from the forward problem theory. The density of polystyrene particles is essentially the same as that of water, and so the translational oscillations of the particles are small. Therefore, the viscous attenuation is small, and the low frequency behavior is governed by the thermal attenuation of the $n = 0$ mode (volume oscillations). At higher frequencies the $n = 0$ mode increases first as f^4 due to scattering losses, but the contribution from the $n = 2$

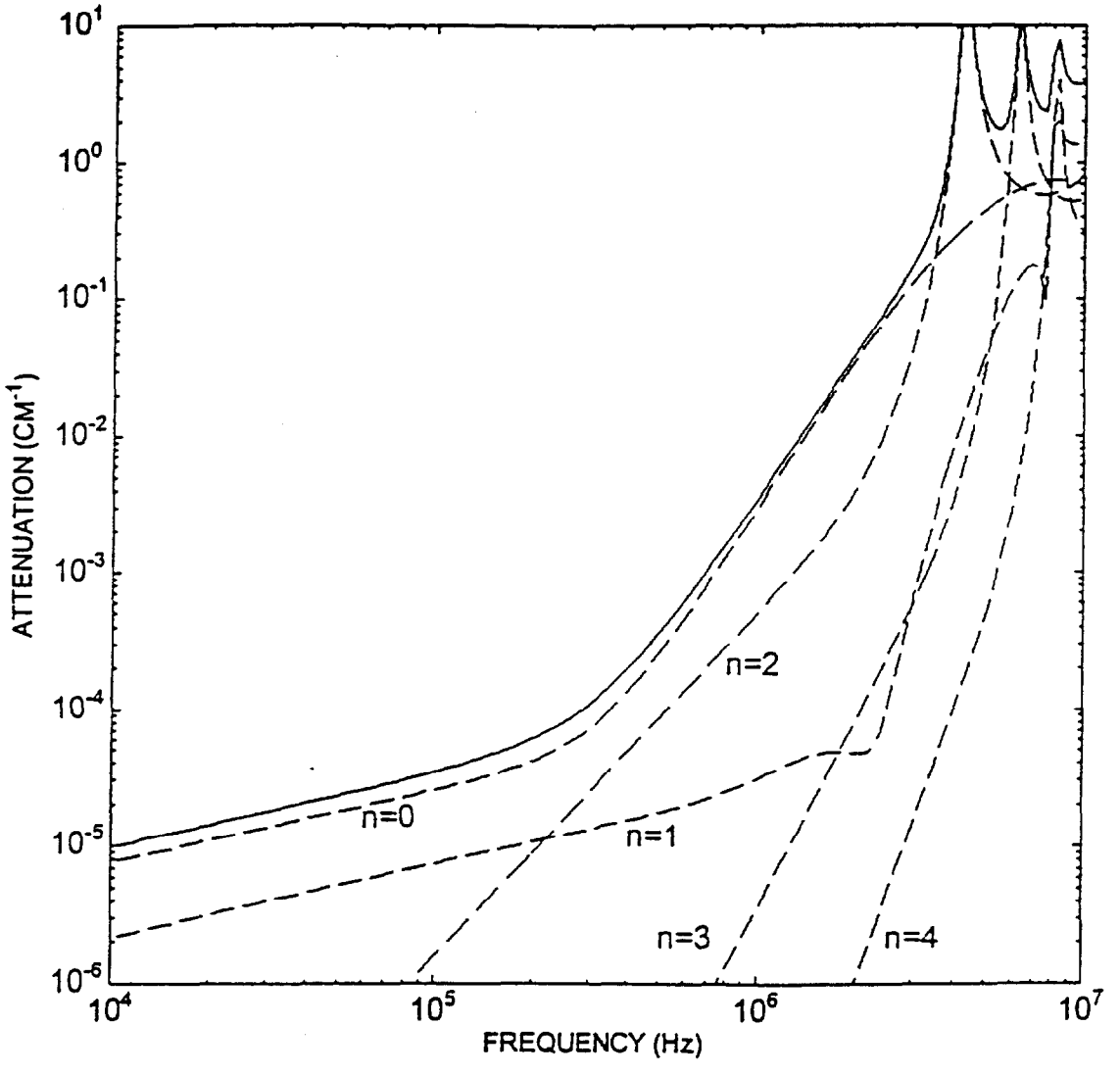

Figure 4.3: Contributions of the first five modes of resonance (n =1 through 5) to the total attenuation (the imaginary part of k_{eff}) for 79 μm radius polystyrene particles in water.

mode (ellipsoidal oscillations) soon becomes important as it undergoes resonance at about 3 MHz. In the figure we see that the $n = 3$ and $n = 1$ modes undergo resonance next, etc. Therefore, the attenuation never really achieves the f^4 dependence that would be predicted by the scattering theory; but rather, it displays the combined behavior shown in Figure 4.4. Thus, it can be said that the resonance frequencies of the various modes of oscillations cause the high frequency behavior of the polystyrene particles to become quite complicated.

It should be noted that the reason why the peaks appear truncated, in the region where the theory predicts very high peaks in the attenuation, is because in those regions the attenuation increases dramatically to levels which are beyond the measuring capabilities of the instrumentation used in this study.

In contrast, these peaks and troughs do not appear in the attenuation behavior predicted by the theory of Allegra and Hawley (1972) for soda-lime glass particles. This behavior is shown in Figure 4.5. Unlike the polystyrene data, the attenuation data for the soda-lime glass particles do not peak at several different frequencies. Rather, for each mode n we see broad "hills" separated by narrow "valleys". The total attenuation does not appear to go through several resonances, but instead has one broad "overall" peak which is a mean contribution, of sorts, of all the individual resonance behaviors. The difference between the behavior for the polystyrene and soda-lime glass particles at the higher frequencies seems to arise mainly from the different elastic properties of the two materials. Also, the density of the soda-lime glass particles is significantly different from that of water. The soda-lime glass particles exhibit significant translational oscillations.

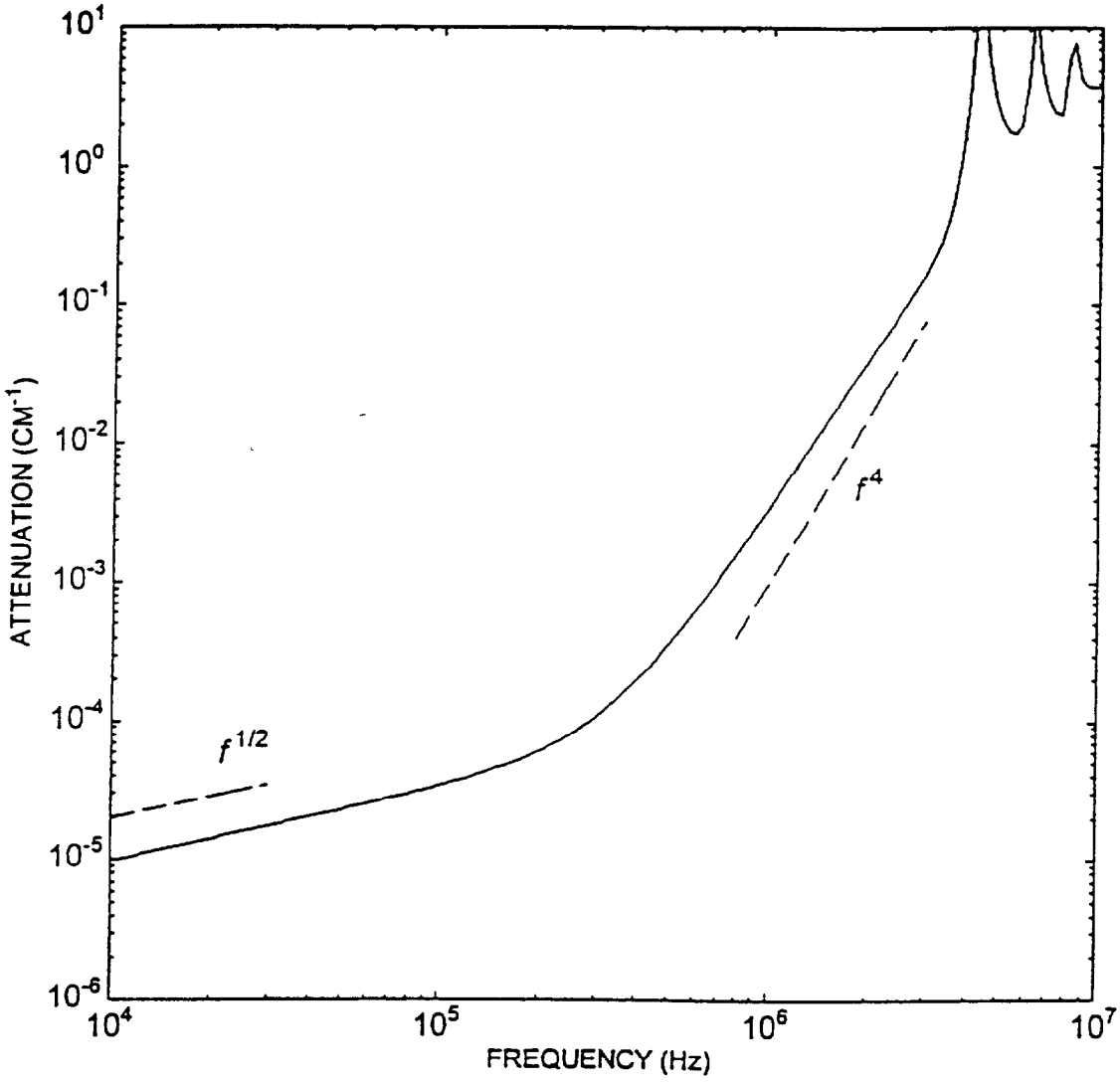

Figure 4.4: Example of the dependence of attenuation on frequency, f, for a slurry of polystyrene particles in water. Dashed lines are asymptotic slopes of the attenuation for low and high frequencies.

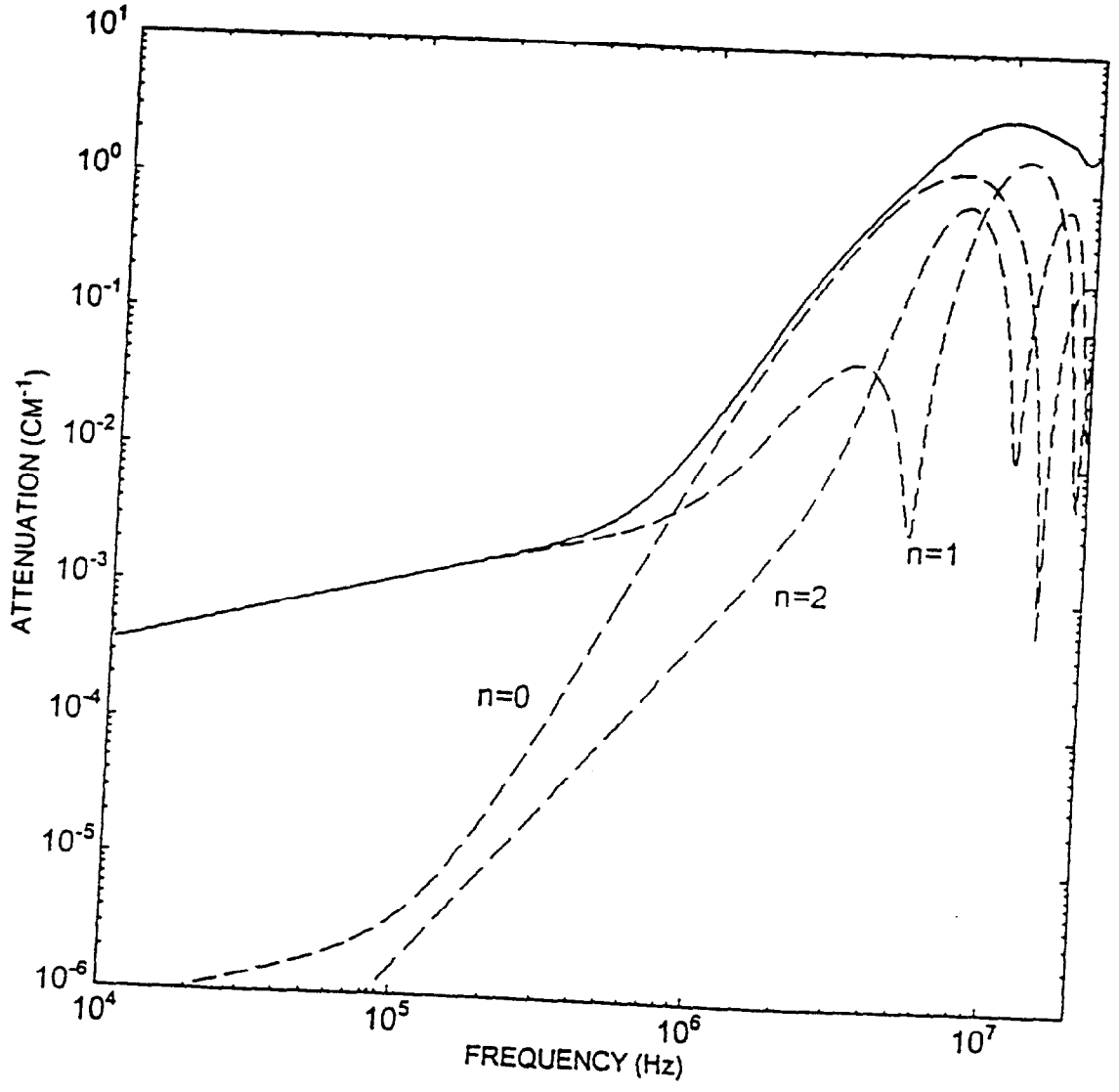

Figure 4.5: Contributions of the first three modes of resonance (n =1 through 3) to the total attenuation (the imaginary part of k_{eff}) for 79 μm radius monodispersed glass particles in water.

As a result, the low frequency behavior is completely governed by the viscous effects and the $n = 1$ mode. It should be noted that small frequency attenuation is about two orders of magnitude greater for the soda-lime glass particles than for the polystyrene particles.

Chapter 5: Inverse Problem for Determination of Particle Size Distributions

5.1 Inverse Problem Theory:

Determining the particle size distribution of a solid-liquid suspension is of great practical interest. It has been suggested in the literature that this distribution may be determined by measuring the attenuation of a sound wave propagating through the suspension as a function of the frequency of the wave. The main premise is that the attenuation caused by a particle as a function of frequency depends on its size; and, therefore, the attenuation measurements can be inverted to determine the particle size distribution -- at least when the total volume fraction of the solids is small enough such that particle interactions and detailed microstructure of the suspension play an insignificant role in determining the acoustic response of the suspension. Indeed, this general principle has been exploited successfully to determine the size distribution of bubbles in bubbly liquids (Commander and McDonald (1991); Duraiswami (1993); and Duraiswami *et al.* (1998)). Commercial "particle sizers" based on acoustic response are in the process of being developed/marketed for characterizing solid-liquid mixtures (Oja and Alba (1997)). The main objective of this chapter is to investigate under which circumstances such a problem can be solved for solid-liquid systems. The attenuation is predicted in the calculations from the linear theory of Allegra and Hawley (1972). It will be shown that the success of the acoustic method for determining detailed particle size

distributions is limited, depending on the nature of the particles and the frequency range over which the input (attenuation) data are available.

We now consider the inverse problem. That is, given only the total attenuation α_{tot} as a function of f, it is desirable to determine $\phi(a)$ using equation (4.13). Inverse techniques have been explored by many investigators with regard to the acoustic evaluation of dispersed phase systems.

Duraiswami (1993), after exploring a number of possible regularization strategies such as truncated singular value expansion, moment collocation techniques, and Tikhonov regularization and optimization, employed a Tikhonov regularization scheme and optimization to solve the inverse problem of determining the size distribution of bubbles in bubbly liquids from measurements of attenuation and change in phase speed. The basic idea behind the Tikhonov regularization technique is that the problem is formulated in such a way that the norm of the solution and the norm of the residual error are sought to be minimized. This technique also takes advantage of the fact that the bubble size distribution function is generally a smooth function. Further details of this technique will be discussed later in this chapter.

This type of straightforward method of solving the integral equations, i.e., discretizing the integral domain into a number of elements and converting the integral equation into a system of linear equations in unknowns $\phi(a_k)$ at a selected number of points a_k in the domain, cannot be used in the solid-liquid slurry inverse problem since the resulting equations will be ill-posed. Figures 5.1a & b illustrates the ill-posed nature of the problem. Figure 5.1a shows two very different particles size distributions

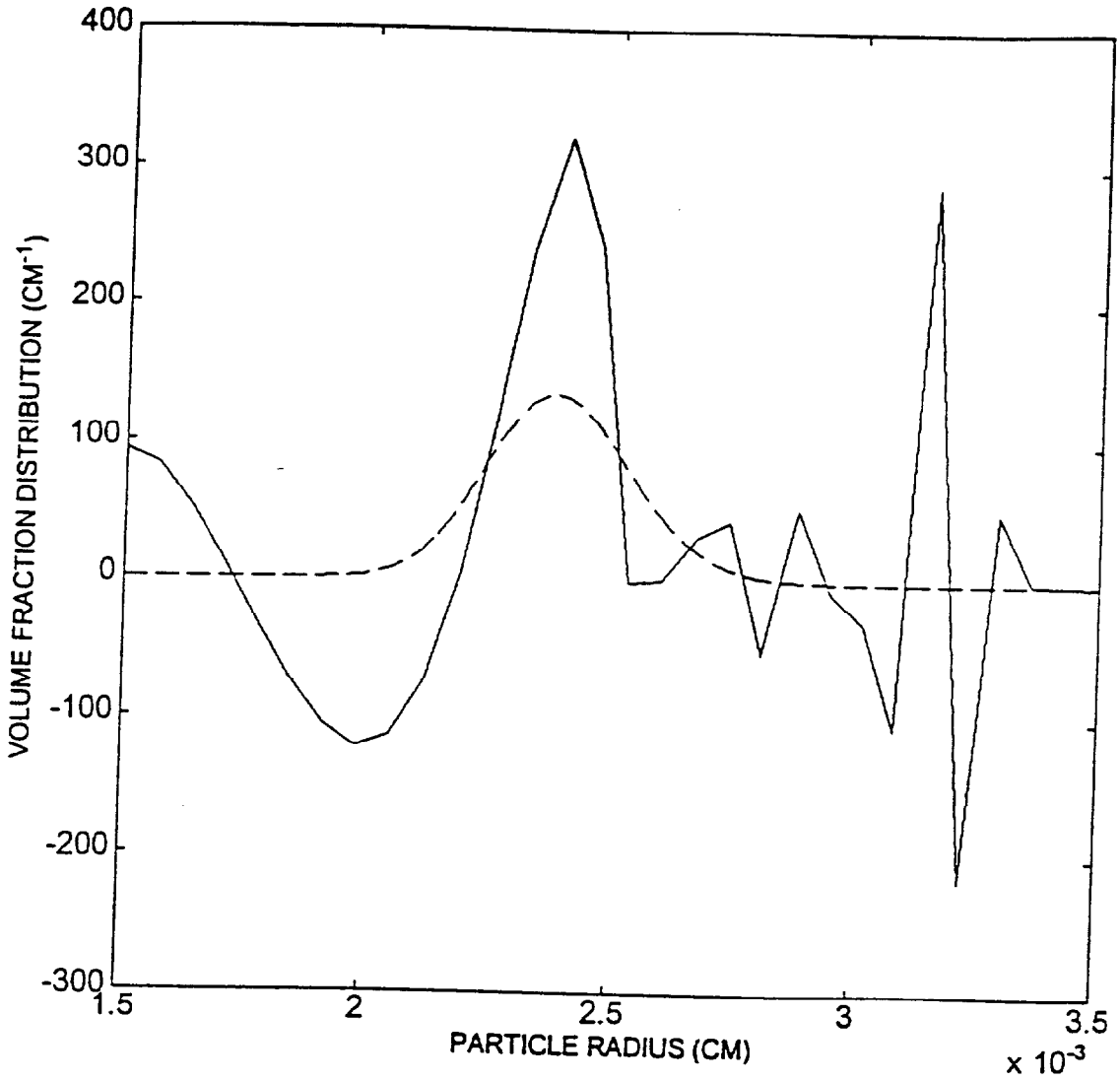

Figure 5.1a: Two significantly different particle volume fraction distributions which yield similar attenuation spectra.

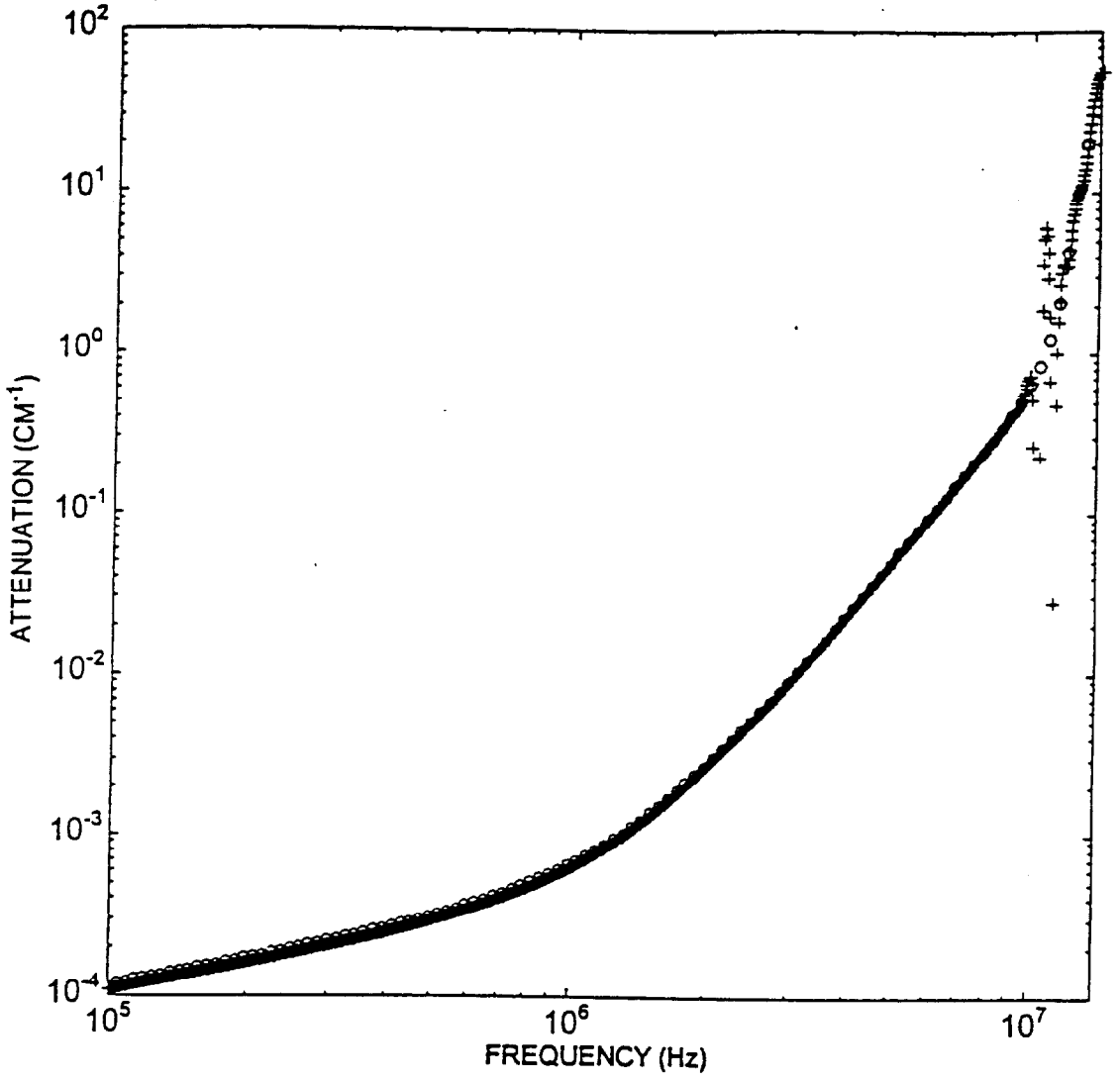

Figure 5.1b: Attenuation spectra obtained from the volume fraction distributions in Figure 5.1a. The circles correspond to the results obtained when using the distribution shown by a dashed line in Figure 5.1a, and the crosses correspond to the result obtained when using the distribution shown by the solid line in Figure 5.1a.

whose attenuation spectra, shown in Figure 5.1b, are seen to be essentially the same. These two curves were obtained by starting with a smooth, log-normal particles size distribution (dashed curve in Figure 5.1a) and generating the attenuation versus frequency data using the forward theory (circles in Figure 5.1b). A random noise of 1 % was then added to the data, and equation (5.2) with $\varepsilon = 0$ (which is equivalent to integral equation (4.13)) was subsequently solved to yield the particle size distribution indicated by the solid line in Figure 5.1a. The crosses in Figure 5.1b correspond to the attenuation spectrum determined from the forward theory using the new particle size distribution. It should be noted that the attenuation is evaluated with a smaller frequency increment than the one used for the original distribution. It is seen that the attenuation from the two distributions agree with each other to within 1 % for the frequencies marked by the circles. The attenuation spectrum for the latter particle size distribution does exhibit an oscillatory behavior in between the frequency increments, particularly at 10 MHz, but these oscillations occur only for a very narrow frequency range and would have been missed altogether had the attenuation been determined at only the input frequencies.

Since the true particle size distribution is expected to be smooth, only solutions which are reasonably smooth can be permitted. This restriction may be imposed in several ways. In the present study, the primarily used regularization technique is that due to Tikhonov (Kress 1989) which was successfully used for bubbly liquids by Duraiswami (1993). An alternative method is presented at the end of this section. Accordingly, equation (4.13), which is based on the theory of Allegra and Hawley (1972), is multiplied

with $\hat{\alpha}(f,a)df$ and integrated over the frequency range to obtain a simpler integral equation in which the right-hand side is only a function of a:

$$\int_{f_{\min}}^{f_{\max}} \int_{a_{\min}}^{a_{\max}} \hat{\alpha}(f,a)\,\hat{\alpha}(f,a')\phi(a')da'df = b(a) \equiv \int_{f_{\min}}^{f_{\max}} \alpha_{\text{tot}}(f)\,\hat{\alpha}(f,a)df\,, \tag{5.1}$$

where ($a_{\min}$, $a_{\max}$) and ($f_{\min}$,$f_{\max}$) are the radius and frequency ranges. The above integral equation is now regularized as explained below by adding a small term $\varepsilon\left(\phi - l^2\phi''\right)$ (where primes denote derivatives) to its left-hand side. Thus,

$$\varepsilon\left[\phi(a) - l^2\phi''(a)\right] + \int_{a_{\min}}^{a_{\max}} K(a,a')\phi(a')da' = b(a), \tag{5.2}$$

is obtained, where l is a suitably chosen length scale and $K(a,a')$ is a kernel defined by

$$K(a,a') = \int_{f_{\min}}^{f_{\max}} \hat{\alpha}(f,a)\,\hat{\alpha}(f,a')df\,. \tag{5.3}$$

Equation (5.2) is an integro-differential equation and needs two boundary conditions. Usual practice is to take the derivative of $\phi(a)$ to be zero at the two end points:

$$\phi'(a_{\min}) = \phi'(a_{\max}) = 0\,. \tag{5.4}$$

It should be noted that $a_{\min}$ and $a_{\max}$ are not, in general, known *a priori*. One expects ϕ to also be zero at the two end points. Thus, the range ($a_{\min}$ - $a_{\max}$) must be determined by trial

and error so that both ϕ and its derivatives are approximately zero at the extreme values of a.

Now it can be shown that the solution of equation (5.2) subject to the boundary conditions given by equation (5.4) minimizes

$$E + \varepsilon \int_{a_{\min}}^{a_{\max}} \left[\left\{ \phi(a) \right\}^2 + l^2 \left\{ \phi'(a) \right\}^2 \right] da, \tag{5.5}$$

where E is the measure of error between the actual attenuation and the computed attenuation:

$$E = \int_{f_{\min}}^{f_{\max}} \left| \int_{a_{\min}}^{a_{\min}} \hat{\alpha}(f,a)\phi(a)da - \alpha_{\text{tot}}(f) \right|^2 df. \tag{5.6}$$

Since both E and the second term in equation (5.5), i.e., the integral, are non-negative, minimization of equation (5.5) ensures that the solution of equation (5.2) will be free from large oscillations in ϕ. In other words, highly oscillatory distributions such as the one shown in Figure 5.1a. are rendered inadmissible when equation (5.2) is solved with finite, positive ε in place of the original integral equation (5.1). Thus, we have regularized the problem of determining ϕ.

If a large ε is chosen, then the oscillations in ϕ decrease, but increase the error in $\phi(a)$ increases since then the equation solved is significantly different from the original integral equation. Small ε, on the other hand, yields unrealistic $\phi(a)$ having large oscillations when the data $\alpha_{tot}(f)$ are not exact. An optimum choice of ε, therefore, depends on the magnitude of the uncertainty or error in the measured attenuation versus frequency

data.

5.2 Inverse Problem Calculation Results:

The theoretical calculations which accompany the experimental results in this dissertation are performed by Dr. Peter D.M. Spelt and Professor Ashok S. Sangani at Syracuse University. Both the theoretical study and computations are performed by these individuals as part of the overall Acoustic Probe Development Project being funded by the US DOE Environmental Management Science Program Grant # DE-FG07-96ER14729. A formal presentation of the theoretical and computational work presented herein may be found in Spelt *et al.* (1998).

As mentioned in the previous section, an optimum choice of parameter, ε, depends on the magnitude of the uncertainty or error in the attenuation versus frequency data. This concept is tested by first determining the exact $\alpha_{tot}(f)$ using the forward theory for a given $\phi(a)$ with a small random noise of about 1 % magnitude added to it before the inverse calculations are performed. This random noise is introduced to simulate the error which would be present in experimentally obtained attenuation versus frequency data. To obtain the optimum value of ε, equation (5.2) is solved for several different ε's, and the error E is plotted versus ε to find a minimum value of E. This minimum value of E, however, may lead to volume fraction distributions in which $\phi(a)$ may have physically unrealizable negative values for some values of a. To prevent the realization of this possibility, the constraint $\phi(a) \geq 0$ for all a is satisfied *a posteriori* by

setting $\phi(a) = 0$ for all a's for which the solution of equation (5.2) yields negative values of $\phi(a)$. Thus, the computed value of E is based on $\phi(a) \geq 0$.

The integro-differential equation (5.2) was solved in the following manner. After discretizing the domain (a_{min} to a_{max}) into N - 1 equal segments and the frequency domain into M - 1 logarithmically equal segments the kernel $K(a_i, a_j)$, is first evaluated for i, j = 1, 2,..., N (cf. equation 5.3) using a trapezoidal rule for the integration over the frequency range. As was indicated by Duraiswami (1993) it is important to calculate the integral over the particle radius rather accurately. Thus, it was assumed that $\phi(a)$ varied in a piecewise continuous manner in each segment, and a 12-point Gauss-Legendre quadrature was used to evaluate the integral in equation (5.2). A second-order central difference formula was used to evaluate $\phi''(a)$ at all points except the endpoints a_{min} and a_{max}. The boundary conditions $\phi'(a_{\min}) = 0$ and $\phi'(a_{\max}) = 0$ were approximated using, respectively, second-order forward and backward difference formulae. Application of equation (5.2) at all the discretization points together with the boundary conditions can be expressed with the above scheme as a system of linear equations:

$$\sum_{j=1}^{N} A_{ij}\phi_j = b_i \qquad i = 1,2,...,N\ , \tag{5.7}$$

where $\phi_j = \phi(a_j)$ and $b_i = b(a_i)$. The above set of equations was then normalized by dividing all the equations by the greatest element of the kernel, $K(a_i, a_j)$, K_m for all i, j, times the segment length, $\Delta a = (a_{\max} - a_{\min})/(N-1)$. This set of equations was subsequently solved using a standard IMSL subroutine for linear equations.

Once the ϕ_j are determined for a selected value of ε, the constraint $\phi_j \geq 0$ is satisfied by setting, as was mentioned previously, all $\phi_j = 0$ for all negative values of ϕ_j. The error, E, as given by equation (5.6), was subsequently evaluated using a trapezoidal rule for integration over the frequency range. The optimum value of ε was determined by stepping logarithmically through several values of ε and plotting E versus ε.

A typical result ($N = 30$, $M = 112$, $f_{min} = 0.1$ MHz, $f_{max} = 17$ MHz, $a_{min} = 15$ μm, and $a_{max} = 35$ μm) for the error in the resulting attenuation as a function of ε is shown in Figure 5.2. It should be noted that here ε is actually the value of ε divided by $K_m \Delta a$. Upon examining Figure 5.2, one can see a clearly defined optimum value of ε. Computations were also made with larger M to confirm that the resulting volume fraction distribution was not affected by the further refinement in the integration over the frequency range.

It should be noted that both ε and l are parameters which were chosen so as to minimize the error E. The value for l was taken as $l = (a_{max} - a_{min})/n$, and E was computed by varying both ε and n. The value of n was varied from 1 to N. It was found that when E was plotted versus n and ε, E was much more sensitive to ε than it was to n. In general, it was found that the results where n was close to N were slightly better than those where n was close to unity. Therefore, n was chosen to equal 30. For larger values of N ($N > 40$), it was found that choosing $n = N$ led to more oscillatory behavior for ϕ_j. This behavior is to be expected since choosing a larger value of n, and hence, a smaller value of l will permit larger values of $\phi'(a)$.

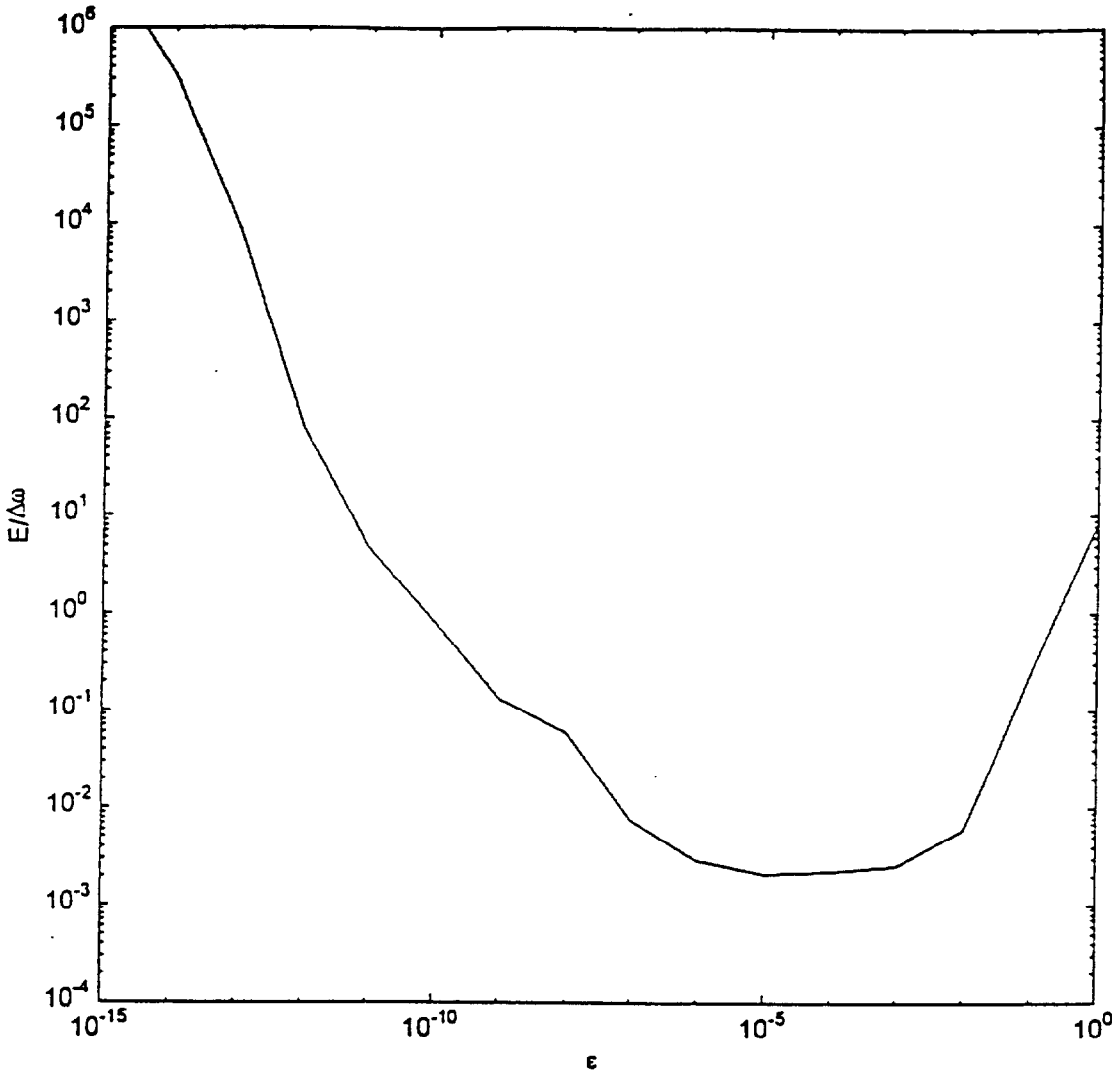

Figure 5.2: Error in the attenuation as a function of ε.

In order to obtain the results for the volume fraction distribution using the above mentioned regularization technique, the forward theory was used to first generate attenuation data for an assumed volume fraction distribution. Small random noise was added to the generated data to mimic experimental error in measured attenuation data. If the procedure fails for the generated data with small amount of noise added, it would certainly fail for any real experimentally obtained data.

The calculation is initially performed for a frequency range of 0.1 to 15 MHz in order to investigate the success and limitations of the technique. This range roughly coincides with the range of frequency employed in the attenuation measurement experiments. Also considered is a larger range of frequency to determine if better estimates of the particle volume fraction distribution could be achieved if the attenuation data at higher frequencies were available. The examination of higher frequency results is important because there are commercially available acoustic probes which can operate at frequencies up to 150 MHz.

The particle sizes first considered are those which are of the same order of magnitude as the wavelength of the sound waves somewhere in the above mentioned frequency range. This requirement is satisfied for particles of size about 10 to 100 μm in radius. It should be noted that particles of larger sizes would merely shift the observed behavior to the left in an attenuation versus frequency plot. The smooth particle volume fraction distribution (dashed line) in Figure 5.1a shows an example of a log-normal particle size distribution which is employed because it is a commonly used and smooth distribution. As in the forward problem calculations, the inverse problem calculations are

performed for polystyrene and soda-lime glass particles. These two types of particles form a good basis for examination of the capabilities and limitations of the inverse problem technique because the polystyrene particles are almost neutrally buoyant with respect to water and deformable, while the soda-lime glass particles are much more dense than water and quite rigid. The physical properties of these two materials are shown in Table 3.2 in Chapter 3.

The first volume fraction distribution results obtained from the inverse problem are shown in Figure 5.3. These results are for polystyrene particles with a narrow size distribution in the range of 20 to 30 μm in radius. However, the particle size range initially employed was somewhat larger, ranging from 5 to 100 μm in radius; and the frequency range was 0.1 to 17 MHz. The results for this particle size range are shown in Figure 5.3, and it is clear that the volume fraction distribution, evaluated from the inverse technique, is in very good agreement with the original input particle volume fraction distribution. The result for the particle volume fraction distribution can be further improved by making the particle size range smaller (a close-up of the improved result is shown as a dashed line in Figure 5.4).

In Figure 5.5 a more complicated, bimodal, volume fraction distribution is considered for the polystyrene particles. This distribution has a particle radius range of 20 to 45 μm with peaks at approximately 25 and 38 μm. The attenuation as a function of frequency for this volume fraction distribution is shown in Figure 5.6. The maximum frequency used in the inverse calculation is indicated in the figure by a square. It is seen that the frequency range includes the first two resonance peaks of the attenuation curve.

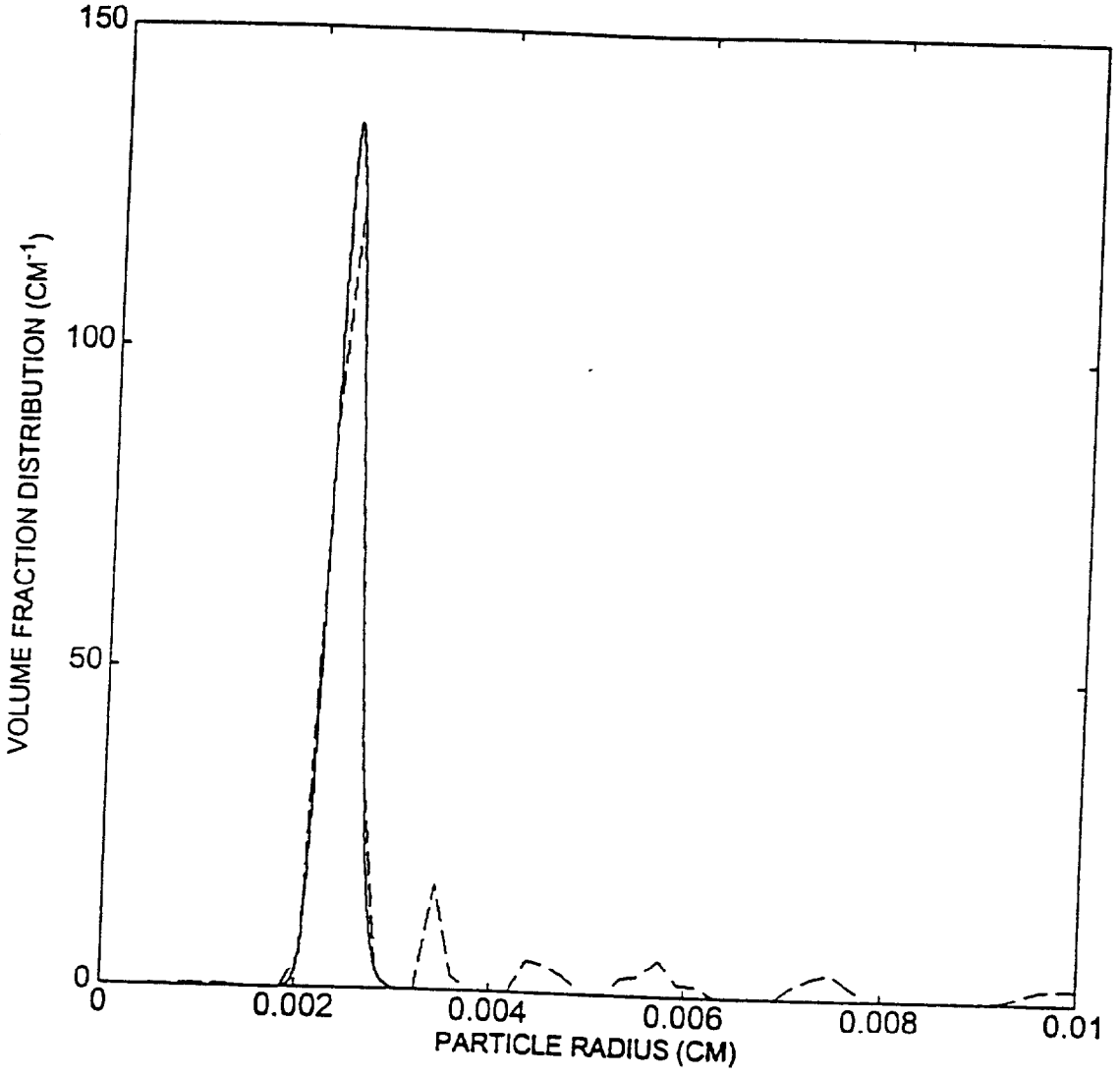

Figure 5.3: Inverse problem solution for polystyrene particles in water. The solid curve is the volume fraction distribution used to generate the attenuation curve shown in Figure 5.7a (with f_{max} indicated by a square); and the dashed curve is the solution to the inverse problem for particle radius range of 1 to 100 μm and using 50 'bins' of particle sizes.

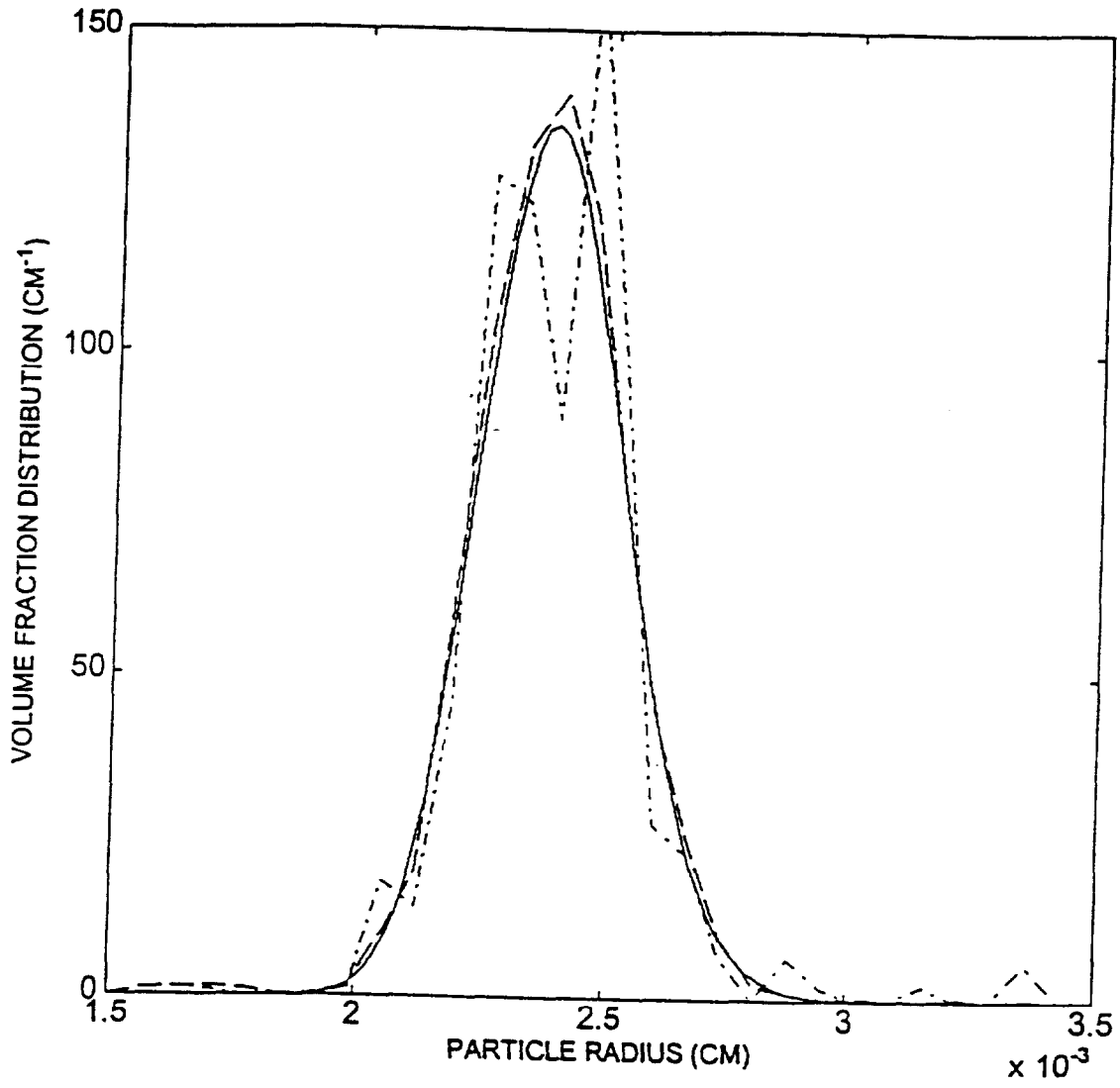

Figure 5.4: Solution of the inverse problem when a random noise of 5 % standard deviation is introduced in the attenuation (input) data. The solid line is the exact result; the dashed curve is the result when no noise is introduced; the dash-dotted curve is the result after the introduction of the noise. These calculations are for polystyrene in water.

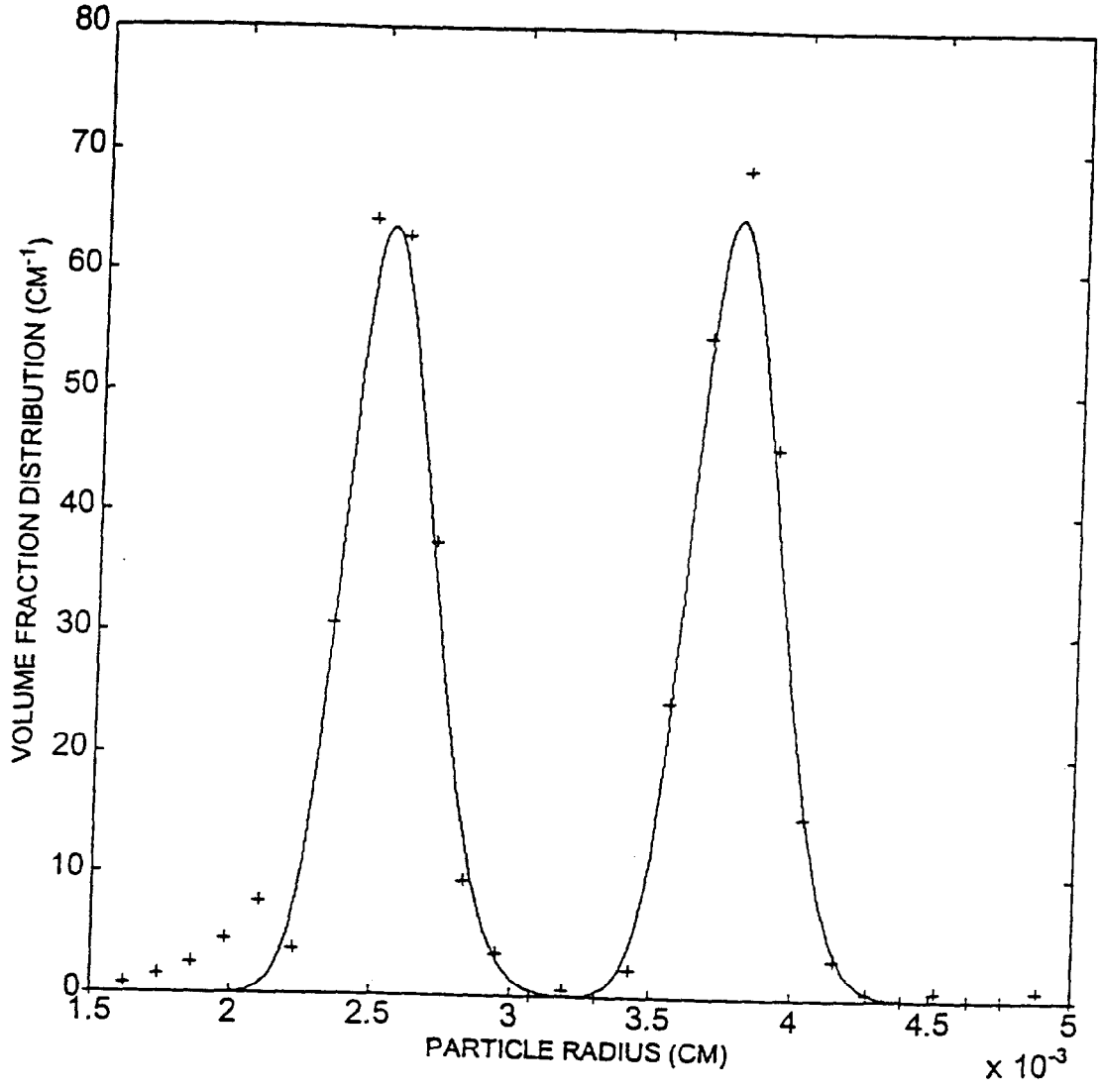

Figure 5.5: Solution of the inverse problem for a bimodal distribution of polystyrene particles, using 30 particle size bins. The solid curve is the exact result, and the markers represent the inverse problem solution when using a value of f_{max} indicated by a square in Figure 5.6.

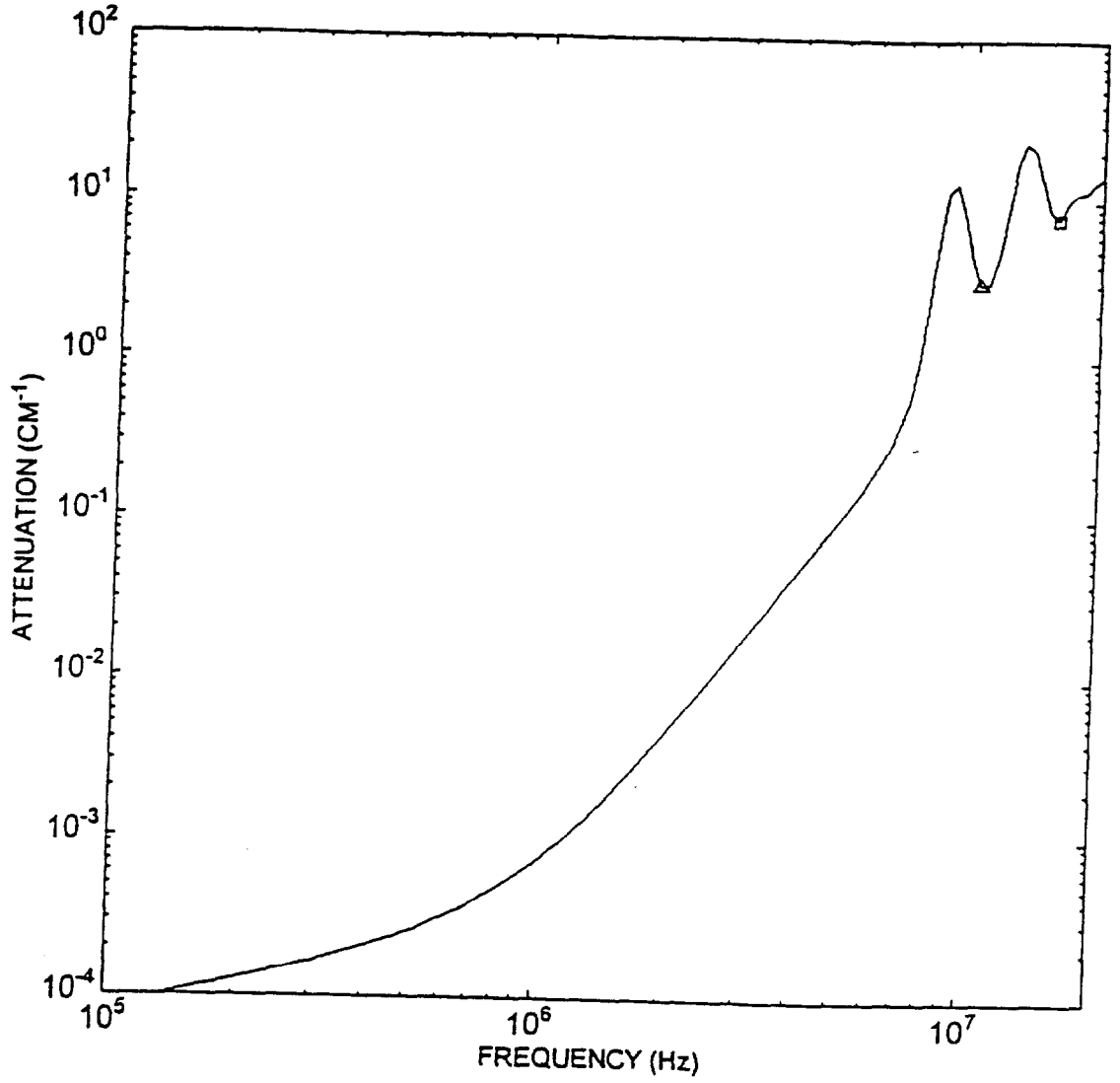

Figure 5.6: Attenuation versus frequency curve for polystyrene particle volume fraction distribution shown in Figure 5.5.

From the results shown in Figure 5.5 we can see, once again, that the inverse procedure recovers this distribution quite well.

As has been discussed previously, one of the difficulties in solving inverse problems is that they tend to be ill-posed. That is, small errors in the input (attenuation) data can lead to large changes in the solution (volume fraction distribution). Of course, there is always a certain amount of error present in experimentally obtained attenuation data. The inverse problem results presented so far were obtained with no noise added to the input attenuation data. To imitate the practical situation, a random noise of 5 % standard deviation was added to the input data. It turns out this error is approximately of the same order of magnitude as the error in the experimentally obtained attenuation data for polystyrene shown in Figure 4.2. The resulting volume fraction distribution is shown in Figure 5.4 (dash-dot line). The calculations were repeated with a noise of 10 % standard deviation (not shown), and the computed volume fraction distribution was considerably different form the input distribution, but the main features of the distribution were still preserved by the inverse computations.

The results which have so far been presented would suggest that the inverse technique can be employed with reasonable success. There are, however, limitations. The inverse problem technique yielded erroneous volume fraction distributions for smaller particles when the above mentioned frequency range (0.1 MHz to 17 MHz) was used in the computations. In order for the size of the particles to be determined there must be at least one transition in the attenuation versus frequency curve, namely the transition from the thermal attenuation dominated regime to the scattering dominated

regime which occurs when the dimensionless wavenumber becomes approximately $O(1)$. If the particles are very small this transition may not occur over a fixed frequency range. However, it will be shown that the results are quite sensitive to the frequency range which is chosen for the calculations, even when the transition is included in the frequency range.

Figures 5.7a & b illustrate the effect of varying the maximum frequency, f_{max}, on the computed volume fraction distribution. As seen in Figure 5.7a the resonance in the shape oscillations of the polystyrene particles leads to a change in the slope of the curve just before the first resonance. This transition occurs just before the point marked with a circle in Figure 5.7a. There appears to be a marked improvement in the results shown in Figure 5.7b when f_{max} is chosen corresponding to a point marked by a cross in Figure 5.7a over those obtained with the point corresponding to a circle, which does not include the second change in slope. The point marked with a cross corresponds to a frequency greater than the frequency at which the second change in slope occurs for larger particles but less than that for smaller particles. This gives rise to a solution of the inverse problem (cf. Figure 5.7b) which is reasonably accurate for larger particles but not as accurate for smaller particles. Also shown in Figure 5.7b are the results when f_{max} is chosen to coincide with the end of the first resonance peak in the attenuation versus frequency plot. This is the point marked with a square in Figure 5.7a. The resulting volume fraction distribution shows that when the first resonance peak is included in the attenuation data, the resulting volume fraction distribution predicted from the inverse problem solution is quite accurate.

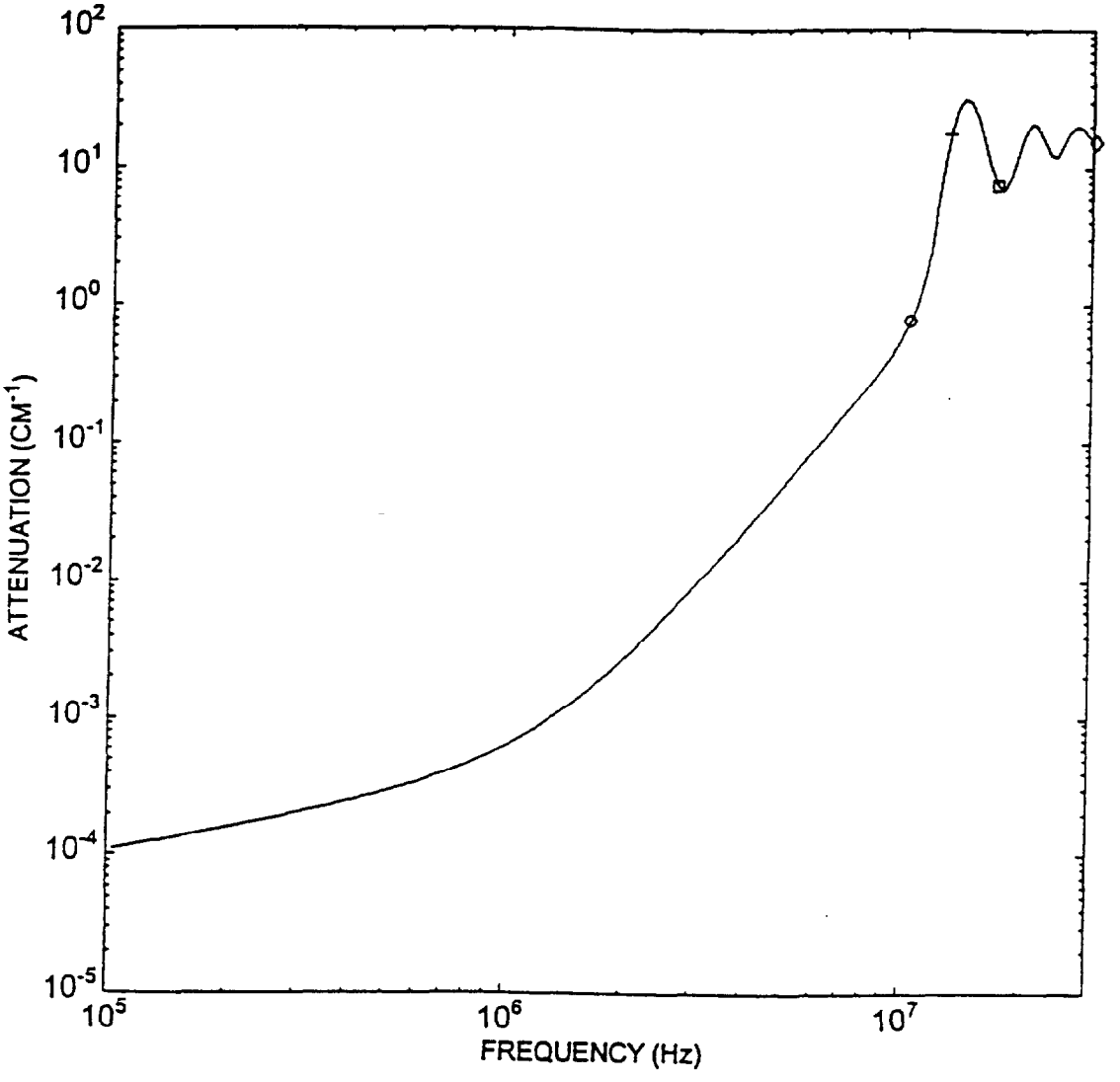

Figure5.7a: Input attenuation data for four different upper bounds on frequency to determine the influence of the frequency range over which the attenuation is specified on the solution of the inverse problem. This attenuation curve is for polystyrene in water. The solid curve is the exact result; □, cutting off the frequency range after the first attenuation peak; +, cutting off the frequency range just after the second change in slope in the attenuation curve; O, cutting off the frequency range just before the second change in slope in the attenuation curve; and ◊, cutting off the frequency range just after the third attenuation peak.

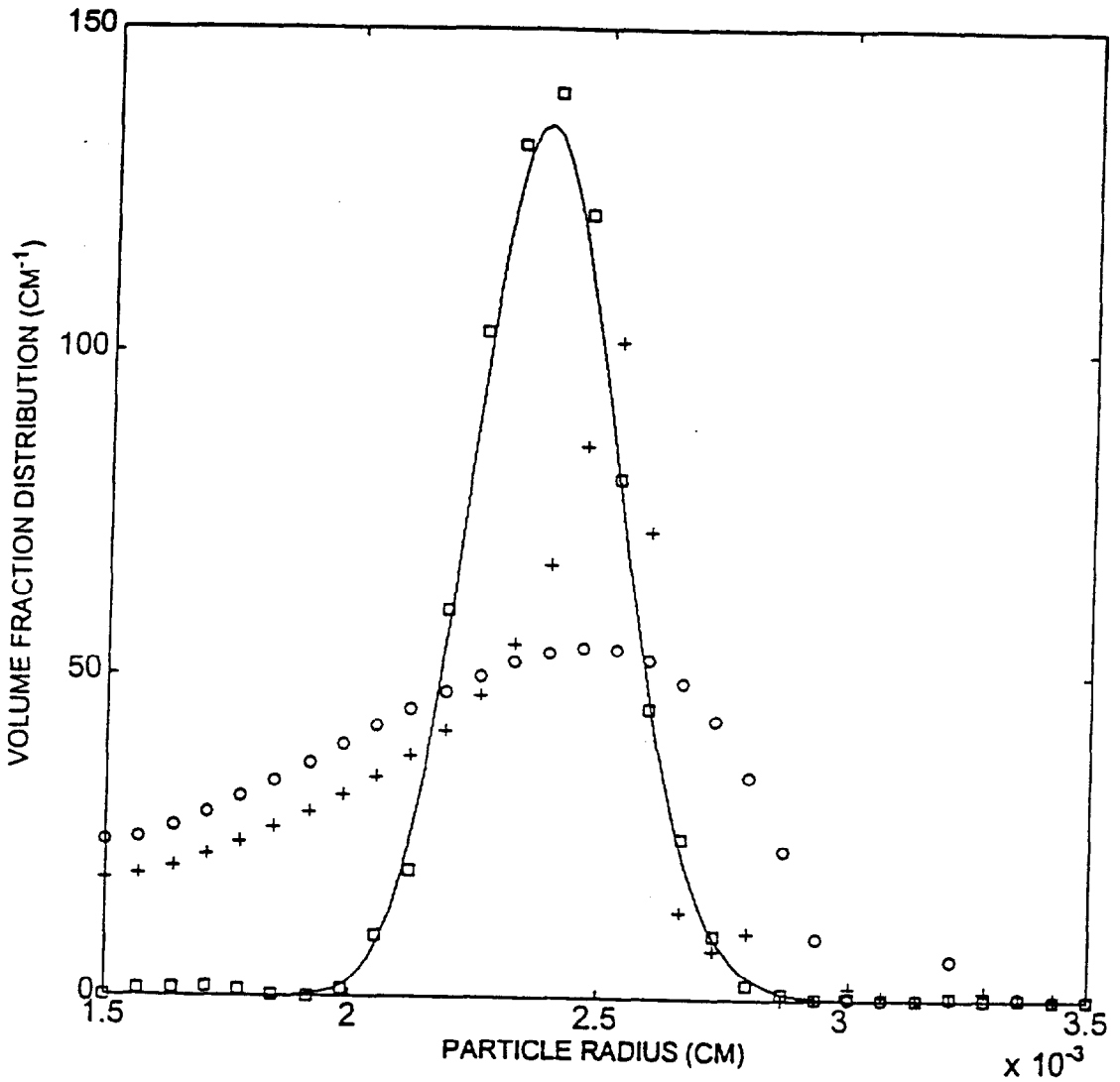

Figure 5.7b: Results of the inverse problem solution for four different frequency ranges using the same marker types as in Figure 5.7a.

It should, however, be noted that one cannot alleviate all the difficulties mentioned above by merely choosing a wide enough frequency range of interrogation. Figure 5.8 shows results of the inverse problem calculations for three different values of f_{max}. The dashed curve corresponds to terminating the frequency range at the end of the first resonance peak, as in Figure 5.7a. The dash-dot curve corresponds to terminating the frequency range at the end of three resonance peaks; and the dotted curve corresponds to terminating the frequency range at 10^9 Hz, a frequency which is approximately fifty times greater than the first resonance frequency. Figure 5.8 shows that the results of the inverse calculation actually deteriorate from those calculated after the first resonance peak if a much larger range of frequency is employed. The deterioration of results is due to the different modes of oscillation which may undergo resonance. As is shown in Figure 4.4, a monodisperse suspension will exhibit several resonance frequencies corresponding to various shape oscillation P_n (n =2, 3, ...) modes. Therefore, a second peak in the attenuation versus frequency curve for polystyrene particles could, for example, correspond either to a P_3 mode for a larger particle, or it could correspond to a P_2 mode for smaller particle. The inverse calculations performed in this work used only the first six modes ($n \leq 5$), but in practice the acoustic response may be further complicated by the higher modes of oscillation for frequencies of the order of 10^9 Hz considered here.

Since including an extremely wide frequency range with several resonance peaks seems to adversely affect the inverse calculations, one may consider terminating the attenuation data just beyond the first resonance peak. This strategy may not be successful

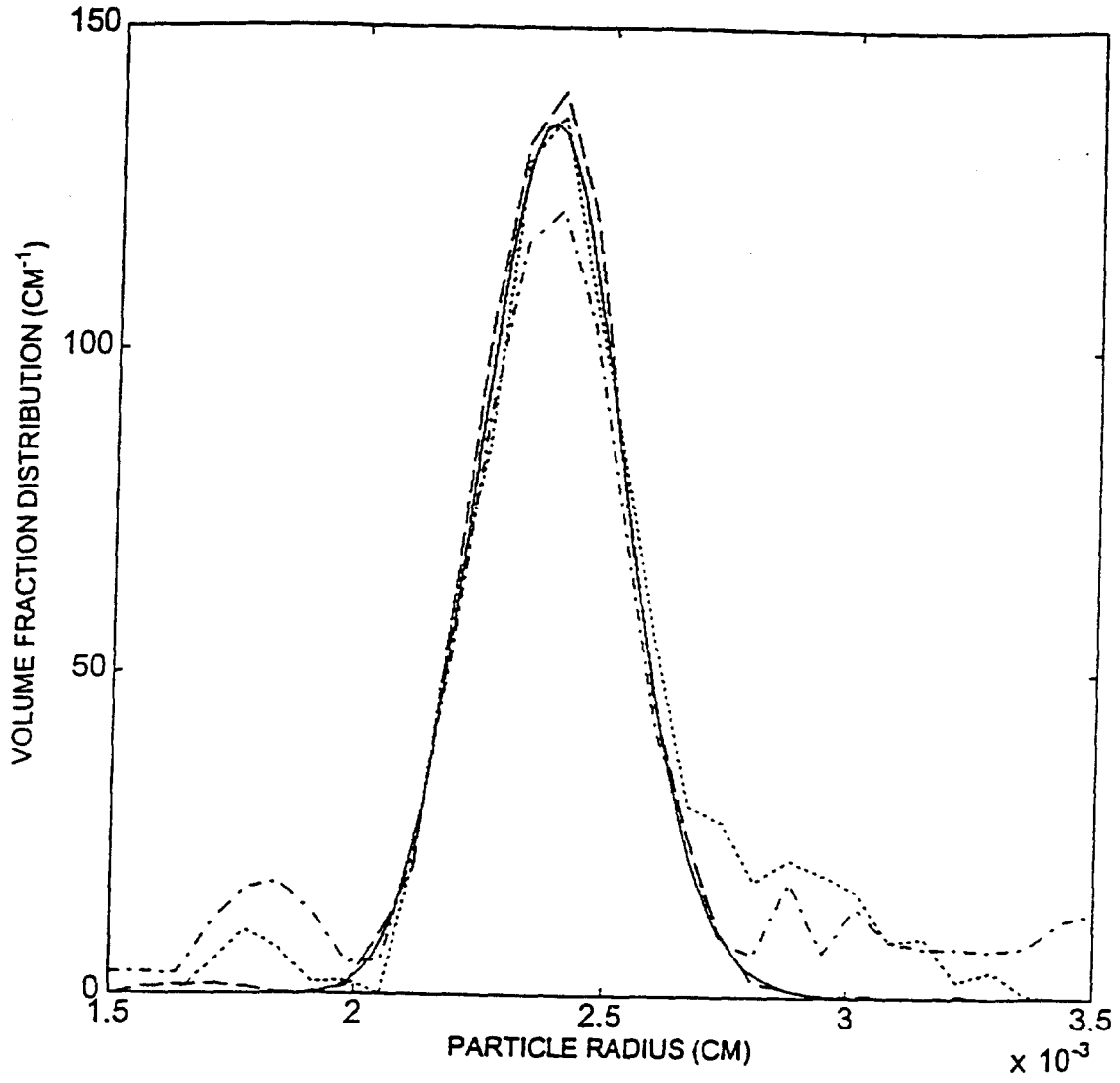

Figure 5.8: Using too large of a frequency range over which the attenuation data are available for polystyrene particles in water can deteriorate the results. The solid curve is the exact result; the dashed curve is the inverse problem result when using the data of Figure 5.7a below the point marked by a '□' the dash-dotted curve represents the results when this endpoint is shifted to the point marked by '◊'; and the dotted curve is the result when this endpoint is shifted to 1000 MHz.

if the volume fraction distribution is truly bimodal as was seen earlier in Figure 5.5. If the second resonance peak is omitted from the attenuation data by considering a frequency range with a maximum that is less than the frequency marked with a square in Figure 5.6, for example let the maximum be the frequency marked with the triangle; then the inverse calculation yields rather poor results as shown in Figure 5.9. It is interesting to note that the inverse technique computes rather accurately the volume fraction distribution of the larger particles, whose resonance behavior was included in the data; but it fails to accurately predict the volume fraction distribution for the smaller particles, whose resonance behavior is not included in the attenuation data.

Figures 5.10a & b show the inverse technique results for a very broad unimodal distribution for polystyrene particles. The resonance peaks of the different particles overlap in this case, resulting in the absence of peaks in the attenuation versus frequency curve (cf. Figure 5.10a). Figure 5.10b shows the results of the inverse calculation for three different cut-off frequencies. The largest frequency, marked by a square in Figure 5.10a, is larger than the second transition frequency of small as well as large particles, and this appears to produce excellent results.

We note that in the cases shown so far where the inverse calculations yielded poor results the failure is particularly severe for smaller particles. This phenomenon may be explained when one considers that the total error, E, will be dominated by the errors at large frequencies, since the attenuation there is quite large. When $k_C a_{\min} < 1$ in the frequency domain that is considered, the small particles' volume fraction appears in Figures 5.7b and 5.9 to be underestimated, while the large particles' volume fraction is

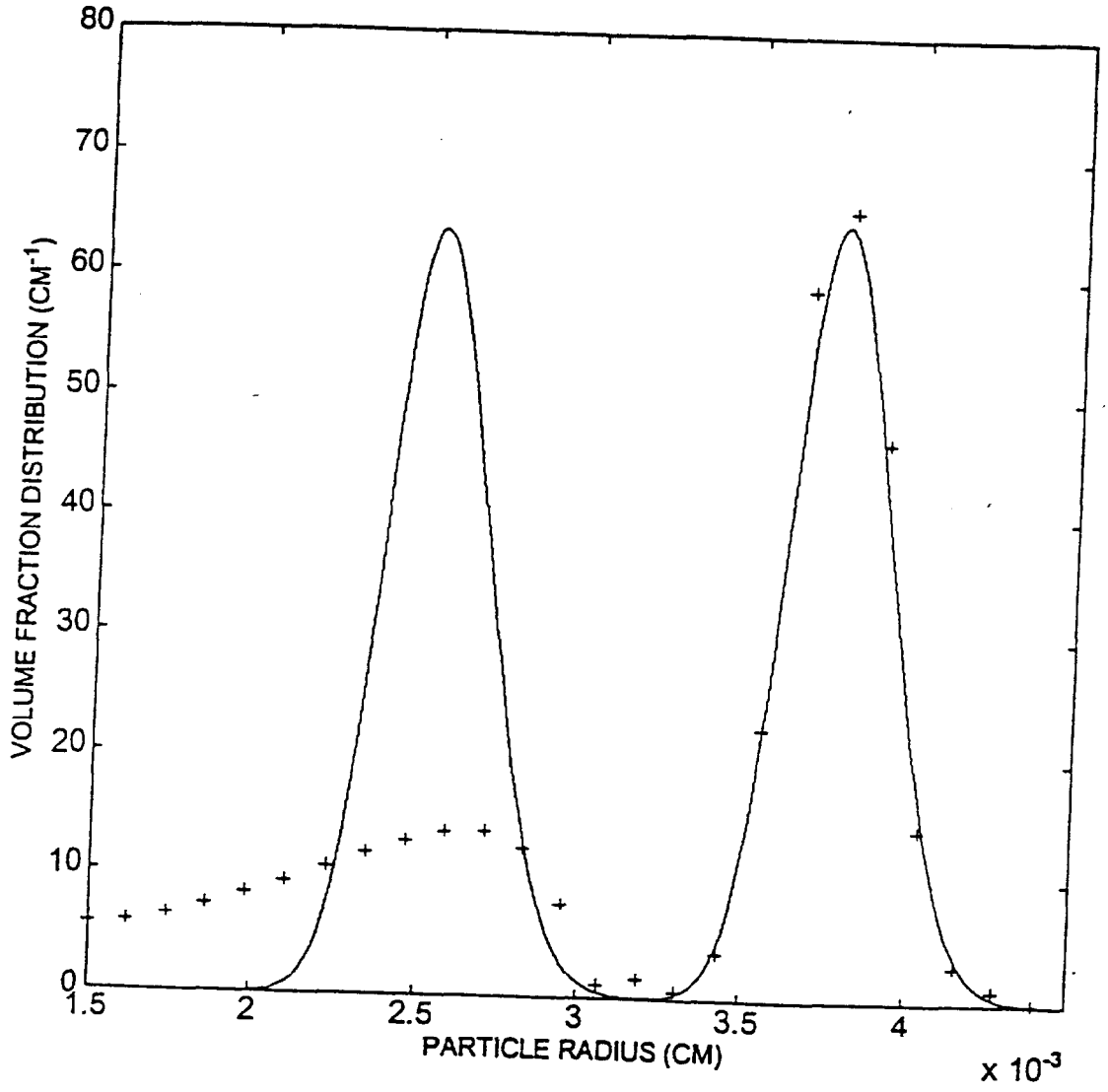

Figure 5.9: Inverse problem solution for a bimodal distribution of polystyrene particles (same distribution as in Figure 5.5) when cutting off the frequency range over which the attenuation was given between the first and second attenuation peaks.

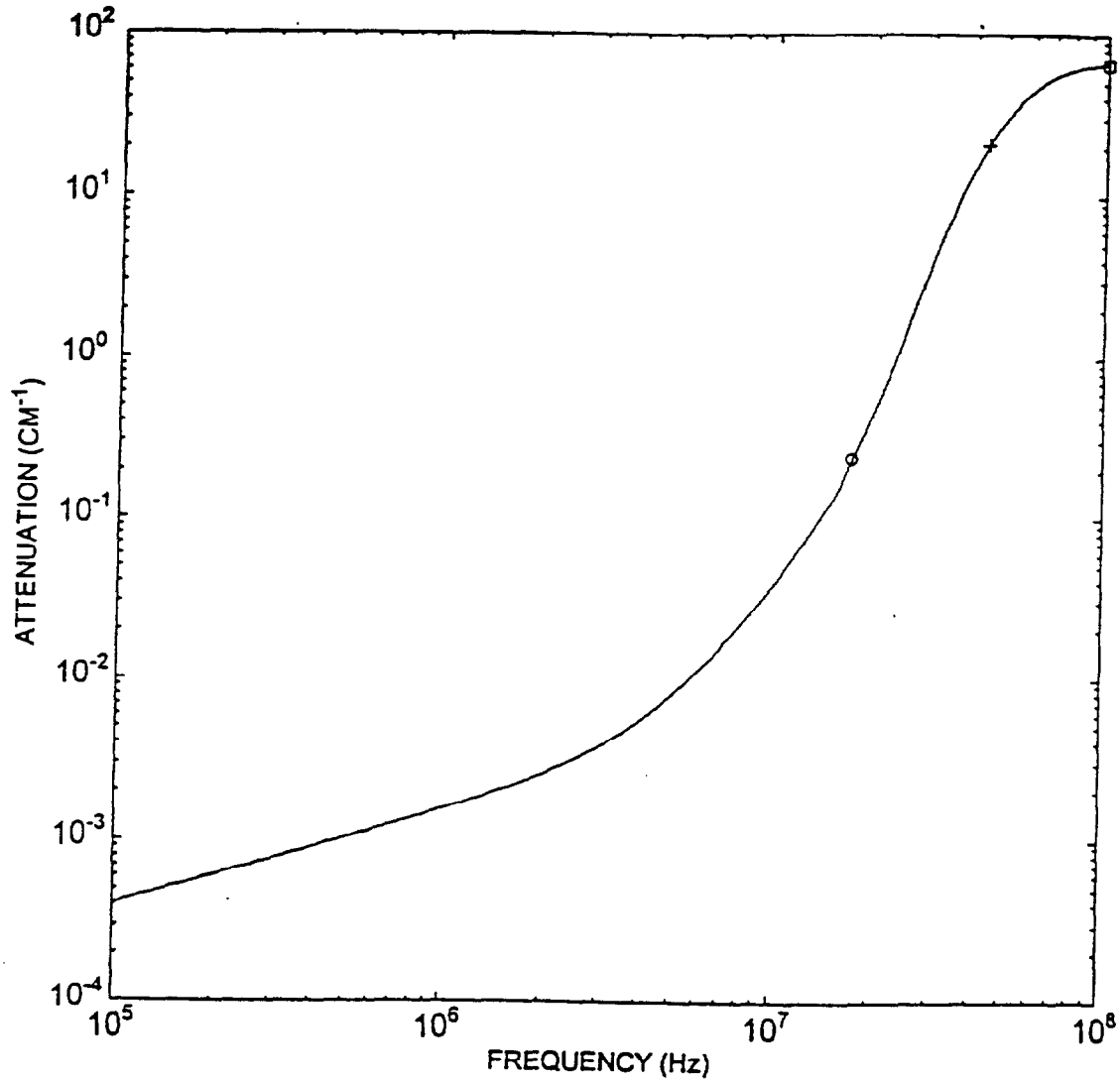

Figure 5.10a: Attenuation versus frequency curve for the same inverse calculation for polystyrene particles in water whose results are shown in Figures 5.7a & b, but with a broader size distribution.

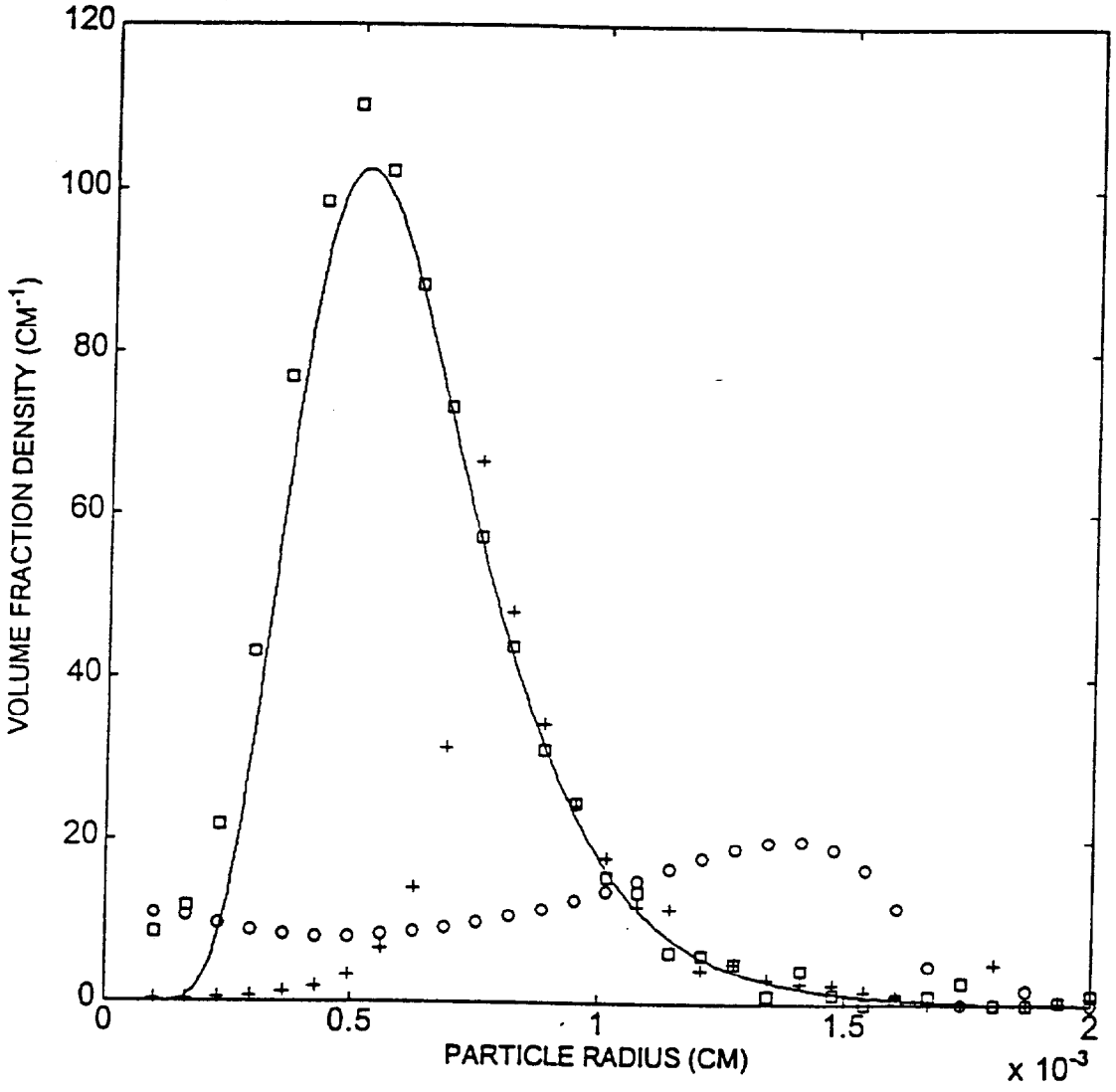

Figure5.10b: Resulting volume fraction distribution for the broader distribution attenuation data shown in Figure 5.10a.

slightly overestimated. This problem was addressed in some calculations by dividing both the attenuation and $\hat{\alpha}$ by f^2. However, only small improvements were realized by modifying the attenuation data in this manner. It should be noted that the inverse calculation results presented in Figure 5.9 were obtained in this manner.

Figures 5.11a, b, & c provide some insight into why the choice of f_{max} can greatly affect the results of the inverse calculation. These figures show three-dimensional plots of the kernel, K (for the same values of f_{max} considered in Figures 5.7a & b) plotted against particle radius, a_i and a_j. We see that when f_{max} = 10.4 MHz, corresponding to the circle in Figure 5.7a, the kernel has a maximum for $a_i = a_j = a_{max}$. The kernel for smaller particles is rather small in comparison; and as a consequence, the inverse technique could determine the larger size particle volume fraction correctly but failed for the smaller particles. In contrast, the kernel for f_{max} = 17.1 MHz, corresponding to the end of the first peak in Figure 5.7a, shows significant variations for a wide range of values of a_i and a_j (cf. Figure 5.11b). This behavior of the kernel apparently leads to a much more accurate inverse solution. Finally, the kernel for f_{max} = 30.4 MHz, corresponding to the end of the third resonance peak in Figure 5.7a, shows a less pronounced structure (cf. Figure 5.11c) which explains the fact that the inverse results actually deteriorated when using such a wide frequency range.

Inverse problem calculations were also performed to determine the kernel, volume fraction distribution, and attenuation in the bubbly liquids examined by Duraiswami (1993). The inverse procedure worked quite well for bubbly liquids as is shown in Figures 5.12a, b, & c. Figure 5.12a shows the input and computed bubble volume

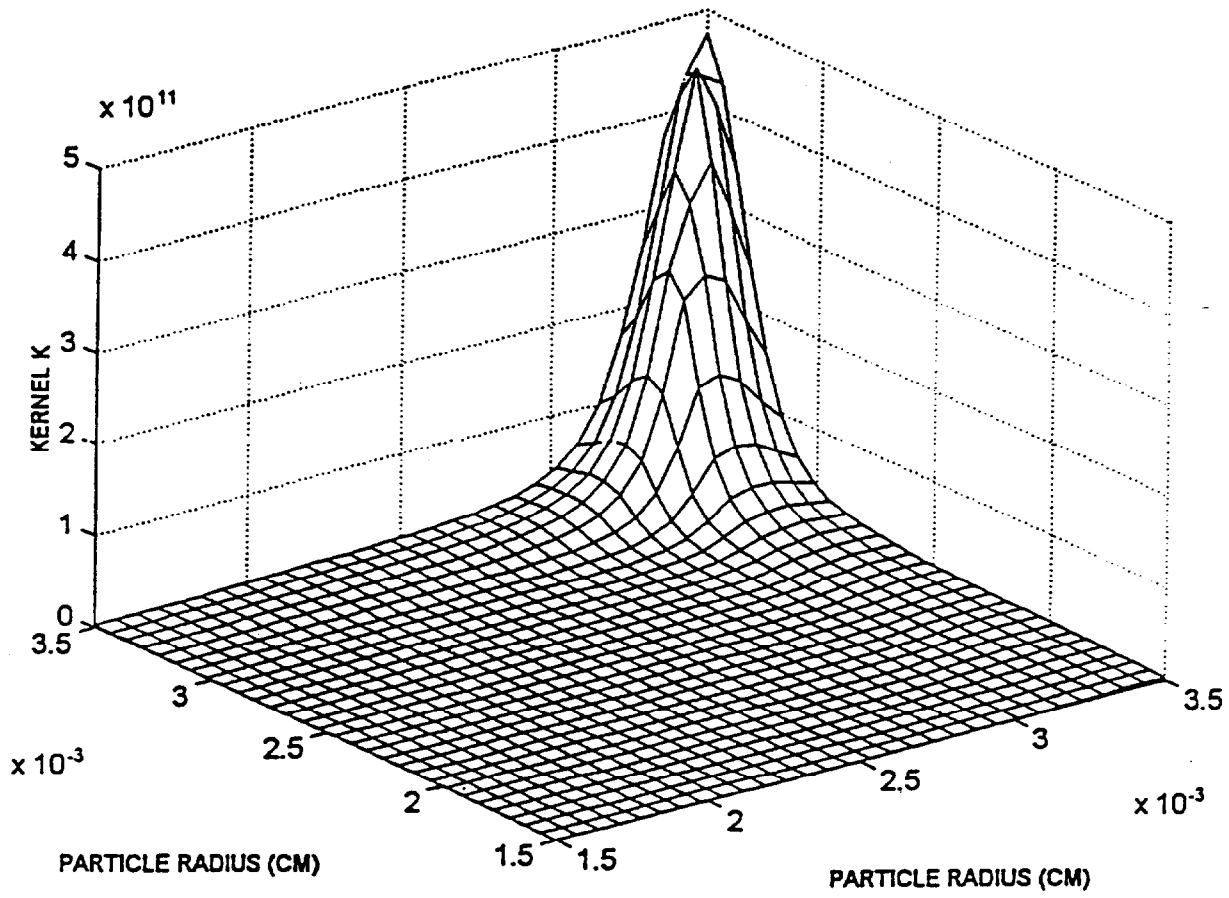

Figure 5.11a: The kernel, $K(a_i, a_j)$ for polystyrene particles in water when using for f_{max} the value of frequency indicated by a 'O' in Figure 5.7a.

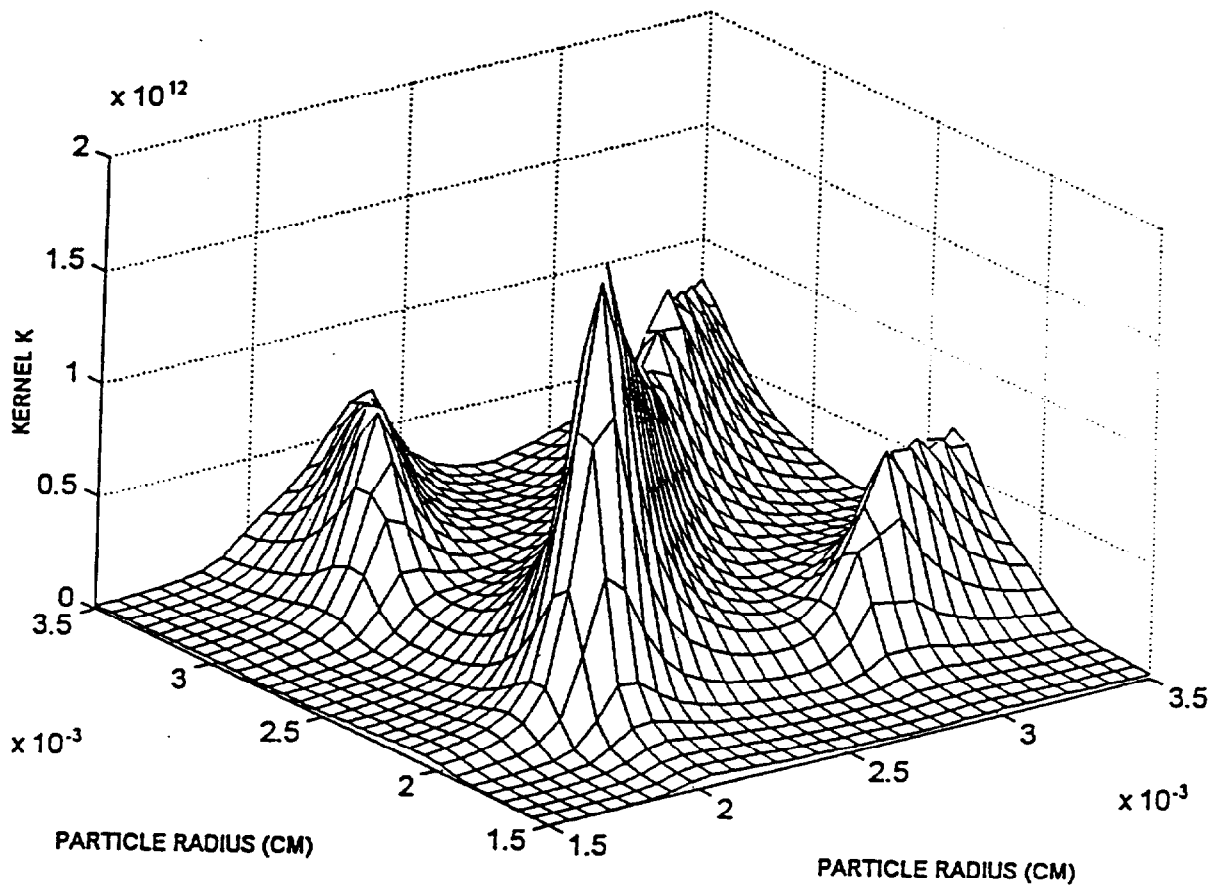

Figure 5.11b: The kernel, $K(a_i, a_j)$, for polystyrene particles in water when using for f_{max} the value of frequency indicated by a '+' in Figure 5.7a.

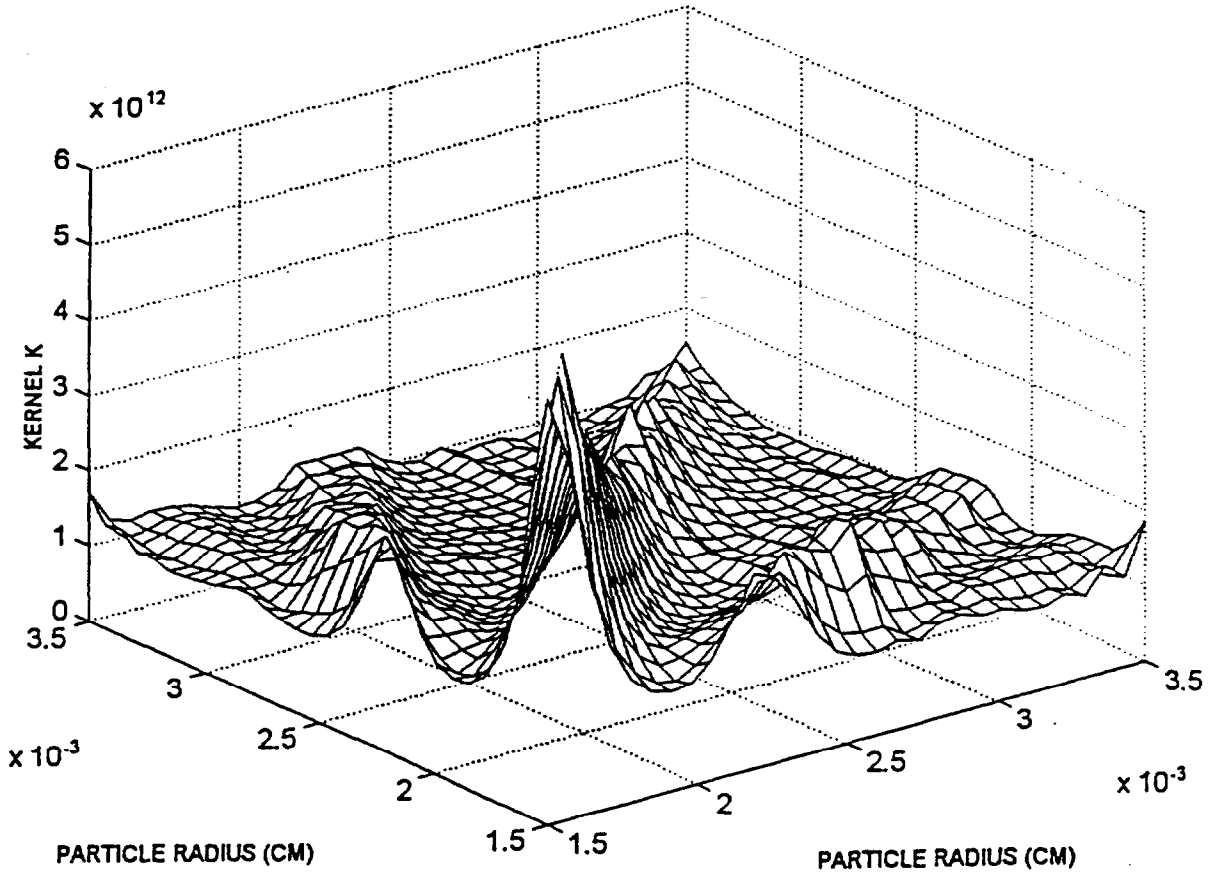

Figure 5.11c: The kernel, $K(a_i, a_j)$, for polystyrene particles in water when using for f_{max} the value of frequency indicated by a '□' in Figure 5.7a.

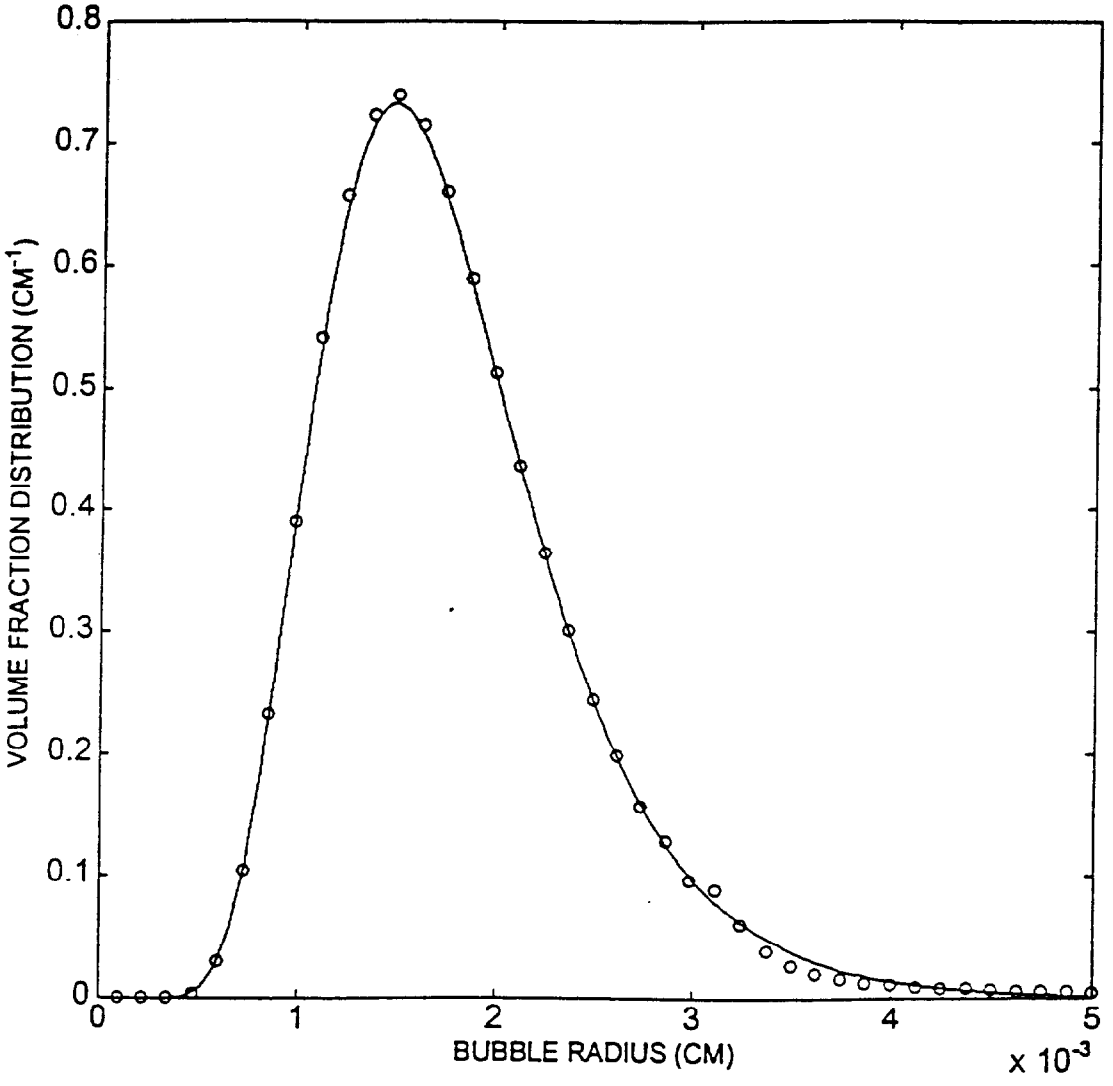

Figure5.12a: Results of the inverse problem solution for air bubbles in water. Bubble volume fraction distribution for a total gas phase volume fraction equal to 0.004.

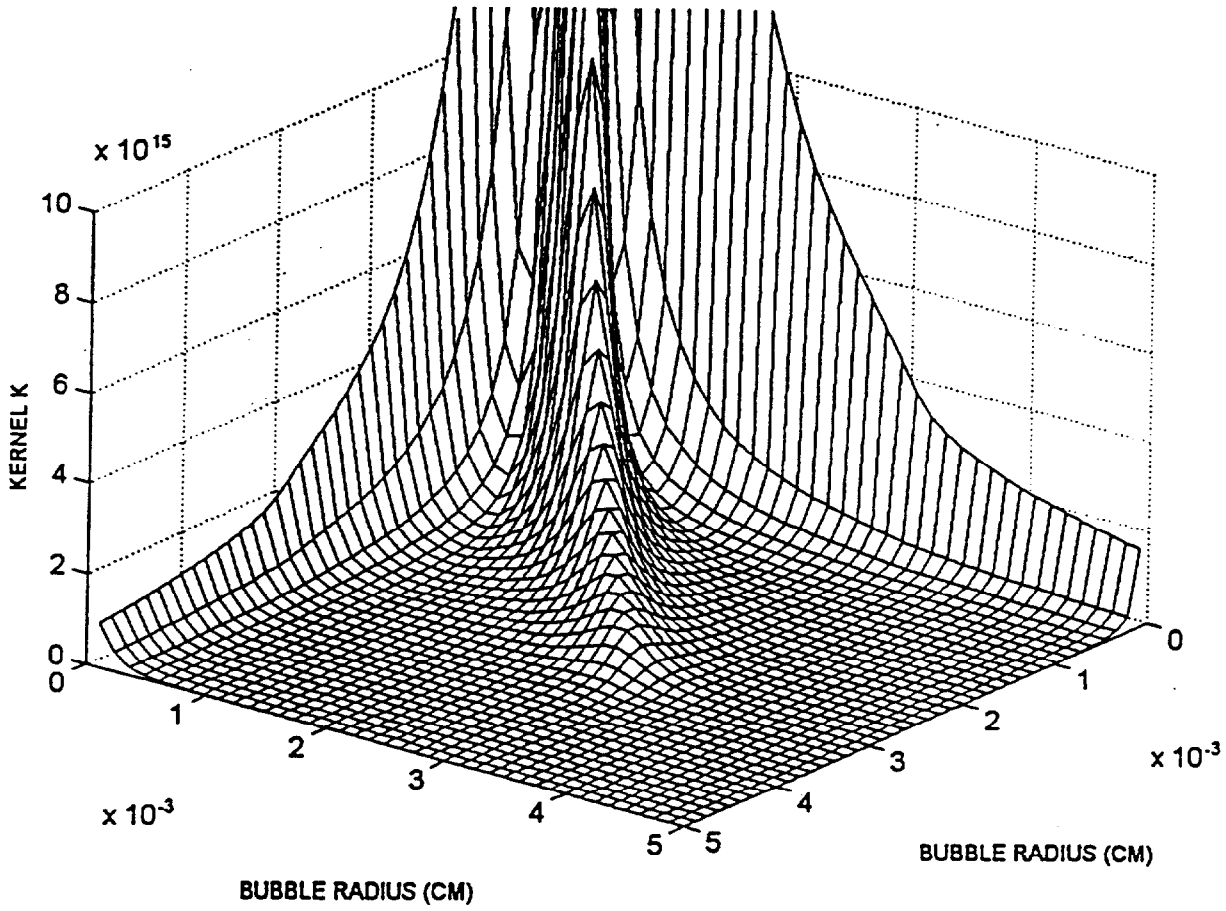

Figure 5.12b: The kernel, $K(a_i, a_j)$, for air bubbles in water at a total gas phase volume fraction of 0.004.

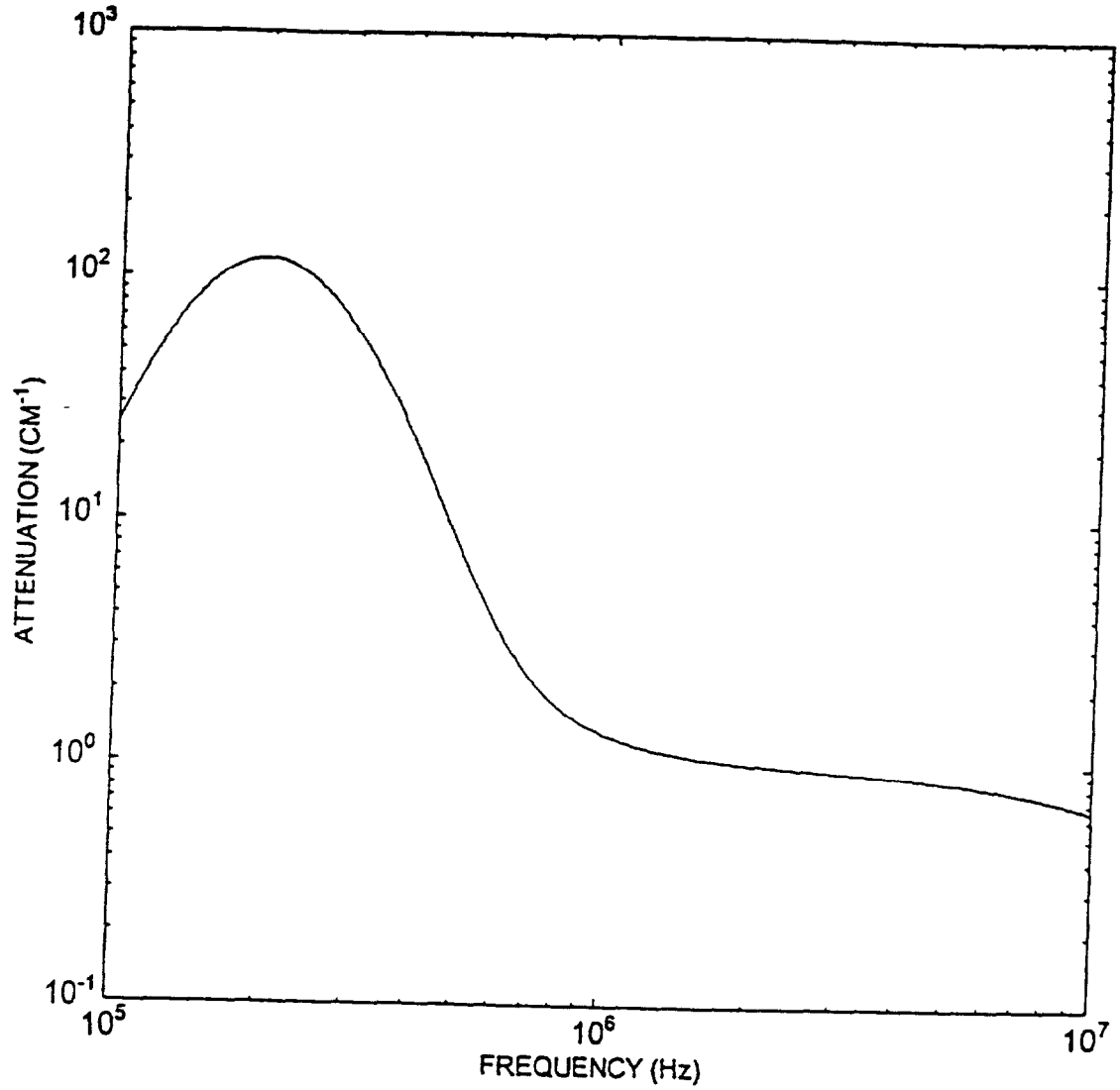

Figure 5.12c: The attenuation spectrum for air bubbles in water at a total gas phase volume fraction of 0.004.

fraction distributions to be in excellent agreement. The kernel, as shown in Figure 5.12b, has smooth variations over a wide range of bubble radii. The resulting attenuation as a function of frequency is shown in Figure 5.12c. The main reason why the inverse technique appears to be somewhat more successful for bubbly liquids is that there is only one resonance frequency for bubbles of each size. Therefore, so long as the frequency range is wide enough to cover the resonance frequency of all the bubbles, it is possible to accurately determine the volume fraction distribution.

If one recalls the notable difference between the attenuation data for polystyrene and that for soda-lime glass particles, it was the absence of the multiple resonance peaks for the soda-lime glass particles (cf. Figure 4.5). Along with this fact, it was found that the inverse calculation results for the soda-lime glass particles were generally poor. Figure 5.13a shows an inverse problem result for small soda-lime glass particles which is still reasonable; however, that shown for larger particles in Figure 5.13b is quite poor.

The reason for this result lies in the shape of the kernel, which is shown for the latter case in Figure 5.13c. When this kernel is compared with those for polystyrene particles (cf. Figure 5.11b) and for bubbles (cf. Figure 5.12b), it can be seen that the kernel for the soda-lime glass particles is relatively flat. This behavior is indicative of an inverse problem which is rather hard to solve.

Based on the above discussion, it can be said that the success of the Tikhonov regularization in solving the inverse problem is somewhat limited. Although reasons are given as to why this method worked well for bubbly liquids and not as well for slurries, other techniques were examined to investigate whether they might be more generally

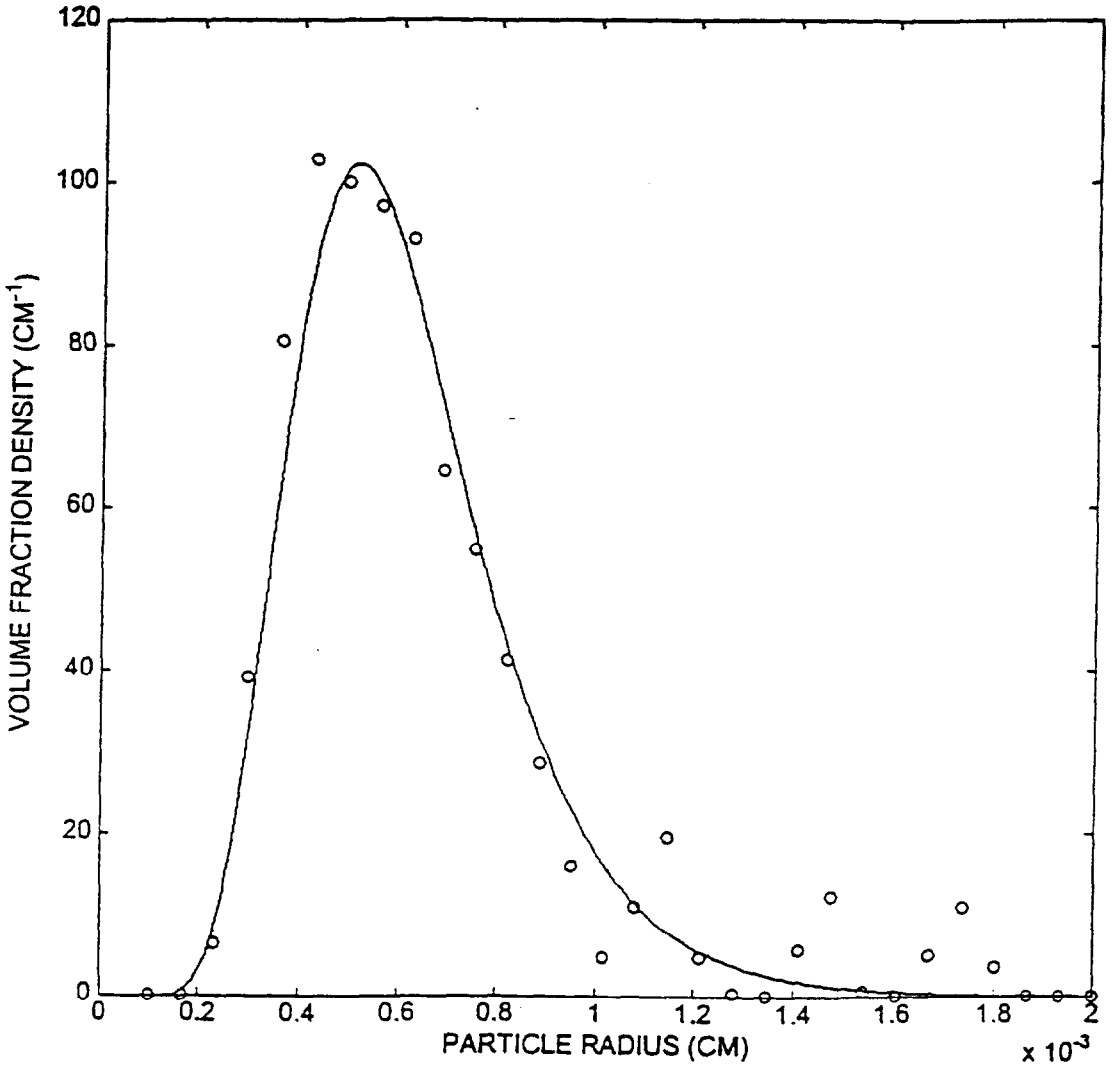

Figure 5.13a: An inverse problem result for small glass particles.

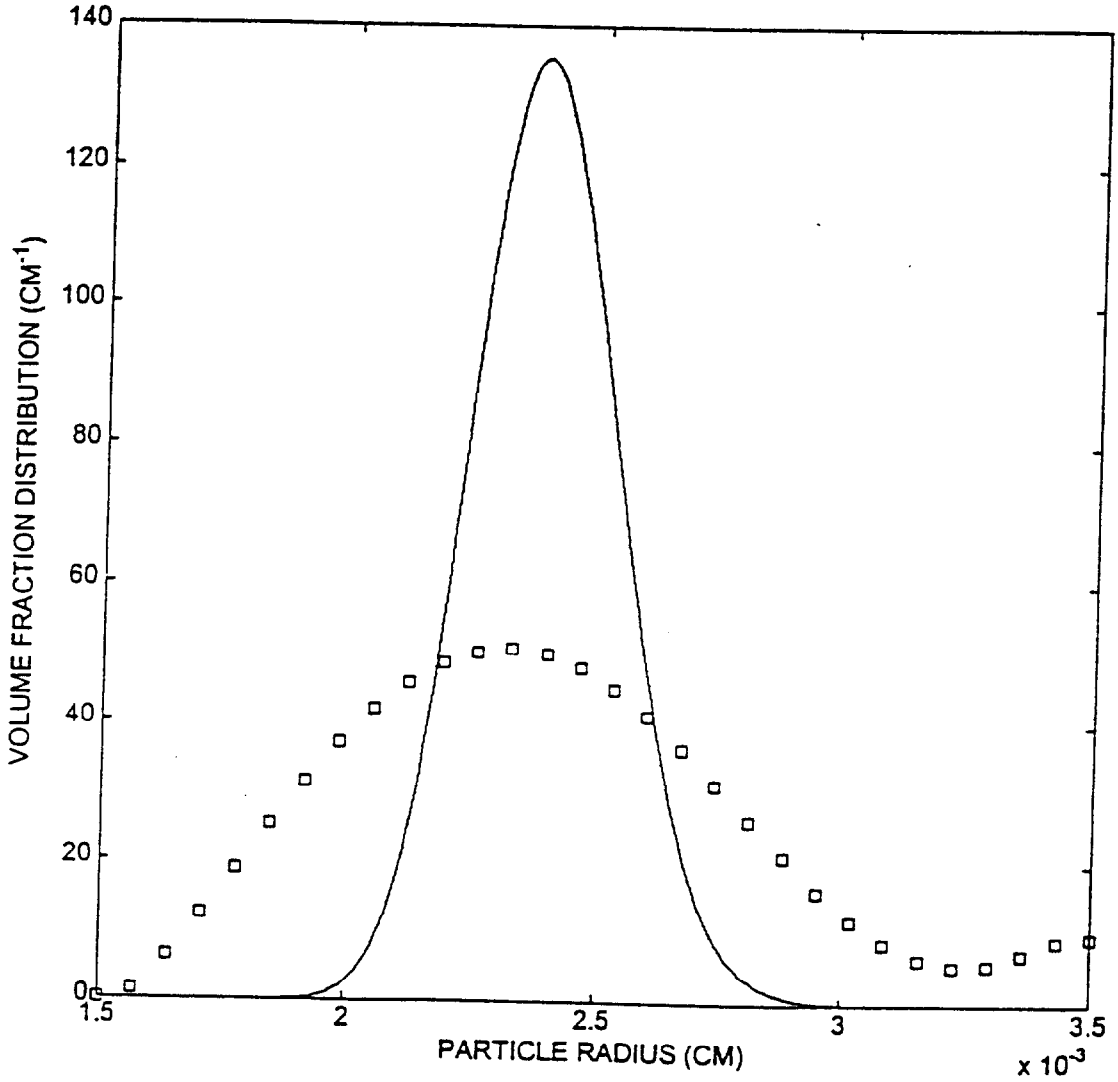

Figure 5.13b: An inverse problem result for larger glass particles.

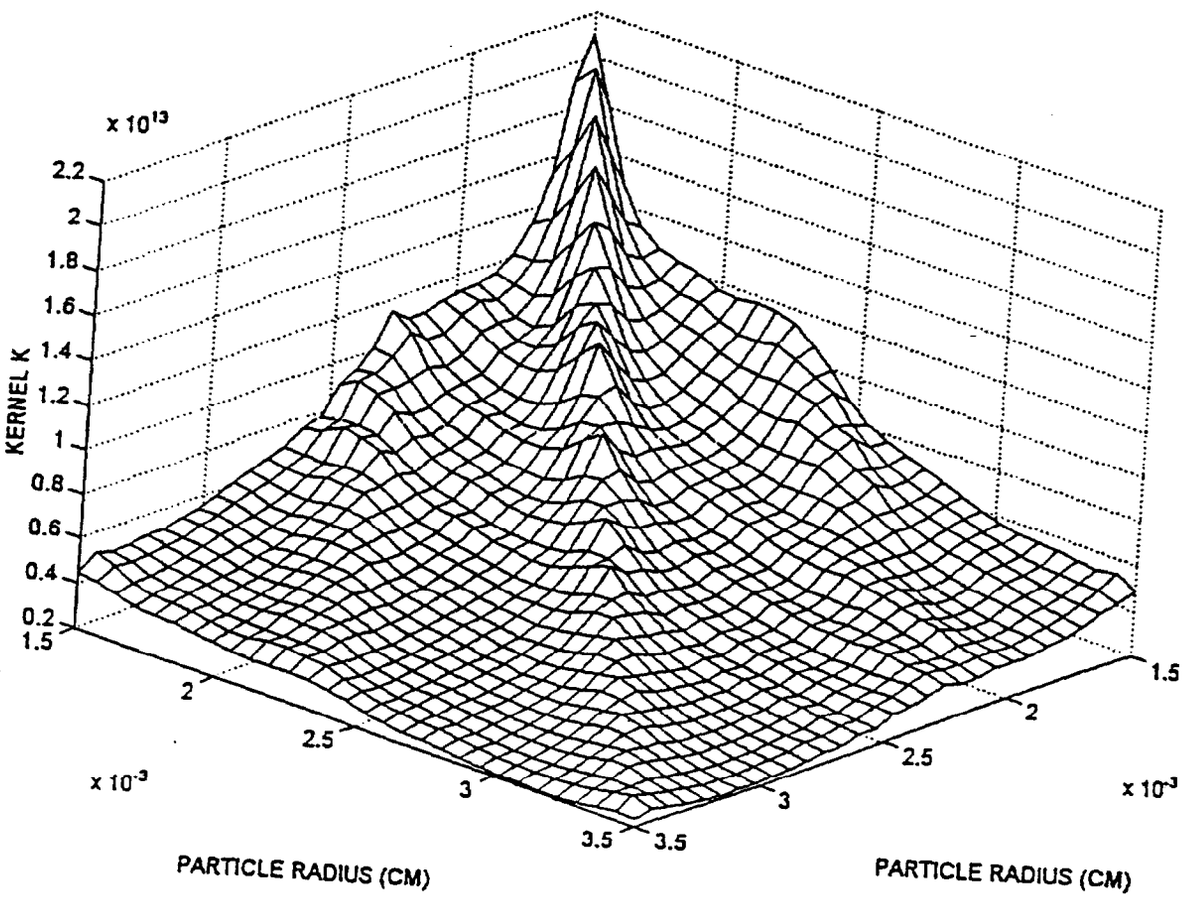

Figure 5.13c: The kernel, $K(a_i, a_j)$, for the larger glass particles whose results are shown in Figure 5.13b.

successful. With that in mind, an alternative method based on linear programming was attempted.

The constraint $\phi(a) \geq 0$ was satisfied only *a posteriori* in the Tikhonov scheme. To ensure that the error was minimized while satisfying this constraint, the original inverse problem is reformulated as an optimization problem. The simplest scheme is that to minimize the error

$$\int_{f\min}^{f\max} \left| \int_{a\min}^{a\max} \hat{\alpha}(f,a)\phi(a)da - \alpha_{\text{tot}}(f) \right| df \ , \qquad (5.8)$$

instead of the integral of the square of the quantity enclosed by the two vertical bars at each frequency. Constraints on the solution are used *a priori* in optimization via linear programming; here $\phi(a) \geq 0$ is used. Imposing an upper limit on the total volume fraction (maximum packing) can also be incorporated but is not essential. After discretizing the frequency range by M and $\phi(a)$ by N discrete values, one can write

$$\sum_{j=1}^{N} B_{ij}\phi(a_j) - \alpha_{\text{tot}}(f_i) = u_i - v_i \qquad u_i, v_i \geq 0 \qquad i = 1,2,\ldots,M \ . \qquad (5.9)$$

Here, $B_{i,j}$ is the discretized form of the integral operator in equation (5.8); and u_i and v_i are, as yet, unknown, non-negative variables. It can be shown (Delves 1985) that minimizing the absolute value of equation (5.9) is equivalent to minimizing

$$\sum_{i=1}^{M}(u_i + v_i) \qquad (5.10)$$

with equation (5.9) as a constraint together with the constraints $u_i, v_i \geq 0$ ($i = 1,\ldots,M$) and $\phi(a_i) \geq 0$ ($i = 1,\ldots,N$). It is essential here that at the optimum $u_i\, v_i = 0$ for each i, which makes the solutions of the two minimization problems, equations (5.8) and (5.9), identical.

Although the above linear programming scheme is a completely different method for solving the inverse problem, the results obtained from it were found to be very similar to those obtained from the Tikhonov method. It was shown earlier that the Tikhonov regularization fails when the frequency range over which the attenuation data are provided is made too small. In Figures 5.14a & b linear programming results are presented for the same problem solved by the Tikhonov method in Figures 5.7a & b. The Tikhonov method results are also presented in Figure 5.14b (open square markers) for comparison. From these figures it is clear that there is no improvement. In fact, there is actually a deterioration of results. Similarly, it was found that increasing the frequency range cut-off beyond the point marked with a square in Figure 5.14a actually made the results worse, as it had in the solution in Figure 5.7a. The other problem where the Tikhonov regularization failed was in the case of relatively large soda-lime glass particles (cf. Figures 5.13a & b). The linear programming technique also failed to yield good inverse results for this case

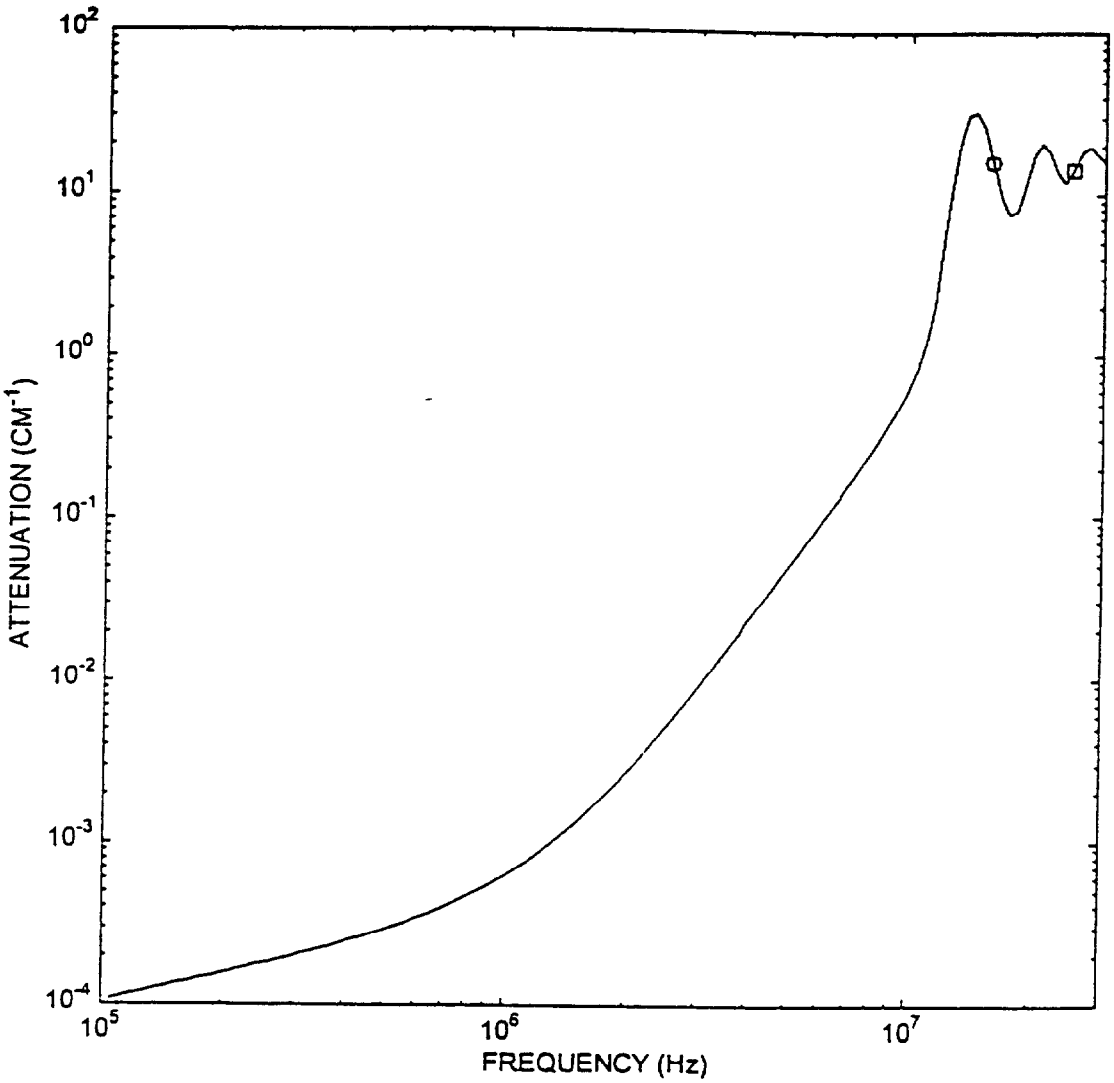

Figure 5.14a: Attenuation spectrum for polystyrene particles in water where the data are used in the linear programming results shown in Figure 5.14b.

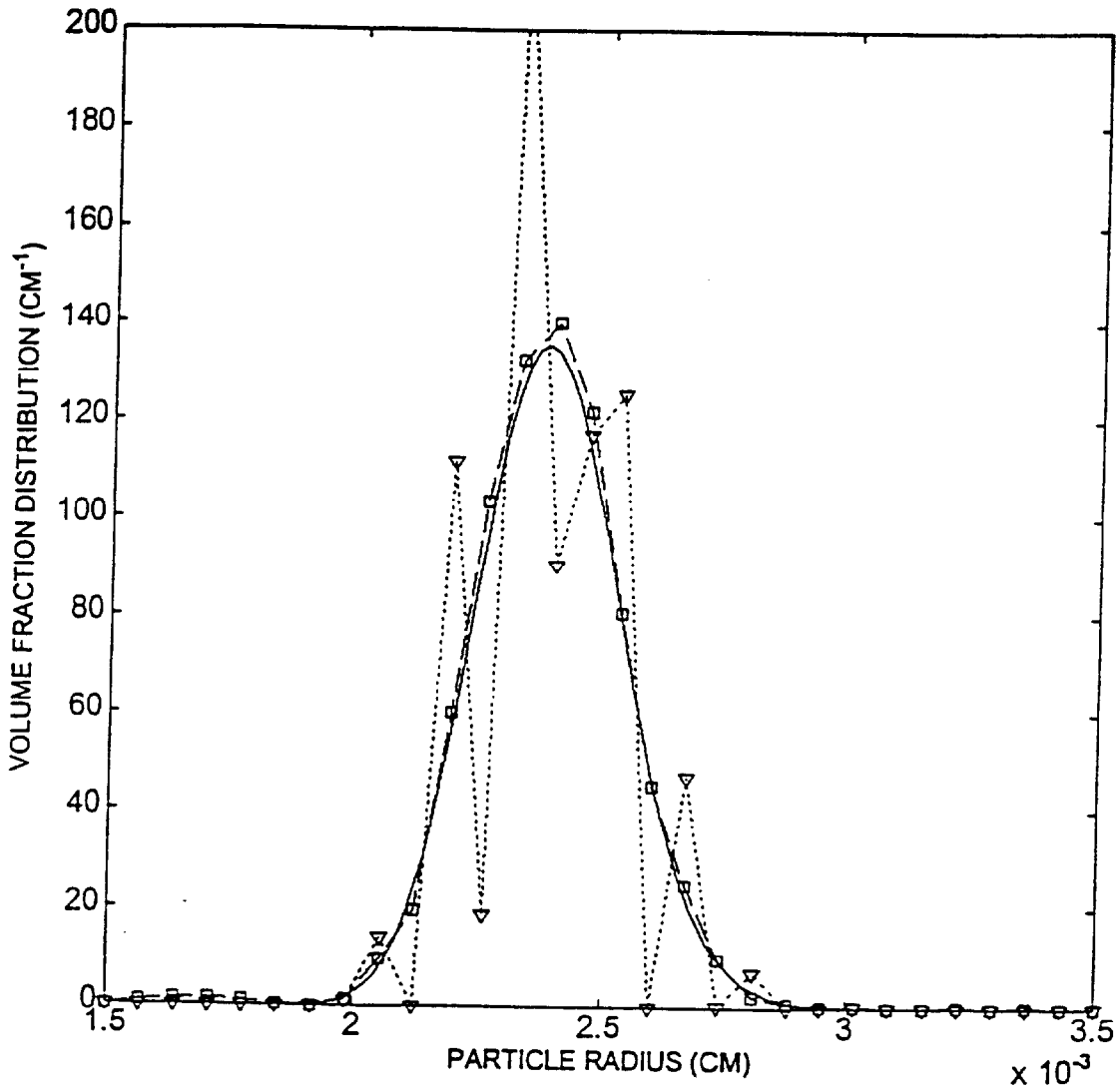

Figure 5.14b: Inverse problem results using the linear programming method. The linear programming results (..∇..) are compared with results of the Tikhonov method (--□--) and the exact solution (solid curve).

Chapter 6: Effective Medium Theory and Experiments for Concentrated Slurries

6.1 Effective Medium Theory:

As mentioned earlier, the measurement of the attenuation of acoustic waves through a suspension of solid or fluid particles can be used to infer the suspension properties. When the particle volume fraction in the suspension is very small the particle interactions may be neglected, and the attenuation as a function of the sound wave frequency can be determined by examining the interaction of a single particle with the incident wave as has been done by a number of investigators in the past and in Chapter 4. As mentioned earlier, Foldy (1945) examined the problem of scattering in dilute bubbly liquids. Epstein and Carhart (1953) and Allegra and Hawley (1972) examined, respectively, the case of dilute emulsions and dilute slurries. Since the attenuation behavior is strongly dependent upon particle radius, the attenuation versus frequency data for dilute suspensions may be used to determine particle size distributions, as was shown by Duraiswami (1998) for the case of bubbly liquids. The corresponding problem for dilute slurries has been examined in Chapter 5.

In many processes it is desirable to monitor continuous flow of non-dilute suspensions. The particle interactions can have significant effects on the acoustic behavior of non-dilute suspensions, and at the present, rigorous calculations accounting for their effects are lacking. Direct attack on the problem, i.e. solving the linearized

energy, momentum, and continuity equations for multiparticle systems, appears daunting even with the development of efficient computers. Thus, it is necessary to develop a suitable approximate theory and to assess its validity by comparison with the experimental data obtained from different kinds of suspensions.

Two approximate theories commonly used for predicting effective properties of non-dilute suspensions are the cell theory and the effective medium theory. The cell theory models particle interaction effects by assuming that each particle is surrounded by a spherical shell of fluid. This particle-cell assembly is assumed to interact with the rest of the suspension in the least possible manner by requiring, for example, that the tangential stress and the heat flux at the boundary between the cell and the surrounding suspension are zero. The cell theory has been used for predicting the average force on a particle in a fixed bed of particles by Happel and Brenner (1973) and for determining the attenuation of sound waves in slurries by Strout (1991). The main criticism of the cell theory is its *ad-hoc* nature. It is not clear, in general, what conditions must be applied at the cell boundary to ensure the minimal interaction between the cell and the rest of the suspension. Furthermore, it is not even clear that the interaction between the cell and the surrounding suspension must be minimal.

Kuwabara (1959) proposed another model for determining the force on a particle in a fixed bed that assumed that the fluid vorticity, and not the tangential stress, vanishes at the fluid-particle boundary and obtained estimates of the force that are different from those given by Happel and Brenner (1973).

In the effective medium theory the particle-cell assembly is assumed to be immersed in a uniform suspension with properties which are determined by requiring that the governing equations in the particle-cell assembly are consistent with the averaged equations for the suspension. Semi-theoretical reasoning is used to select proper boundary conditions at the interface between the cell and the effective suspension. This selection of boundary conditions renders the effective medium theories somewhat less *ad-hoc* than the cell theory. As a result, the effective medium theory is the approximate theory of choice whenever rigorous calculations involving multiparticle interactions are not feasible or are to time consuming to be practical.

In recent years, the effective medium theory has proven to yield reasonably accurate estimates in a number of cases for which the detailed multiparticle interaction calculations are carried out with the help of high performance computers. This includes the calculations of the force on a particle in fixed beds, effective viscosity and elasticity of random suspensions (Ladd 1990), the Nusselt number for heat transfer from an array of cylinders (Wang and Sangani 1997), and the diffusivity of proteins in bilipid membranes (Dodd *et al.* 1995). The effective medium theory is also applied to the light scattering problem, a problem which is quite similar to the acoustic problem of interest here; and its predictions are shown to compare well with experiments on the light scattered by suspensions (Ma *et al.* (1990)).

In this chapter an effective medium theory is developed to predict the attenuation of sound waves in non-dilute monodispersed suspensions. The accuracy of the theory is

assessed by comparing its predictions against the experimental data available in the literature and with new data obtained in this study.

6.1.1 Linearized Equations:

Consider a small amplitude plane acoustic wave with frequency, ω, propagating through a uniform, monodisperse suspension of solid particles of radius, a. Let us write the density as $\rho_0 + \rho e^{-i\omega t}$, the temperature as $T_0 + Te^{-i\omega t}$, and the velocity as $\mathbf{u}e^{-i\omega t}$. When the amplitudes of ρ, **u**, and T are small, the terms involving the products of these quantities can be neglected from the continuity, momentum, and energy equations to obtain the following linearized equations:

$$-i\omega\rho + \rho_0 \nabla \bullet \mathbf{u} = 0, \tag{6.1}$$

$$-i\omega\rho_0 u_i = \frac{\partial \sigma_{ij}}{\partial x_j}, \tag{6.2}$$

and $$-i\omega\rho_0 C_v T = -\frac{\partial q_j}{\partial x_j} - \rho_0 C_v \beta^{-1}(\gamma - 1)\nabla \bullet \mathbf{u}. \tag{6.3}$$

In writing equation (6.3), we have made use of the linearized equation of state to eliminate the pressure from the usual energy equation. The stress tensor amplitude, σ_{ij},, for a Newtonian fluid is given by

$$\sigma_{ij} = \left[\left\{\frac{c^2\rho_0}{-i\omega\gamma} + \mu_v\right\}\nabla \bullet \mathbf{u} - \left\{\frac{\rho_0(\gamma-1)C_v}{\beta T_0}\right\}T\right]\delta_{ij} + d_{ij}, \tag{6.4}$$

where d_{ij} is the deviatoric component of the rate of strain tensor amplitude

$$d_{ij} = \mu\left[\frac{\partial u_i}{\partial x_j} + \frac{\partial u_j}{\partial x_i} - \frac{2}{3}\delta_{ij}\nabla \bullet \mathbf{u}\right]. \qquad (6.5)$$

In the above equations C_v is the constant volume heat capacity and $\gamma = C_p / C_v$ is the ratio of specific heats, μ and μ_v are the shear and bulk coefficients of viscosity, c is the speed of sound through the fluid, and β is the coefficient of thermal expansion. It should be noted that the first and third terms inside the square brackets on the right-hand side of equation (6.4) are related to the thermodynamic pressure amplitude by

$$p = \left(\frac{\partial p}{\partial \rho}\right)_{T=T_0}\rho + \left(\frac{\partial p}{\partial T}\right)_{\rho=\rho_0}T = \frac{c^2}{\gamma}\rho + \frac{\rho_0(\gamma-1)C_v}{\beta T_0}T. \qquad (6.6)$$

Finally, $q_j = -k\partial T/\partial x_j$ in equation (6.3) is the heat flux, k being the thermal conductivity.

Inside the solid particles equations similar to equations (6.1) through (6.3) apply with the stress tensor, in this case given by Landau and Lifshitz (1986) as

$$\sigma_{ij} = \left[\left\{\frac{\tilde{\lambda} + \frac{2}{3}\tilde{\mu}}{-i\omega}\right\}\nabla \bullet \mathbf{u} - \left\{\frac{\rho_0(\gamma-1)C_v}{\beta T_0}\right\}T\right]\delta_{ij} + \tilde{d}_{ij}; \qquad (6.7)$$

where $\tilde{\lambda}$ and $\tilde{\mu}$ are the Lamé constants for the particles, which are assumed to be perfectly elastic. Note that for solids it is customary to write the stress in terms of displacement and not velocity. For small amplitude oscillatory motions the amplitudes of the two are, of course, related by a factor of $1/(-i\omega)$, and this fact has been used in

writing the first term on the right-hand side of the above equation. Note also that the factor $\tilde{\lambda} + (2/3)\tilde{\mu}$ is the bulk modulus of the solid. Thus, the isotropic part of the stress tensor represented by the terms inside the square brackets in the above equation arises from the density and temperature changes in the solid. The deviatoric stress tensor, $\tilde{d}_{ij}$, is defined in manner similar to equation (6.5), but with the fluid viscosity replaced by $\mu_P = \tilde{\mu}/(-i\omega)$. This term may be thought of as a "particle viscosity". It should be noted that the Lamè constant, $\tilde{\mu}$, is sometimes referred to as the shear modulus.

The above equations must be solved subject to the boundary conditions of continuity of velocity, temperature, heat flux, and traction ($\sigma_{ij} n_j$, n_j being the unit outward normal at the particle surface) at the interface between the particles and the fluid. In concentrated suspensions particle interactions are significant and the rigorous evaluation of sound wave speed and attenuation through the suspension would require a very difficult task of solving the above set of equations in a domain containing many particles. We shall introduce suitable approximations to convert this multiparticle problem to a single particle problem in Section 6.1.4. But first, we shall derive ensemble-averaged equations for the suspension and show how their solutions can be related to the overall speed and attenuation of waves through the suspension.

6.1.2 Ensemble Averaged Linearized Equations for Suspensions:

In this section we ensemble average the equations for the amplitudes of density, velocity, and temperature in the fluid and solid phases, and obtain, thereby, the linearized

continuity, momentum, and energy equations for the suspension. It will be shown that the resulting equations have a form similar to the equations for a single phase, provided that the suspension is assigned suitable properties, which we refer to as the effective properties of the suspension. An important outcome of the averaging process will be that it will yield rigorous expressions for various effective properties of the suspension.

Let $g(\mathbf{x})$ be the particle indicator function defined to be unity when the point, $\mathbf{x}$, is inside any of the particles and zero when $\mathbf{x}$ is in the fluid. The properties of the liquid and particles are denoted by the subscripts, L and P, respectively. The ensemble averaged variables are denoted by angular brackets.

Multiplying the continuity equation for the liquid by the liquid indicator function, (1-g); and that for the solid particle by g; adding the two; and averaging the resulting equation yields the continuity equation for the suspension

$$-i\omega\langle\rho\rangle+\rho_{0L}\langle(1-g)\nabla\bullet\mathbf{u}_L\rangle+\rho_{0P}\langle g\nabla\bullet\mathbf{u}_P\rangle=0. \tag{6.8}$$

The last two terms on the left-hand side of equation (6.8) must now be expressed in terms of the divergence of the average velocity, i.e. $\langle\nabla\bullet\mathbf{u}\rangle$, so that the resulting equation resembles the continuity equation of a single phase medium (cf. equation (6.1)). We begin with the identity

$$\begin{aligned}&\rho_{0L}\langle(1-g)\nabla\bullet\mathbf{u}_L\rangle+\rho_{0P}\langle g\nabla\bullet\mathbf{u}_P\rangle\\&\quad=\rho_{0L}\nabla\bullet\langle\mathbf{u}\rangle+(\rho_{0P}-\rho_{0L})\langle g\nabla\bullet\mathbf{u}_P\rangle+\rho_{0L}\langle(\mathbf{u}_L-\mathbf{u}_P)\bullet\nabla g\rangle\end{aligned}. \tag{6.9}$$

The gradient of the indicator function is zero at all points except at the particle-fluid interface, where it is proportional to the Dirac delta function owing to the step jump in g across the particle-fluid interface.

More specifically, $$\nabla g = -\mathbf{n}\delta(\mathbf{x}-\mathbf{x}_S), \tag{6.10}$$

where $\mathbf{x} = \mathbf{x}_S$ represents the surface of the particles; δ is the Dirac delta function; and $\mathbf{n}$ is the unit normal vector pointing into the liquid, at the particle surface. At the particle-liquid interface it is required that the velocity be continuous. Because the velocity is continuous across the solid-liquid interfaces, the last term in equation (6.9) vanishes. The second term on the right-hand side of equation (6.9) still contains as an unknown the quantity, $\langle g\nabla \bullet \mathbf{u}_P \rangle$. Since the equations of small amplitude acoustics are linear, it is expected that this quantity depends linearly on $\langle \nabla \bullet \mathbf{u} \rangle$. Therefore, one can write this term as

$$\phi\lambda_\rho \nabla \bullet \langle \mathbf{u} \rangle(\mathbf{x}) = \langle g(\mathbf{x})(\nabla \bullet \mathbf{u}_P)(\mathbf{x}) \rangle, \tag{6.11}$$

where ϕ is the volume fraction of the solid particles. Substituting $\langle g\nabla \bullet \mathbf{u}_P \rangle$ from equation (6.11) into equation (6.9) yields the continuity equation for the suspension (equation (6.8)) to be given by

$$-i\omega\langle\rho\rangle + \langle\rho_0\rangle_c \nabla \bullet \langle \mathbf{u} \rangle = 0, \tag{6.12}$$

with the effective equilibrium density of the suspension to be used in the suspension continuity equation, i.e. $\langle\rho_0\rangle_c$ is given by

Physically, λ_v, represents the ratio of the average velocity amplitude inside the particles to that in the suspension. Once again, this coefficient, and such other coefficients to be introduced in this section will, in general, depend on complex multiparticle interactions; and details of its evaluation will be described later.

The right-hand side of equation (6.14) can be simplified by using the identity

$$\frac{\partial\langle\sigma_{ij}\rangle}{\partial x_j} \equiv \frac{\partial}{\partial x_j}\left\langle g\sigma_{ij}^P + (1-g)\sigma_{ij}^L\right\rangle$$
$$= \left\langle g\frac{\partial\sigma_{ij}^P}{\partial x_j}\right\rangle + \left\langle (1-g)\frac{\partial\sigma_{ij}^L}{\partial x_j}\right\rangle + \left\langle \left(\sigma_{ij}^P - \sigma_{ij}^L\right)\frac{\partial g}{\partial x_j}\right\rangle . \qquad (6.17)$$

The last term in the equation (6.17), is related to the jump in traction across the interface and vanishes owing to the boundary condition that $\sigma_{ij}n_j$ be continuous at the particle-fluid interface. Thus, it follows that the right-hand side of equation (6.14) simply equals the divergence of the average stress in the suspension, i.e. the momentum equation for the suspension is given by

$$-i\omega\langle\rho_0\rangle_m\langle u_i\rangle = \frac{\partial\langle\sigma_{ij}\rangle}{\partial x_j}. \qquad (6.18)$$

We must now supplement the above momentum equation with an expression for the average stress. The linearity of the equations implies that the stress amplitude will be linear in the gradient of the average velocity amplitude and $\langle T\rangle$.

Let us first consider the isotropic part of the stress, or equivalently, the stress trace. Multiplying the isotropic part in equation (6.4) by (1-g) and that in equation (6.7) by g and averaging, we obtain

$$\frac{1}{3}\langle\sigma_{kk}\rangle=\left\{\frac{\left(c^2\,\rho_0/\gamma\right)_m}{-i\omega}+\mu_{v,eff}\right\}\nabla\bullet\langle\mathbf{u}\rangle-\left\langle\frac{\rho_0(\gamma-1)C_v}{\beta T_0}\right\rangle_m\langle T\rangle, \qquad (6.19)$$

with

$$\left\langle c^2\rho_0/\gamma\right\rangle_m=c_L^2\rho_{0L}/\gamma_L+\phi\lambda_\rho\left(\left(\tilde{\lambda}+\frac{2}{3}\tilde{\mu}\right)+c_L^2\rho_{0L}/\gamma_L\right), \qquad (6.20)$$

$$\mu_{v,eff}=\mu_v\left(1-\phi\lambda_\rho\right), \qquad (6.21)$$

and

$$\left\langle\frac{\rho_0(\gamma-1)C_v}{\beta T_0}\right\rangle_m=\frac{\rho_{0L}(\gamma_L-1)C_{vL}}{\beta_L T_0}+\phi\lambda_T\left(\frac{\rho_{0P}(\gamma_P-1)C_{vP}}{\beta_P T_0}-\frac{\rho_{0L}(\gamma_L-1)C_{vL}}{\beta_L T_0}\right) \qquad (6.22)$$

The coefficient λ_ρ was defined earlier (cf. equation (6.11)). The parameter, λ_T, , on the other hand, is a new coefficient which is defined as the ratio of the average temperature amplitude inside the particles to that in the mixture, that is

$$\phi\lambda_T\langle T\rangle(\mathbf{x})=\langle g(\mathbf{x})T_P(\mathbf{x})\rangle. \qquad (6.23)$$

Both the effective $c^2\rho_0/\gamma$ and the bulk viscosity of the suspension depend on the coefficient, λ_ρ. This dependence is not surprising since both depend on the average dilatation amplitude inside the particles. The result that the effective bulk viscosity,

$\mu_{v,eff}$, of the suspension depends only on the bulk viscosity of the fluid may seem strange at first sight, but it is really a consequence of the way the isotropic part of the stress is defined for the liquid and solids (cf. equations (6.4) and (6.7)). The stress arising from thermal expansion or, equivalently, temperature fluctuations depends on $\rho_0(\gamma-1)/\beta T_0$ of the two phases and the relative temperature fluctuations in the two phases.

Since the deviatoric stress amplitudes in the individual phases depend only on the velocity gradient amplitude, it is expected that the average deviatoric stress is linear in the gradient of average velocity amplitude. It must also be traceless. If it is assumed that the suspension is macroscopically isotropic, then the average deviatoric stress is characterized by a single effective (shear) viscosity, μ_{eff}. Thus, we may write

$$\langle d_{ij} \rangle = \mu_{eff}\left[\frac{\partial\langle u_i\rangle}{\partial x_j}+\frac{\partial\langle u_j\rangle}{\partial x_i}-\frac{2}{3}\delta_{ij}\nabla\bullet\langle\mathbf{u}\rangle\right]. \qquad (6.24)$$

To obtain the effective (shear) viscosity, μ_{eff}, one must evaluate only one component of the average deviatoric stress. We can take, without loss of generality, the mean velocity amplitude to be given by

$$\langle\mathbf{u}\rangle(\mathbf{x}) = e^{ik_{c,eff}x_1}\mathbf{e}_1, \qquad (6.25)$$

where $\mathbf{e}_1$ is the unit vector along the x_1-axis, taken to be in the direction of propagation of the plane wave, and $k_{c,eff}$ is the effective wave number for the compressional wave through the suspension. The 11-component of the deviatoric stress is given by

$$\langle d_{11}\rangle = 2\left\langle \mu \frac{\partial u_1}{\partial x_1}\right\rangle - \frac{2}{3}\left\langle \mu \frac{\partial u_k}{\partial x_k}\right\rangle. \qquad (6.26)$$

The last term on the right-hand side of equation (6.26), being related to the dilatation amplitudes, can be readily related to the coefficient, λ_ρ, introduced earlier. The first term on the right-hand side can be expressed in terms of a coefficient, λ_d, defined by

$$\phi\lambda_d \frac{\partial\langle u_1\rangle}{\partial x_1} = \left\langle g(\mathbf{x})\frac{\partial u_1^P}{\partial x_1}(\mathbf{x})\right\rangle, \qquad (6.27)$$

With this definition, it is straightforward now to relate $\langle d_{11}\rangle$ to the gradient in the velocity amplitude:

$$\langle d_{11}\rangle = 2\left[\mu_L + \phi\lambda_d(\mu_P - \mu_L)\right]\frac{\partial\langle u_1\rangle}{\partial x_1} - \frac{2}{3}\left[\mu_L + \phi\lambda_\rho(\mu_P - \mu_L)\right]\frac{\partial\langle u_k\rangle}{\partial x_k}, \qquad (6.28)$$

Substituting for $\langle \mathbf{u}\rangle$ from equations (6.25) into (6.28) and also into (6.24) with $i = j = 1$ and comparing the resulting expressions yields the following expressions for the effective viscosity:

$$\mu_{eff} = \mu_L + (1/2)\phi(\mu_P - \mu_L)(3\lambda_d - \lambda_\rho), \qquad (6.29)$$

Finally, the energy equation for the suspension, obtained by averaging (1-g) times the energy equation for the liquid, plus g times the energy equation for the solid to yield

$$-i\omega\langle\rho_0 C_v\rangle_e\langle T\rangle = -\frac{\partial\langle q_j\rangle}{\partial x_j} - \left\langle \rho_0 C_v \beta^{-1}(\gamma - 1)\right\rangle_e \nabla\bullet\langle\mathbf{u}\rangle \qquad (6.30)$$

Here, an argument similar to the one used for equation (6.17) has been used to simplify the energy flux term (thereby using the boundary condition at the particle surface that the heat flux is continuous). It should be noted that in equation (6.30), the effective heat capacity of the suspension is given by

$$\langle \rho_0 C_v \rangle_e = \rho_{0L} C_{vL} + \phi \lambda_T (\rho_{0P} C_{vP} - \rho_{0L} C_{vL}), \qquad (6.31)$$

with λ_T defined by equation (6.23). The effective property, $\left\langle \rho_0 C_v \beta^{-1} (\gamma - 1) \right\rangle_e$, appearing in the last term in the right-hand side of equation (6.30) is related to λ_ρ, and the expression for evaluating it is obtained by replacing λ_T in equation (6.22) by λ_ρ.

The average heat flux is given by

$$\langle q_j \rangle = -\kappa_{eff} \frac{\partial \langle T \rangle}{\partial x_j}, \qquad (6.32)$$

with the effective conductivity given by

$$\kappa_{eff} = \kappa_L + \phi \lambda_\kappa (\kappa_P - \kappa_L), \qquad (6.33)$$

where the coefficient, λ_κ is the ratio of the average temperature gradient amplitude inside the particles to that in the suspension, i.e.,

$$\phi \lambda_\kappa \frac{\partial \langle T \rangle}{\partial x_i} = \left\langle g(\mathbf{x}) \frac{\partial T_P}{\partial x_i}(\mathbf{x}) \right\rangle. \qquad (6.34)$$

In summary, the continuity, momentum, and energy equations for the suspension are given by equations (6.8), (6.18), and (6.30). The averaged stress tensor is given by equations (6.19) and (6.24). The averaged heat flux is given by equation (6.32). These

equations resemble the equations for the single phase given in Section 6.1.1 with suitably defined effective properties of the suspension.

6.1.3 Wave Equations for the Suspension:

In order to find an expression for the attenuation of sound in the suspension, it is necessary to derive wave equations for the suspension, as was done by Epstein and Carhart (1953) for a pure liquid. The derivation of those authors is followed closely. As shown by these investigators the acoustics equations permit three waves: a thermal wave, a shear or rotational wave, and a compressional wave. The last one is the most significant one as far as the attenuation of a planes acoustic wave is concerned. The other waves are important in determining the disturbance produced by a test particle in the suspension as, we shall see in the next section.

We decompose the average velocity amplitude in scalar and vector potentials as given by

$$\langle \mathbf{u} \rangle = -\nabla\Phi + \nabla \times \mathbf{A}. \qquad (6.35)$$

Since the curl of a gradient of any scalar function is zero, $\mathbf{A}$ can be specified to within a gradient of an arbitrary scalar function. To remove this arbitrariness, an additional restriction is imposed that $\mathbf{A}$ be divergence free, i.e., $\nabla \bullet \mathbf{A} = 0$. It may be noted that the vorticity amplitude equals $-\nabla^2 \mathbf{A}$.

Introducing this decomposition in the momentum equation for the suspension (equation (6.18)) and rearranging yields

$$\nabla\left[\omega^2\Phi+\left\{\frac{\left\langle c^2\rho_0/\gamma\right\rangle_m}{\langle\rho_0\rangle_m}-\frac{i\omega}{\langle\rho_0\rangle_m}\left(\mu_{v,eff}+\frac{4}{3}\mu_{eff}\right)\right\}\nabla^2\Phi\right.$$
$$\left.-\frac{i\omega}{\langle\rho_0\rangle_m}\left\langle\frac{\rho_0(\gamma-1)C_v}{\beta T_0}\right\rangle_m\langle T\rangle\right]=\nabla\times\left[\omega^2\mathbf{A}+\frac{i\omega\mu_{eff}}{\langle\rho_0\rangle_m}\nabla\times(\nabla\times\mathbf{A})\right]. \tag{6.36}$$

Here, the vector identity, $\nabla^2\mathbf{a}=\nabla(\nabla\bullet\mathbf{a})-\nabla\times(\nabla\times\mathbf{a})$, is employed. Similarly, the energy equation (equation (6.30)) becomes

$$-i\omega\langle\rho_0C_v\rangle_e\langle T\rangle=\kappa_{eff}\nabla^2\langle T\rangle+\left\langle\rho_0C_v\beta^{-1}(\gamma-1)\right\rangle_e\nabla^2\Phi. \tag{6.37}$$

In equation (6.36) both sides must vanish separately because a rotational vector field cannot balance an irrotational field. Hence, with the right-hand side being zero, using the previously mentioned vector identity and $\nabla\bullet\mathbf{A}=0$ yields

$$\nabla^2\mathbf{A}+k_{sEM}^2\mathbf{A}=0, \tag{6.38}$$

with $k_{sEM}^2\equiv\dfrac{i\omega\langle\rho_0\rangle_m}{\mu_{eff}}$ being the effective wavenumber for shear waves through the suspension. The subscript, *EM*, refers to the effective medium.

The left-hand side of equation (6.36) being zero gives an expression for $\langle T\rangle$ in terms of the velocity potential:

$$\langle T\rangle = \frac{\left[-i\omega\langle\rho_0\rangle_m\Phi - \left\{\frac{i}{\omega}\left\langle c^2\rho_0/\gamma\right\rangle_m + \left(\mu_{v,eff} + \frac{4}{3}\mu_{eff}\right)\right\}\nabla^2\Phi\right]}{\left\langle\frac{\rho_0(\gamma-1)C_v}{\beta T_0}\right\rangle_m},$$

(6.39)

Eliminating $\langle T\rangle$ from the energy equation for the suspension (equation (6.37)) by substituting the above result gives

$$\Phi + (E - F + G)\nabla^2\Phi - EF\nabla^4\Phi = 0, \tag{6.40}$$

with

$$E = \frac{\left\langle c^2\rho_0/\gamma\right\rangle_m}{\langle\rho_0\rangle_m\omega^2} - \frac{i}{\langle\rho_0\rangle_m\omega}\left(\mu_{v,eff} + \frac{4}{3}\mu_{eff}\right) \tag{6.41}$$

$$F = \frac{i\kappa_{eff}}{\omega\langle\rho_0 C_v\rangle_e} \tag{6.42}$$

$$G = \left\langle\rho_0 C_v\beta^{-1}(\gamma-1)\right\rangle_e\left\langle\frac{\rho_0(\gamma-1)C_v}{\beta T_0}\right\rangle_m\Big/\left(\langle\rho_0\rangle_m\omega^2\langle\rho_0 C_v\rangle_e\right). \tag{6.43}$$

Equation (6.40) can be written in the form

$$\left(k_{cEM}^{-2}\nabla^2 + 1\right)\left(k_{tEM}^{-2}\nabla^2 + 1\right)\Phi = 0, \tag{6.44}$$

so that $\Phi = \Phi_c + \Phi_t$ with

$$\left(\nabla^2 + k_{cEM}^2\right)\Phi_c = 0, \tag{6.45}$$

$$\left(\nabla^2 + k_{tEM}^2\right)\Phi_t = 0. \tag{6.46}$$

The effective wavenumbers for the compressional and thermal waves are given by, respectively,

$$k_{cEM}^{-2} = \frac{1}{2}(E - F + G) + \frac{1}{2}\left\{(E - F + G)^2 + 4EF\right\}^{1/2}, \tag{6.47}$$

$$k_{tEM}^{-2} = \frac{1}{2}(E - F + G) - \frac{1}{2}\left\{(E - F + G)^2 + 4EF\right\}^{1/2}. \tag{6.48}$$

As mentioned earlier, the compressional wavenumber is the most important one as far as the propagation of the acoustic plane wave is concerned. The imaginary part of k_{cEM} gives the attenuation while ω divided by the real part of k_{cEM} gives the phase speed.

6.1.4 An Effective-Medium Model:

To determine the attenuation and phase speed, we must now estimate the various effective properties of the suspension. This requires determining the five coefficients: λ_ρ, λ_ν, λ_T, λ_d, and λ_κ. Let us begin with λ_ρ, which represents the ratio of the average dilatation amplitude inside the particles to that in the suspension.

The coefficient, λ_ρ, is defined by equation (6.11), which is equivalent to

$$\phi\lambda_\rho \nabla \bullet \langle \mathbf{u} \rangle (\mathbf{x}) = \int_{|\mathbf{x}-\mathbf{x}_1|\le a} \langle \nabla \bullet \mathbf{u}_P \rangle (\mathbf{x}|\mathbf{x}_1) dV(\mathbf{x}_1). \tag{6.49}$$

Here, we have introduced the conditionally averaged field. Thus $\langle \mathbf{u} \rangle (\mathbf{x}|\mathbf{x}_1)$ the ensemble averaged velocity amplitude at point $\mathbf{x}$, given that in all the ensembles used in the averaging a test particle is centered at $\mathbf{x}_1$. $P(\mathbf{x}_1)$ is the probability density for

finding a particle with its center in the vicinity of $\mathbf{x}_1$. For uniform, monodisperse suspensions $P(\mathbf{x}) = n = 3\phi/\left(4\pi a^3\right)$, n being the number density of the particles and ϕ the particle volume fraction.

We shall use an effective medium approximation for determining the conditionally averaged fields, and, hence, the use of the integrals, such as the one appearing on the right-hand side of equation (6.49). All effective medium approximations must satisfy the criterion that far from the test particle, i.e., for $|\mathbf{x}-\mathbf{x}_1| \to \infty$, the conditionally averaged fields, such as $\langle \mathbf{u} \rangle (\mathbf{x}|\mathbf{x}_1)$ must approach the corresponding unconditionally averaged fields, such as $\langle \mathbf{u} \rangle (\mathbf{x})$. On the other hand, for $|\mathbf{x}-\mathbf{x}_1| \leq a$, i.e., for a point inside the test particle, the conditionally averaged fields must satisfy the equations governing the particle phase. The simplest kind of effective medium approximation, then, assumes that the conditionally averaged equation satisfies the suspending fluid equations for $a \leq r \leq R$ and the unconditionally averaged equations for the suspension for $r \geq R$. Here, $r \equiv |\mathbf{x}-\mathbf{x}_1|$ is the distance from the center of the particle. Different effective medium approximations differ in their choice of R. Some investigators choose $R = a$, which eliminates the fluid region altogether. This makes the subsequent analysis very simple; but, unfortunately, the estimates obtained with $R = a$ are typically inferior, and in some cases unphysical. For example, it may yield negative effective properties at high volume fractions. Other investigators choose $R = a\phi^{1/3}$ with incorrect reasoning that the volumes occupied by

the particle and fluid for $r \le R$ must be proportional to the volume fractions of the two phases. In the present study, we shall choose R to be given by

$$\frac{R}{a} = \left(\frac{1 - S(\mathbf{0})}{\phi} \right)^{1/3} , \tag{6.50}$$

with S(**0**) the zero-wavenumber limit of the suspension structure factor, defined by

$$S(\mathbf{0}) = n \int \left[P(\mathbf{r}|\mathbf{0}) - P(\mathbf{0}) \right] d\mathbf{r} , \tag{6.51}$$

where $P(\mathbf{r}|\mathbf{0})$ is the probability density for finding a particle near **r** given that there is a particle with its center at the origin. (Note that $P(\mathbf{r}|\mathbf{0}) = \delta(\mathbf{r})$ for $r \le a$.) The structure factor of the suspension can be determined experimentally by a light scattering technique; but in the absence of such information, one may choose $S(\mathbf{0})$ to correspond to that of a hard-sphere molecular system for which the well-known Carnahan-Starling approximation yields quite accurate estimates of the structure factor as a function of the volume fraction,

$$S(\mathbf{0}) = \frac{(1-\phi)^4}{1 + 4\phi + 4\phi^2 - 4\phi^3 + \phi^4} . \tag{6.52}$$

The effective medium radius, R, based on $S(\mathbf{0})$ was first introduced by Dodd *et al.* (1995), who compared the results of rigorous multiparticle interactions for determining the short-time self- and gradient diffusivity of proteins in bilipid membranes with those obtained by the effective medium approximation and found very good agreement between the two. In the problems concerned with determining the collective mobility or the sedimentation velocity, where each particle is acted upon with a constant force, it was

shown in Sangani and Mo (1997) that the conditionally averaged velocity has the correct leading order behavior at large r only when R is chosen according to equation (6.50).

For small volume fractions, $S(\mathbf{0})$ given by equation (6.52) behaves as $1 - 8\phi + O\left(\phi^2\right)$ and $R \to 2a$. Thus, in "well-stirred" dilute random suspensions, the effective medium begins at $r = 2a$ according to equation (6.50) and the fluid region $a < r < 2a$ corresponds to the excluded region volume region. Note that the more usual choice of $R = a\phi^{-1/3}$ would, on the other hand, suggest that the effective medium at a very large distance from the test particle in a dilute suspension which is unphysical except for the situations such as dilute periodic or "well-separated" random suspensions defined by Jeffrey ( ) (For such arrays $S(\mathbf{0})$ is small when ϕ is small and equation (6.50) also gives $R/a = O\left(\phi^{-1/3}\right)$.) Thus it is not surprising that R based on equation (6.50) will give better estimates of the effective properties at small to moderate volume fractions compared to those obtained with $R = a\phi^{-1/3}$. Indeed, Sangani and Mo (1997) have shown that the coefficients of $O\left(\phi^2\right)$ corrections to the effective conductivity and elasticity obtained using equation (6.50) are much closer to the rigorous results for these coefficients obtained by detailed pair interaction calculations than those obtained with $R = a\phi^{-1/3}$.

Before closing this brief review of effective medium approximations, we should perhaps note here one more class of effective medium approximations in the literature.

These approximations involve immersing a pair of particles in the effective medium. Examples are the calculations by Kim and Russel (1995) who estimated the permeability of a fixed bed of particles, calculations for the effective viscosity of suspensions with hard-sphere spatial distributions, and Ma *et al.* (1990) for the attenuation due to scattering. These calculations generally require far greater effort, comparable to direct multiparticle calculations, and do not necessarily yield superior estimates compared with the simple approximations based on a single particle. On the other hand, the single particle approximations will be inadequate for the suspension problems in which the changes in microstructure due to imposed flow and their effects, in turn, on the suspension properties must be addressed.

Returning now to the problem of estimating coefficients λ_ρ, etc. using the effective medium model consisting of particle-fluid assembly of radius, R, immersed in a medium with the effective properties of the suspension, we write the velocity inside the test particle in terms of scalar and vector potentials as in the previous section. For the plane wave traveling along the x_1-axis with $\langle \mathbf{u} \rangle(\mathbf{x}) = \exp(i\mathbf{k}_{cEM} \bullet \mathbf{x})\mathbf{e}_1$ we have for $|\mathbf{x}-\mathbf{x}_1| \leq a$,

$$\langle \Phi_{cP} \rangle(\mathbf{x}|\mathbf{x}_1) = \exp(i\mathbf{k}_{cEM} \bullet \mathbf{x}_1) \sum_{n=0}^{\infty} i^n (2n+1) A_{Pn} P_n(\mu) j_n(k_{cP} r), \qquad (6.53)$$

$$\langle \Phi_{tP} \rangle(\mathbf{x}|\mathbf{x}_1) = \exp(i\mathbf{k}_{cEM} \bullet \mathbf{x}_1) \sum_{n=0}^{\infty} i^n (2n+1) B_{Pn} P_n(\mu) j_n(k_{tP} r), \qquad (6.54)$$

$$\langle A_P \rangle(\mathbf{x}|\mathbf{x}_1) = \exp(i\mathbf{k}_{cEM} \bullet \mathbf{x}_1) \sum_{n=0}^{\infty} i^n (2n+1) C_{Pn} P_n^1(\mu) j_n(k_{sP} r), \qquad (6.55)$$

where $r = |\mathbf{x} - \mathbf{x}_1|$, $\mu = \cos\theta$, θ being the angle between $\mathbf{x} - \mathbf{x}_1$ and $\mathbf{k}_{cEM}$, j_n is the spherical Bessel function of the first kind (regular at $r = 0$), and P_n is the Legendre polynomial of degree n ($P^1{}_n$ is associated Legendre polynomial of degree n). AP is the only nonzero (azimuthal) component of **A**.

Similar expressions can be written for $a < r < R$ for which the relevant wavenumbers in the expressions for Φ_{cL}, Φ_{tL}, and A_L are, respectively, k_{cL}, k_{tL}, and k_{sL}. Both the spherical harmonics of the first kind and second kind (corresponding to waves emanating from $r = 0$) must be included in the expression. This leads to a set of six unknowns for each mode n describing the motion in the liquid shell. Finally, for $r > R$, the potentials consist of the plane wave corresponding to the unconditional motion plus the outgoing wave with wavenumbers k_{cEM}, k_{tEM}, and k_{sEM}. Thus a total of 12 unknowns are needed in describing the motion for each mode n. These unknowns are determined from the boundary conditions of continuity of velocity, traction, temperature, and heat flux amplitudes at $r = a$ and $r = R$. Note that the conditional density and temperature amplitudes can be determined from the expressions for Φ_c, Φ_t, and A using the expressions given in the previous section. We keep a total of N modes (typical calculation uses $N = 5$) and solve the resulting $12N$ equations numerically.

We now return to the calculation of λ_p. One must first substitute for

$\nabla \bullet \mathbf{u}_P = -\nabla^2 \Phi_P = k_{cP}^2 \Phi_{cP} + k_{tP}^2 \Phi_{tP}$ in equation (6.49). One may now define the coefficient, η_c, as

$$\phi \eta_c \langle \Phi_c \rangle (\mathbf{x}) \equiv n \int_{|\mathbf{x}-\mathbf{x}_1| \le a} \langle \Phi_{cP} \rangle (\mathbf{x}|\mathbf{x}_1) dV(\mathbf{x}_1), \qquad (6.56)$$

Similarly a coefficient, η_t, is defined with Φ_c replaced by Φ_t. The integration in the above must be carried out over all $\mathbf{x}_1$ such that $|\mathbf{x}-\mathbf{x}_1| \le a$. To convert this to an integration over **r**, we use the identity

$$\begin{aligned} \exp[i\mathbf{k}_{cEM} \bullet \mathbf{x}_1] &= \exp[i\mathbf{k}_{cEM} \bullet \mathbf{x}] \exp[-irk_c \mu] \\ &= \exp[i\mathbf{k}_{cEM} \bullet \mathbf{x}] \sum_{m=0}^{\infty} i^m (-1)^m (2m+1) j_m(k_c r) P_m(\mu) \end{aligned} \qquad (6.57)$$

Now substituting Φ_{cP} form equation (6.53) into (6.56) to give, with $z_{cEM} \equiv k_{cEM} a$,

$$\begin{aligned} \eta_c = \frac{3}{z_{cEM}^2 - z_{cP}^2} \sum_{n=0}^{\infty} (2n+1) A_{Pn} \big[& z_{cP} j_{n-1}(z_{cP}) j_n(z_{cEM}) \\ & - z_{cEM} j_n(z_{cP}) j_{n-1}(z_{cEM}) \big] \end{aligned} \qquad (6.58)$$

In the special case of $n = 0$, $j_{n-1}(z)$ should be replaced by cos(z)/z. Here we have used the solution of equation (6.53); the integral over the radius of the product of two spherical Bessel functions and r^2 is given by Gradshteyn and Ryzhik (1994). Using this result, one can simply write

$$\lambda_\rho = \left(z_{cP}^2 / z_{cEM}^2 \right) \eta_c + \left(z_{tP}^2 / z_{cEM}^2 \right) \eta_t \,. \qquad (6.59)$$

Equation (6.39) shows that the temperature field is linear in Φ_c and Φ_t. Following the notation of Epstein and Carhart (1953) and Allegra and Hawley (1972), where the temperature field is written as $T = b_c\Phi_c + b_t\Phi_t$, one finds that λ_T, as defined by equation (6.23), is given by

$$\lambda_T = \left(b_{cP}/b_{cEM}\right)\eta_c + \left(b_{tP}/b_{tEM}\right)\eta_t . \qquad (6.60)$$

Note that the unconditionally averaged $\langle T\rangle = b_{cEM}\langle\Phi_c\rangle$ because the unconditionally averaged $\langle\Phi_t\rangle = 0$.

The other λ's are evaluated in a similar manner and are inter-connected. The definition of λ_v is first written as an integral similar to that in equation (6.49) for the component of the velocity inside the particle in the direction of the wave. The velocity inside the particles can now be split up into three parts (two velocity potentials and a rotational contribution), so that one can write

$$\lambda_v = \lambda_v^{\Phi_c} + \lambda_v^{\Phi_t} + \lambda_v^{\mathbf{A}}, \qquad (6.61)$$

where λ_v^{Φ} and $\lambda_v^{\mathbf{A}}$ are the irrotational and rotational field contributions, respectively. The irrotational contributions to λ_v are

$$\lambda_v^{\Phi_c} = \eta_c + \frac{3}{z_{cEM}}\sum_{n=0}^{\infty} A_{Pn} j_n\left[n j_{n-1}\left(z_{cEM}\right) - \left(n+1\right) j_{n+1}\left(z_{cP}\right)\right]; \qquad (6.62)$$

and a similar expression for $\lambda_v^{\Phi_t}$ (just replace z_{cP} by z_{tP} and A_{Pn} by B_{Pn}), where terms that give a spherical Bessel function of negative order are omitted. In deriving equation (6.62) use has been made of equation (6.57) and

$$\exp[-i\mathbf{k}_{cEM}\bullet\mathbf{s}]\nabla_{\mathbf{s}}\Phi(\mathbf{s})=\nabla_{\mathbf{s}}\{[-i\mathbf{k}_{cEM}\bullet\mathbf{s}]\Phi(\mathbf{s})\}+i\mathbf{k}_{cEM}\exp[-i\mathbf{k}_{cEM}\bullet\mathbf{s}]\Phi(\mathbf{s}),\tag{6.63}$$

with $\mathbf{s} = \mathbf{x} - \mathbf{x}_1$. The divergence theorem is used to evaluate the integral of the first term on the right-hand side of equation (6.63); the second term is seen to simply lead to η_c in equation (6.62). The rotational contribution to λ_v is

$$\lambda_v^{\mathbf{A}}=\frac{3}{z_{cEM}}\sum_{n=0}^{\infty}n(n+1)C_{Pn}j_n(z_{sP})\left(j_{n+1}(z_{cEM})+j_{n-1}(z_{cEM})\right).\tag{6.64}$$

Here, a similar relation to equation (6.63) is used

$$\exp[-i\mathbf{k}_{cEM}\bullet\mathbf{s}]\nabla_{\mathbf{s}}\times\mathbf{A}(\mathbf{s})=\nabla_{\mathbf{s}}\times\{[-i\mathbf{k}_{cEM}\bullet\mathbf{s}]\mathbf{A}(\mathbf{s})\}+\exp[-i\mathbf{k}_{cEM}\bullet\mathbf{s}]i\mathbf{k}_{cEM}\times\mathbf{A}(\mathbf{s}).\tag{6.65}$$

Recognizing that the second term on the right-hand side does not contribute to the component in the wave direction of the velocity inside the particle, this term is left out in the evaluation of $\lambda_v^{\mathbf{A}}$.

The result for λ_v can be used to determine other λ's as well. We notice that

$$\lambda_k=(b_{cP}/b_{cEM})\lambda_v^{\Phi c}+(b_{tP}/b_{cEM})\lambda_v^{\Phi t}.\tag{6.66}$$

Finally, λ_d, defined by equation (6.27), equals

$$\lambda_d=\lambda_d+\lambda_d^{\Phi c}+\lambda_d^{\Phi t}+\lambda_d^{\mathbf{A}},\tag{6.67}$$

where we have, again, made use of equation (6.63), with Φ replaced by $\mathbf{u}$. The result for $\lambda_d^{\Phi c}$ is

$$\lambda_d^{\Phi c} = \frac{3}{z_{cEM}^2}\sum_{n=0}^{\infty} A_{Pn}\left[\left\{z_{cP}j_n'(z_{cP})+(n+1)j_n(z_{cP})\right\}\left\{\left(\frac{(n+1)^2}{2n+3}+\frac{n^2}{2n-1}\right)\right.\right.$$
$$\times j_n(z_{cEM}) - \frac{(n+1)(n+2)}{2n+3}j_{n+2}(z_{cEM}) - \frac{n(n-1)}{2n-1}j_{n-2}(z_{cEM})\Big\}$$
$$\left. + \frac{(n+1)(2n+1)}{2n+3}j_n(z_{cP})\left\{(n+2)j_{n+2}(z_{cEM})-(n+1)j_n(z_{cEM})\right\}\right]. \tag{6.68}$$

Again, $\lambda_d^{\Phi t}$ is obtained from $\lambda_v^{\Phi c}$ by replacing A_{Pn} by B_{Pn}, and z_{cP} by z_{tP}. Those terms which would give a spherical Bessel function of negative order at $n \le 1$ are omitted from this formula. The evaluation of λ_d is complete with

$$\lambda_d^{\mathbf{A}} = \frac{3}{z_{cEM}^2}\sum_{n=1}^{\infty}(n+1)C_{Pn}\left[-\frac{n(n+2)}{2n+3}X_{n,n+2}\right.$$
$$\left. - \frac{n(2n+1)}{(2n+3)(2n-1)}X_{n,n} + \frac{n(n-1)}{2n-1}X_{n,n-2}\right], \tag{6.69}$$

with the short hand notation

$$X_{n,m} \equiv -\frac{3}{2}j_n(z_{sP})j_m(z_{cEM}) - \frac{1}{2}\left(z_{sP}j_n'(z_{sP})j_m(z_{cEM})\right.$$
$$\left. + z_{cEM}j_n(z_{sP})j_m'(z_{cEM})\right). \tag{6.70}$$

Again, the terms which give a spherical Bessel function of negative order at $n = 1$ are to be omitted.

This completes the calculation of the attenuation. The attenuation is the real part of k_{cEM}, given by equation (6.47), the right-hand side of which contains the effective

medium properties that have been expressed in the unknown parameters, λ_ρ, etc. These parameters are calculated from the above expressions by solving first, at each n, for the coefficients, A_{Pn}, etc., from the boundary conditions at the particle and shell interfaces. In the boundary conditions the effective medium properties show up as well (e.g., the effective viscosity and conductivity), so that this procedure is repeated until the λ's have converged.

6.2 Attenuation Measurements in Concentrated Solid-Liquid Systems:

In order to test the effective medium theory for concentrated slurries (solids volume fractions greater than about 10% by volume), attenuation measurements are performed in slurries of Potter's beads in mixtures of glycerin in distilled water.

The first set of measurements is actually performed on a dilute (5 % by volume) slurry over the entire experimental frequency range. Although this is not a concentrated slurry, these data are necessary in order to test the theoretical effective medium calculations. Any effective medium approach to the forward problem theory should reduce to the theory of Allegra and Hawley (1972) for small solids volume fraction. Having data at lower volume fractions, such as 5 %, allows for "tuning" the effective medium approach by providing a basis for comparison between the results of the Allegra and Hawley (1972) theory, the effective medium approach, and experimental data. If the effective medium approach is correctly formulated, the attenuation spectra generated in all three cases should be essentially the same. Data are collected using both the

Toneburst and Pulse/FFT techniques. The experimentally obtained attenuation spectrum is shown, together with results predicted by the theory, in Figure 6.1.

Attenuation measurements are then made in slurries of 10 %, 15 %, 20 %, 30 %, 40 %, 45 %, and 50 % solids by volume. Figures 6.2 & 6.3 show attenuation as a function of solids volume fraction in the Potter's Beads slurries for several different frequencies. In this figure, the experimental data (markers) are also compared with results of theoretical calculations (solid curves) employing the effective medium approach using a mean particle diameter of 130 μm with standard deviation of 22 μm. The results for lower frequencies (1.5, 1.75, 2.0, 2.25, and 2.75 MHz) are shown in Figure 6.2, and the agreement between theory and experiment is rather good up to a solids volume fraction of approximately 0.30. Agreement is better at frequencies above 2 MHz than for those below. The experimental data at all frequencies appear to go through a maximum at solids volume fraction of approximately 0.30. It should be noted that similar behavior was seen by Atkinson (1991), who also observed a maximum at a solids volume fraction of approximately 0.30, in the attenuation versus concentration curves he obtained for 1.0 mm diameter glass beads in a fluidized bed. The attenuation data from this study then go through a minimum at a volume fraction of approximately 0.4 or 0.5, and then the attenuation begins to increase again. This behavior is interesting in that the attenuation curves predicted by the effective medium theory show monotonically increasing behavior. There is definitely a change in the apparent slope of the theoretical curves, but there are no local maxima or minima. Nevertheless, it can be said that there is fairly good agreement between the effective medium theory and

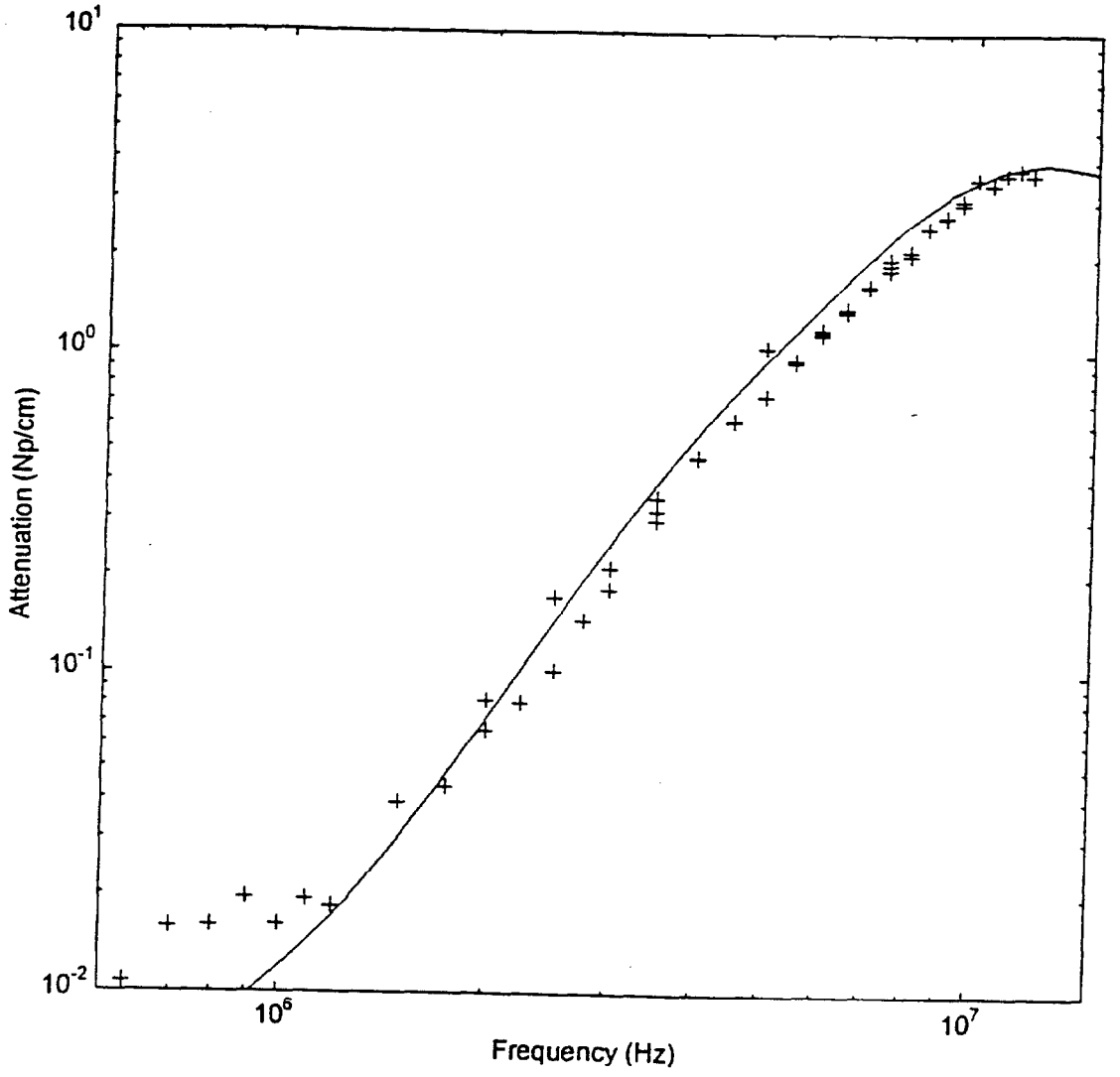

Figure 6.1: Attenuation versus frequency behavior for a slurry of Potter's beads in a mixture of glycerin/water at 5 % by volume—forward theory and experimental data. - E2162.

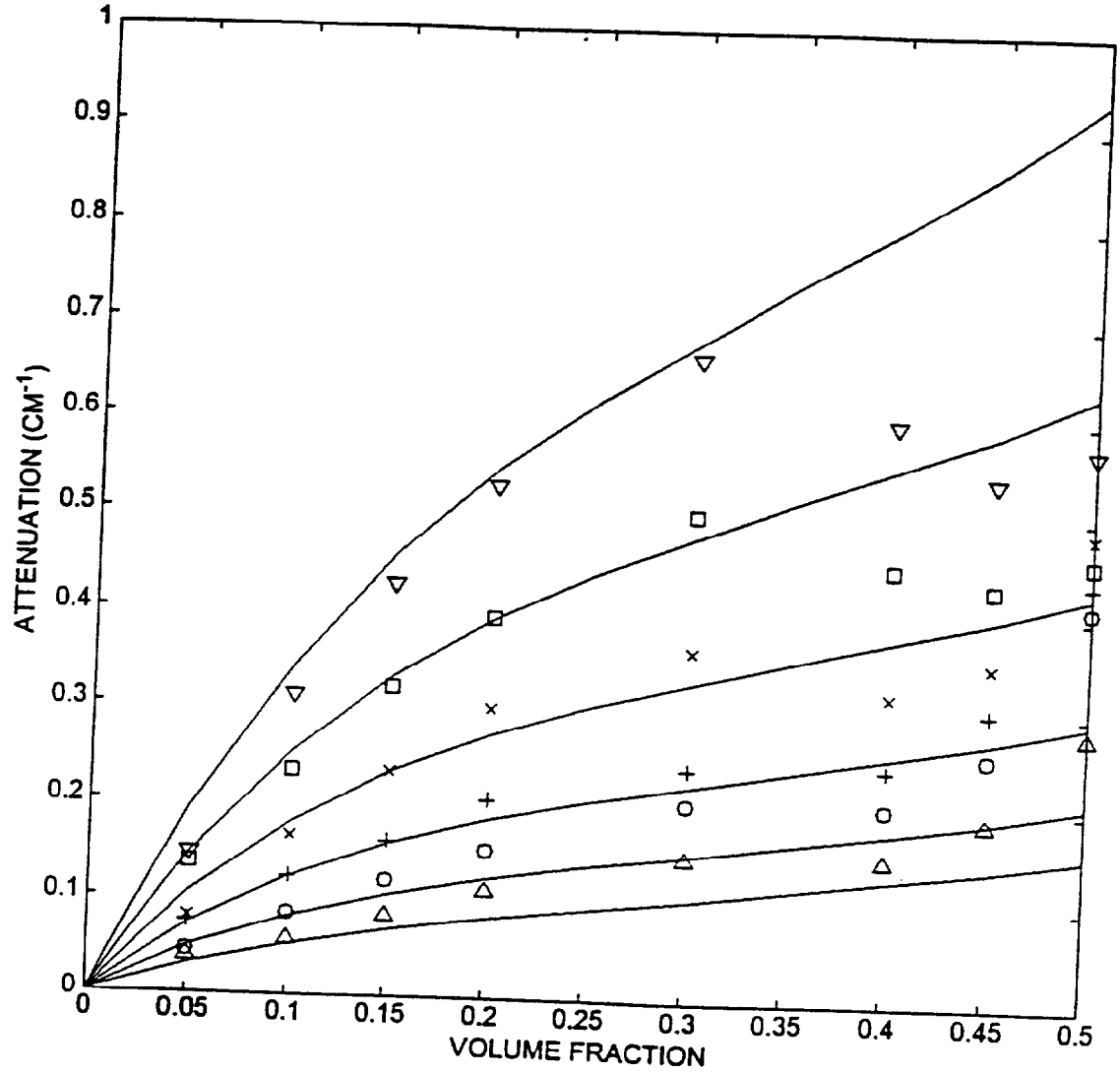

Figure 6.2: Attenuation as a function of solids volume fraction at various frequencies in slurries of Potter's beads in glycerin/water. Data are shown for 1.5 MHz (Δ); 1.75 MHz (O); 2.0 MHz (+); 2.25 MHz (×); 2.5 MHz (□); and 2.75 MHz (∇). The solid curves represent the results of the effective medium calculations using a particle size distribution with 65 μm mean radius and standard deviation of 11 μm. - E4172.